

NON-PRECIOUS METAL CATALYSTS PREPARED BY  
CHEMICAL FUNCTIONALIZATION OF CARBON SURFACES

by

STEPHANIE MAVILLA

B.Sc. University of Ontario Institute of Technology

B.Ed. University of Ontario Institute of Technology

A THESIS SUBMITTED IN PARTIAL FULFILLMENT OF  
THE REQUIREMENTS FOR THE DEGREE OF  
MASTER OF SCIENCE

in

THE FACULTY OF SCIENCE

MATERIALS SCIENCE

UNIVERSITY OF ONTARIO INSTITUTE OF TECHNOLOGY

August 2014

© Stephanie Mavilla, 2014

## Abstract

New sources of power are of great interest as attempts to make smaller, more convenient and environmentally friendly sources are being investigated. Hydrogen fuel cells are a way to combine both an effective method of power supply, converting chemical energy into electrical energy directly, and a way to employ clean energy. Fuel cells involve the use of platinum (Pt) as a catalyst, for both the oxygen reduction and hydrogen oxidation reactions, which is both rare and expensive. As such, there is significant ongoing research towards the discovery of non-precious metal catalysts (NPMC) with activity comparable to that of Pt.

The Fe-N/C catalyst system is a promising alternative, though the exact structure of the active catalytic site is still debated. Active catalysts are typically formed by high temperature (600 – 1000°C) pyrolysis in an ammonia atmosphere of a carbon with adsorbed iron on the surface. Our approach to these catalysts employs surface chemical methods to more systematically synthesize the active site in order to better relate structure and activity. The current nitrogen compound of interest is 5,6-diamino-1,10-phenanthroline (aphen) which was attached to a carbon support (Black Pearls 2000 or Ketjen Black EC600JD) using a diazonium coupling reaction. This a chemisorption process, as opposed to physisorption one, that allows for a clearer model of attachment of the aphen molecule.

In order to understand the effects of the precursor and the metal on active site density and activity many synthetic parameters were varied and measurements were taken at each step of the process. Aphen loading was investigated by preparing a series of samples with increasing ratios of aphen to Black Pearls 2000 and Ketjen Black EC600JD. Iron uptake was also explored by using two different iron salts; iron(III) chloride and iron(II) acetate. An alternate carbon support and synthetic route was also explored using graphene oxide in a glycerol reflux to mimic reactions commonly used to make organometallic compounds.

Overall it was found that the Black Pearls 2000 outperformed the Ketjen Black EC600JD samples at all ratios. An optimal heat treatment, ink loading and ratio of aphen to carbon black pearls was determined for these catalyst materials. It was also observed that using iron(III) chloride for the iron uptake step produced the most active catalyst. Electrochemical and structural measurements indicate that the success of the diazonium coupling reaction and graphitization during heat treatment are essential to the synthesis of active materials.

## Acknowledgments

I would like to first thank Dr. Brad Easton for the opportunity to work in his lab (despite my lack of ability to convert units in undergrad) and all the guidance over the course of this project. It is thanks to him that I now have a better understanding and appreciation for electrochemistry and materials science. I would also like to extend my thanks to my co-supervisor Dr. B.J. MacLean for his help and guidance (those organic molecules can be tricky) and to the other members of my committee. I am also grateful to the members of the Easton lab (past and present) for their help and patience as I worked through my project. Special thanks to Mohammad for answering my persistent questions and to Ranga for assistance with SEM and Raman measurements.

I also owe gratitude to Richard, Mike, and Clayton for all the chats where I was able to share ideas, get feedback or just learn some new things. It was always great to have a couple offices to pop into when I needed a short break or a new set of ears. The faculty and staff at UOIT are a great support system and I am thankful that I am able to receive my Master's Degree from UOIT.

During the course of this degree I faced many personal trials in addition to the academic challenges and the support of all those around me has helped (and continues to help) me through it. My dad, Christina (and boys), Anthony and Jonathan have been so strong and I want to thank them for everything they have done for me. A very heartfelt thank you goes out to Jennie Eastcott for always being there to talk to when I needed it and offering unconditional support. I am grateful for all the understanding and supportive people I have been surrounded by; this project and thesis would not be completed if it wasn't for all of them.

Last, but most definitely not least, I want to thank my fiancé, Patrick Edge. He has grounded me over the last few years and I do not know what I would have done without him. He has supported me both academically and personally and I do not have enough words to convey my gratitude. Not only have I received his comfort and guidance, but I have also felt love and support from his family; Debra, Martin and Tori have contributed a large amount to my success.

Everything that I have done and the person that I am today is in a large part due to one person; my mom. She supported and encouraged me when I started this project and I know that she would be proud to see it complete. I would like to dedicate this work in loving memory of my mom, Sue Yuen Mavilla.

# Table of Contents

Abstract.....	i
Acknowledgments.....	ii
Table of Contents.....	iii
Table of Figures.....	vi
Table of Tables .....	x
List of Equations.....	xi
Common Abbreviations .....	xii
Chapter 1 Introduction .....	1
1.1 General Background.....	2
1.2 Proton Exchange Membrane Fuel Cells .....	2
1.3 Oxygen Reduction Reaction.....	3
1.4 Traditional Catalysts.....	6
1.5 Non Precious Metal Catalysts .....	7
1.5.1 The M-N/C Active Site.....	7
1.5.2 Early Materials .....	8
1.5.3 Metal Precursors and Ligands.....	9
1.5.4 Metal Loading .....	11
1.5.5 Carbon Support.....	12
1.5.6 Chemical Modification .....	13
1.5.7 Heat Treatment Conditions .....	16
1.6 Thesis Objective .....	17
Chapter 2 Experimental .....	19
2.1 Catalyst Synthesis .....	20
2.1.1 Precursor Materials.....	20
2.1.1.3 Carbon Supports .....	20
2.1.2 Diazonium Coupling of Aphen to Carbon .....	20
2.1.3 Iron Coordination.....	21
2.1.4 Heat Treatment.....	22
2.1.5 Glycerol Reflux Treatment .....	22
2.2 Characterization.....	23

2.2.1 Electrochemical Measurements .....	23
2.2.2 Thermogravimetric Analysis (TGA) .....	24
2.2.3 Raman Spectroscopy.....	25
2.2.4 X-Ray Photoelectron Spectroscopy (XPS) .....	25
2.2.5 Scanning Electron Microscopy (SEM) and Transmission Electron Microscopy (TEM)..	25
2.2.6 Brunauer-Emmett-Teller Analysis (BET) .....	25
Chapter 3 Detailed Study of Fe-N/C Catalysts Prepared by the Diazonium Coupling Reaction ....	26
3.1 Method Validation .....	27
3.2 Non-Precious Metal Catalyst Studies.....	29
3.2.2 Impact of Catalyst Ink Concentrations.....	32
3.3 Results & Discussion: Black Pearls Series Catalysts .....	33
3.3.1 Impact of Aphen Loading .....	33
3.3.2 Effects of Modification on Black Pearls Structure .....	43
3.4 Results & Discussion: Ketjen Black Series Catalysts.....	53
3.4.1 Impact of Aphen Loading .....	53
3.4.2 Effects of Modification on KB Structure .....	62
3.4 Comparison of Base Carbon.....	68
Chapter 4 Modifications to NPMC Synthesis.....	79
4.1 Changing the Iron Salt.....	80
4.1.1 Varying Concentrations.....	86
4.1.2 Acid Leached .....	88
4.2 Graphene Oxide and the Glycerol Reflux.....	90
4.2.1 Graphene Oxide Synthesis .....	91
4.2.2 Conventional Catalyst Synthesis using GO precursor .....	93
4.2.3 Glycerol Reflux .....	96
Chapter 5 Conclusions and Future Directions .....	99
5.1 Optimal Conditions for the Synthesis of NPMCs .....	100
5.1.1 Aphen Ratio.....	100
5.1.2 Carbon Support.....	100
5.1.3 Iron Salt .....	101
5.1.4 Additional Modifications to procedure.....	101
5.1.5 Optimal Conditions .....	102

5.2 Future Directions .....	102
5.2.1 Verify the Diazonium Coupling Reaction .....	102
5.2.2 Iron Salt .....	103
5.2.3 Ammonia Heat Treatment .....	103
5.2.4 Glycerol Reflux .....	104
5.2.5 Alternate Nitrogen Precursor .....	104
5.2.6 Durability and Full Cell Tests .....	105
References .....	106
Appendices.....	112

## Table of Figures

Figure 1.1. Schematic Diagram of a Proton Exchange Membrane Fuel Cell.....	3
Figure 1.2. Ideal versus actual performance of a fuel cell. ....	4
Figure 1.3. Potential pathways of the two and four electron oxygen reduction reaction. ....	6
Figure 1.4. Structure of the active site as proposed by Dodelet. <sup>31</sup> .....	8
Figure 1.5. Structure of heme B, a component of a protein in the blood that transports oxygen..	9
Figure 1.6. Examples of structures used for early NPMCs; (A) Phthalocyanine and (B) Porphine.	10
Figure 1.7. Representation of the different types of nitrogen linkages on a carbon support.....	10
Figure 1.8. Structure of the nitrogen containing precursors (A) 1,10-phenanthroline and (B) 5,6-diamino-1,10-.....	14
Figure 1.9. Schematic for the (A) diazonium coupling reaction and (B) benzimidazole coupling reaction. ....	14
Figure 1.10. Partial diazotization of aphen to the diazonium ion for the diazonium coupling reaction, further.....	15
Figure 1.11. Partial dediazonation reaction of the diazonium ion to generate a radical which will reaction with the.....	15
Figure 1.12. Proposed active site modelled after the slit pore method proposed by Dodelet. <sup>31</sup>	17
Figure 3.1. CV results for Johnson Matthey 20% Pt on carbon black. Measurements were obtained at 10 mv/s in an .....	27
Figure 3.2. Rotating disk measurements for JM20%Pt at various rotation rates in an O <sub>2</sub> saturated 0.5M sulphuric .....	28
Figure 3.3. Koutecky-Levich analysis for JM20%Pt compared to the theoretical 2 and 4 electron oxygen reduction .....	29
Figure 3.4. ORR activity for (A) BPS4Fe and (B) KBS3Fe treated at four different temperatures to determine optimal .....	31
Figure 3.5. Hydrogen peroxide production of (A) BPS4Fe and (B) KBS3Fe treated at four different temperatures to .....	31
Figure 3.6. Comparison of performance of BPS4Fe700 at different catalyst loadings as seen by the (A) ORR activity.....	33
Figure 3.7. Proposed redox activity of the aphen groups on the carbon surface resulting in the peak seen at 0.65 V.....	34
Figure 3.8. Cyclic voltammograms for each prepared ratio of BP and Aphen. Measurements are .....	34
Figure 3.9. Relationship between charge transferred and ratio for BPS1-BPS5.....	35
Figure 3.10. Proposed mechanism of the multilayer formation from the diazonium coupling reaction.....	36
Figure 3.11. Cyclic voltammograms for each prepared ratio of BP with Aphen and iron following heat .....	36
Figure 3.12. Change in ORR activity before (A) and after (B) treatment. Measurements were performed at 900 RPM in an O <sub>2</sub> saturated 0.5 M sulphuric acid solution.....	37
Figure 3.13. Relationship between onset potential and ratio for BPS1Fe700 to BPS5Fe700. ....	39

Figure 3.14. Comparison of the limiting current and onset potential for BPS1Fe700 to BPS5Fe700. ....	39
Figure 3.15. Comparison of hydrogen peroxide production for BPS1 - BPS5 (A) to BPS1Fe700 – BPS5Fe700 (B).....	40
Figure 3.16. Comparison of the hydrogen peroxide production and ratio for BPS1Fe700 to BPS5Fe700. ....	41
Figure 3.17. Koutecky-Levich analysis for the BP series compared to the theoretical two and four electron .....	42
Figure 3.18. Comparison of the activity of BPS4Fe700 to a platinum standard. Measurements were obtained in an .....	43
Figure 3.19. Analysis of pore size distribution for the final catalyst of the BP series.....	45
Figure 3.20. Raman data for all catalyst materials from the BP series compared to unmodified BP .....	46
Figure 3.21. Sample of deconvolution fit for the Raman spectra of BPS4Fe700. All spectra were fitted with four.....	47
Figure 3.22. Comparison of the IG/ID ratio for each sample in the BP series. ....	48
Figure 3.23. N-1s Narrow scan XPS data for final catalysts materials of the BP- series. ....	50
Figure 3.24. Possible nitrogen functionalities present in the catalyst materials; (A) pyridinium, (B) pyridone, and (C) .....	51
Figure 3.25. TEM images of BPS4Fe700 at 142000X, 250000X, 31500X, 50000X, 80000X, and 400000X magnification .....	53
Figure 3.26. Cyclic voltammograms for each prepared ratio of KB and Aphen. Measurements are .....	54
Figure 3.27. Relationship between charge transferred and ratio for KBS1-KBS5.....	55
Figure 3.28. Cyclic voltammograms for each prepared ratio of KB with aphen and iron following heat .....	56
Figure 3.29. Change in ORR activity (A) with aphen alone and (B) with aphen, iron, and post heat treatment.....	56
Figure 3.30. Relationship between onset potential and ratio for completed KB series.....	57
Figure 3.31. Comparison of the limiting current and onset potential for the full BP series.....	58
Figure 3.32. Change in hydrogen peroxide production before (A) and after (B) treatment. Measurements were.....	59
Figure 3.33. Comparison of the hydrogen peroxide production and ratio for KBS1Fe700 to KBS5Fe700 .....	60
Figure 3.34. Koutecky-Levich analysis for the KB series compared to the two and four electron processes. ....	60
Figure 3.35. Comparison of the activity of KBS3Fe700 and KBS5Fe700 to a platinum standard. Measurements were.....	62
Figure 3.36. Histogram comparing the pore size of the samples prepared with KB after heat treatment and.....	63
Figure 3.37. Raman data for catalyst materials from the KB series (A) with aphen alone and (B) with .....	64

Figure 3.38. Comparison of the $I_G/I_D$ ratio for each sample in the KB series compared to the unmodified support. ....	65
Figure 3.39. N-1s Narrow scan XPS data for final catalysts materials of the KB series. ....	66
Figure 3.40. TEM images of KBS4Fe700 at 142000X, 200000X, 31500X, 63000X, 160000X, and 400000X magnification .....	68
Figure 3.41. Comparison of the oxidative peak for the aphen redox couple for the best catalysts of the BP and KB .....	69
Figure 3.42. Comparison of the amount of active aphen present in BPS1-5 and KBS1-5. ....	70
Figure 3.43. Comparison of the activity for the best samples of each series. Measurements were obtained at a .....	71
Figure 3.44. Histogram comparing the pore size of the (A) best samples of the BP and KB series and (B) the bare .....	73
Figure 3.45. Comparison of the N-1s Narrow scan XPS spectra for BPS4Fe700 and KBS4Fe700. .	75
Figure 3.46. Koutecky-Levich analysis for the best samples of the BP and KB series compared to .....	77
Figure 3.47. Comparison of the number of electrons transferred for the BP and KB series as calculated from the.....	77
Figure 4.1. Comparison of the activity of the BP series prepared with iron(II) acetate in (A) a 50:50 mixture.....	81
Figure 4.2. Comparison of the hydrogen peroxide production of the BP series prepared with iron(II) .....	81
Figure 4.3. Comparison of the trend in onset potential of the BP series prepared with iron(II) acetate in .....	82
Figure 4.4. Comparison of the number of electrons transferred for the BP series prepared with iron(II) .....	83
Figure 4.5. Koutecky-Levich analysis for the sample treated in ammonia compared to the theoretical 2 and 4 .....	83
Figure 4.6. Comparison of the activity of the best sample of the BP series prepared with iron(II) acetate in .....	84
Figure 4.7. Determination of the iron content for select samples of the iron(II) acetate series. Measurements were.....	85
Figure 4.8. Initial CV scan for BPS4FeA700 obtained in an $N_2$ saturated 0.5 M solution of sulphuric acid. ....	86
Figure 4.9. Comparison of the sample prepared with a lower concentration of iron(II) acetate to the best sample of .....	87
Figure 4.10. Koutecky-Levich analysis for the sample prepared with a lower concentration if iron(II) acetate .....	88
Figure 4.11. Comparison of the ORR activity for the sample leached in an acid solution to both BPS4FeLow700 and.....	89
Figure 4.12. Koutecky-Levich analysis for the acid leached sample compared to the theoretical 2 and 4 .....	90

Figure 4.13. Proposed active site formation on graphene oxide. It is expected that aphen will functionalize the GO .....	91
Figure 4.14. Comparison of Raman spectra for (A) graphite flakes <sup>75</sup> and (B) synthesized graphene oxide.....	92
Figure 4.15. TEM image of the graphene oxide at 180000X magnification. ....	92
Figure 4.16. Comparison of the CV for graphene oxide reacted with aphen and the unmodified GO. Measurements.....	93
Figure 4.17. Comparison of the ORR activity of the graphene oxide sample compared to the best BP .....	94
Figure 4.18. TEM images of samples prepared with graphene oxide at (A) 80000X magnification and (B) 400000X.....	95
Figure 4.19. Comparison of the ORR activity of the graphene oxide sample prepared with a glycerol reflux .....	96
Figure 4.20. TEM images of samples prepared with graphene oxide and a glycerol reflux at (A) 100000X magnification and (B) 400000X magnification.....	97
Figure 5.1. Potential nitrogen precursors for synthesis of NPMCs; (A) amine and (B) tetra-amino pthalocyanine <sup>76</sup> .....	105

## Table of Tables

Table 1.1. Comparison of surface area for select carbon black materials.....	12
Table 2.1. Black Pearls 2000 series ratios for samples 1 through 5.....	21
Table 2.2. Ketjen Black EC600JC series ratios for samples 1 through 5.....	21
Table 2.3. Conditions for cyclic voltammetry measurements .....	24
Table 3.1. Summary of information regarding the activity for the final catalysts in the BP series. .....	42
Table 3.2. Summarized BET data for the BP series with aphen, iron, and after heat treatment. .	44
Table 3.3. Comparison of the amount of nitrogen added to black pearls via diazonium coupling of aphen to the .....	52
Table 3.4. Summary of information regarding the activity for the final catalysts in the KB series. .....	61
Table 3.5. Summarized BET data for the final catalysts of the KB series.....	62
Table 3.6. Summary of XPS data for each final catalyst in the ketjen black series.....	67
Table 3.7. Summary of structural information for the best catalysts of each series.....	72
Table 3.8. Summary of key features for the best catalysts of each series. ....	76
Table 4.1. Comparison of key parameters for the sample prepared with a lower concentration of iron(II) acetate to .....	87
Table 4.2. Comparison of key parameters for the acid leached sample to the best catalyst treated with iron(II) .....	89
Table 4.3. Comparison of key parameters for the sample prepared with the GO support to the best catalyst of the.....	94
Table 4.4. Comparison of key parameters for the sample prepared from graphene oxide and glycerol reflux to .....	96

## List of Equations

Equation 1-1. Four electron reduction of oxygen to water .....	5
Equation 1-2. Two electron reduction of oxygen to hydrogen peroxide .....	5
Equation 1-3. Two electron reduction of hydrogen peroxide to water.....	5
Equation 2-1. Calculation for the percentage of hydrogen peroxide produced .....	24
Equation 2-2. Calculation for te number of electrons tranferred .....	24
Equation 3-1. Levich Equation .....	28

## Common Abbreviations

PEMFC	Proton exchange membrane fuel cell
HOR	Hydrogen oxidation reaction
ORR	Oxygen reduction reaction
SHE	Standard hydrogen electrode
Ea	Activation energy
NPMC	Non precious metal catalyst
CoPC	Cobalt Phthalocyanine
Aphen	5,6-diamino-1,10-phenanthroline
GO	Graphene oxide
BP	Black pearls 2000
KB	Ketjen back EC600JD
RHE	Reversible hydrogen electrode
DI	Deionized water
RRDE	Rotating ring disk electrode
CV	Cyclic voltammograms
LSV	Linear sweep voltammetry
TGA	Thermogravimetric analysis
XPS	X-ray photoelectron spectroscopy
SEM	Scanning electron microscopy
TEM	Tunneling electron microscopy
BET	Brunauer-Teller analysis
RPM	Rotations per minute
ECSA	Electrochemical surface area
I <sub>G</sub>	Intensity of graphitic peak
I <sub>D</sub>	Intensity of disordered peak

# **Chapter 1**

## **Introduction**

## 1.1 General Background

The search for an alternate energy source that is green, readily available and inexpensive is a large area of focus in the scientific community. Currently the use of fossil fuels far exceeds any other energy source; 80.6% worldwide<sup>1</sup> and 62% in Canada<sup>2</sup> in 2010. This dependence on fossil fuels is not a feasible long term option due to both the environmental impact and availability of these sources. As a result of contaminants in fossil fuels by products such as  $\text{NO}_x$ ,  $\text{SO}_x$ , and other species are formed. Once free in the atmosphere, catastrophic consequences such as smog, acid rain, ozone depletion and global warming result.<sup>3</sup> In addition to this, it is predicted that the current supplies of fossil fuels will run out by 2112<sup>4</sup> stressing the need to quickly find cost effective and efficient ways to replace these sources.

Finding ways to harness clean energy sources and make smaller and more convenient devices are aspects that many research groups and companies strive towards.<sup>5</sup> One of the advantages to fossil fuels is the ease of distribution; it can be easily supplied to different areas and is used in many applications. Current technologies need to maintain this ease of distribution to create a viable option for future power generation on large scale. Fuel cells and batteries are both methods that allow for the conversion of chemical energy to electrical energy with both presenting their own set of problems. Batteries are a closed system with a limited supply of electricity which is dictated by the amount of chemicals it can store and how they can move within the unit.<sup>6</sup> Fuel cells on the other hand operate as an open system – as long as fuel is being fed into the system, electricity can be produced. Although there are a variety of systems being researched and employed that allow for most of these conditions to be met, hydrogen fuel cells have become popular due to their simple design and basic chemical requirements.<sup>7</sup>

## 1.2 Proton Exchange Membrane Fuel Cells

Proton exchange membrane fuel cells (PEMFCs) work to produce energy in the form of electrons using hydrogen as an energy source and converting chemical energy to electrical energy directly. PEMFCs are composed of three main parts; the anode, the cathode and the proton exchange membrane.<sup>8</sup> Figure 1.1 illustrates the basic setup of a PEMFC indicating the processes that occur at each component. Hydrogen is introduced to the anode which catalyzes the hydrogen oxidation reaction (HOR) to produce protons and electrons. The electrons travel through an external circuit to power a device while the protons travel through the exchange membrane.

Oxygen is fed into the cathode side where the oxygen, electrons and protons combine at another catalyst site for the oxygen reduction reaction (ORR) to form water.

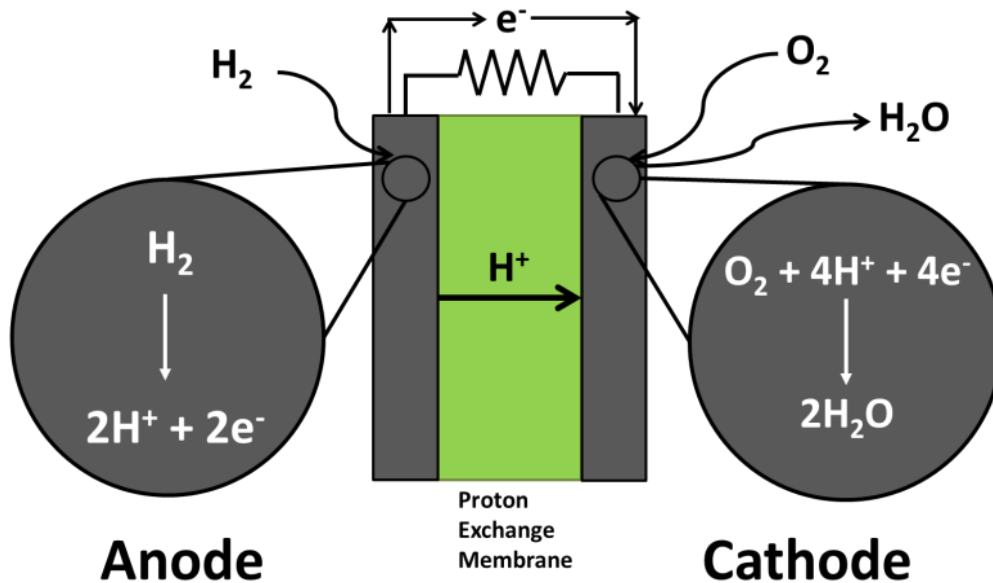


Figure 1.1. Schematic Diagram of a Proton Exchange Membrane Fuel Cell

The anode and cathode are generally composed of a high surface area carbon with embedded metal catalyst particles, typically platinum (Pt). The membrane between the anode and cathode is generally a polymer electrolyte permeable to protons but not electrons or the gasses that are introduced to each side of the fuel cell.<sup>9</sup> This directs the electrons to an external circuit and prevents gasses from mixing together and reacting in a way that inhibits the use of the produced electrons. Although fuel cells are a promising area of research, there are still many challenges associated with the efficiency and effectiveness of these devices. Problems with the permeability of the membrane may arise and although the HOR is easily accomplished using a platinum catalyst, the rate of the ORR is slow even with a platinum catalyst, which limits the efficiency of the fuel cell.<sup>9</sup>

### 1.3 Oxygen Reduction Reaction

The ideal operating cell voltage is based on the thermodynamic potentials of the ORR (1.229 V vs. standard hydrogen electrode (SHE)) and HOR (0 V vs. SHE) is 1.229 V. These are the theoretical maximums that this system can achieve. However, this potential is difficult to achieve due to a variety of effects which can be seen in Figure 1.2. There are three main sources

of this deviation from the ideal case; activation, ohmic and concentration polarization (or over-potential)<sup>10</sup> which will impact the rate of electron transfer.

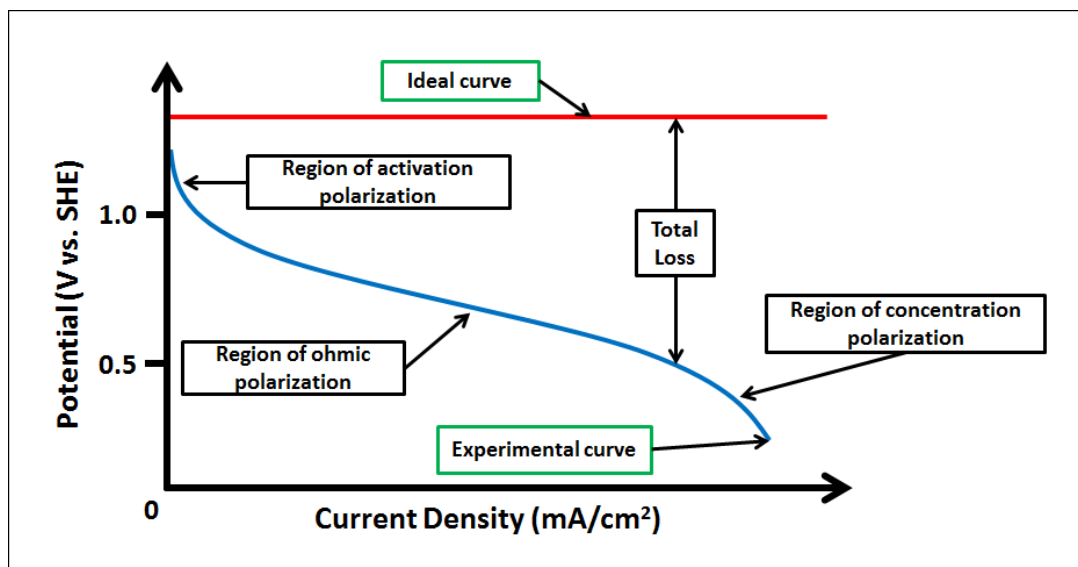


Figure 1.2. Ideal versus actual performance of a fuel cell.

The Activation over-potential is dependent on the activation energy ( $E_a$ ) of the charge transfer reaction<sup>11</sup>; if there is a high  $E_a$  then an over-potential is required to move the reaction forward. Therefore the observed potential will differ from the thermodynamic potential of the reaction. This effect is seen at low current densities where other effects such as ohmic and concentration over-potentials are not yet significant. At high current densities the effects of the concentration polarization begin to impact current produced. The concentration over-potential is the difference between measurements made with the same reference at the electrode and those made in the bulk solution.<sup>11</sup> This effect arises from mass transport problems that occur as the concentration of the analyte is depleted and the diffusion layer expands. Ohmic over-potential (linear region) is the largest and most sustained loss that contributes to the operation of a fuel cell. This arises from resistance in electrolyte, electrode materials and wires that make up the cell and results in a drop in voltage.<sup>11</sup> While activation and concentration over-potentials can be mitigated, ohmic polarization is more difficult to limit as it is inherent to the transport of protons. In a fuel cell the ohmic polarization can be reduced with a good membrane, however over potentials in the ORR will still remain fairly large.

One of the main complications of the ORR is the different pathways that the reaction can proceed by. Equation 1.1 illustrates the four electron process in which the oxygen is directly

reduced to water. Equation 1.2 shows the two electron reduction of the oxygen to hydrogen peroxide ( $\text{H}_2\text{O}_2$ ) followed by the two electron reduction of  $\text{H}_2\text{O}_2$  to water seen in Equation 1.3 . The four electron pathway is preferred for two main reasons; the higher reduction potential and the inert product. The higher reduction potential the more readily a reaction will occur. This also indicates an ability to harness more energy from the redox process. In theory, the four electron process is thermodynamically favoured for the reasons stated above; however differences in catalyst material, operating conditions, and environmental conditions will impact whether or not this will also be kinetically favoured. Figure 1.3 illustrates the competition between the different pathways that the ORR can proceed by and their associated rates ( $k_1$ ,  $k_2$ , etc.). Variations in these rates and the factors that affect them, will dictate which pathway the reaction will proceed by.

Another key aspect seen in Equation 1.3 is the very high reduction potential of  $\text{H}_2\text{O}_2$  to water, resulting in a very readily reduced species. This high potential allows the  $\text{H}_2\text{O}_2$  to be a very strong oxidizing agent which aids in its ability to degrade the catalyst and electrode materials.<sup>12</sup>



Or



It is known that the  $\text{H}_2\text{O}_2$  is detrimental to the function of the fuel cell due to it being a strong oxidizer, and it is possible that the species is able to move freely in the catalyst layer or remain in the active site.

Figure 1.3 illustrates the potential pathways for the four and two electron ORR and their respective rates ( $k$  values).<sup>13</sup> The oxygen is first adsorbed onto a catalyst site where it can be reduced to hydrogen peroxide ( $k_2$ ) or water ( $k_1$ ). If hydrogen peroxide is formed, it can either be reduced further to water ( $k_3$ ) at the same active site or be desorbed ( $k_6$ ). Once desorbed, it is free to chemically react with other species and potentially degrade electrode materials. However, it could also re-adsorb onto another catalyst site ( $k_6'$ ) and be electrochemically reduced to water.

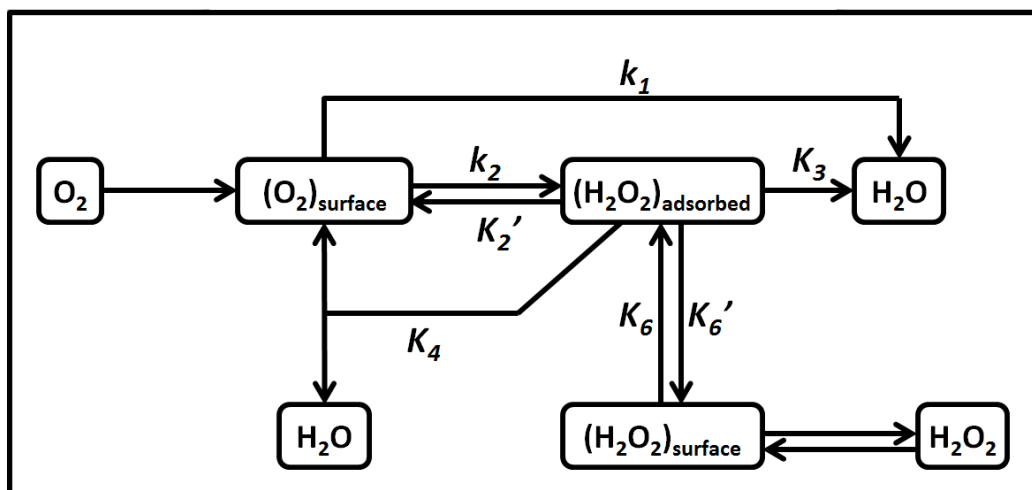


Figure 1.3. Potential pathways of the two and four electron oxygen reduction reaction.

## 1.4 Traditional Catalysts

The overall operating potential of the fuel cell will depend on the reactions occurring at both the anode (HOR) and the cathode (ORR). The predominant catalyst used for both these reactions is platinum which is extremely effective at the anode with an activation over-potential around 50 mV compared to  $\sim 200$  mV at the cathode.<sup>14</sup> As seen in Equations 1.1 to 1.3, the ORR can occur through different mechanisms which may involve the production of hydrogen peroxide. Two such proposed mechanisms are the dissociative and associative processes.<sup>15</sup> In the dissociative mechanism  $O_2$  is adsorbed onto Pt resulting in the immediate breakage of the O-O bond. The adsorbed O then forms water by gaining two  $H^+$  and two electrons. An alternate mechanism is the associative process in which  $O_2$  maintains its bond when adsorbed onto the Pt surface resulting in the potential to form  $H_2O_2$  as an intermediate to the water.

Although Pt is commonly used as a catalyst for the ORR, it is rare and expensive. Currently the cost of Pt is just over \$1400 per ounce of precious metal.<sup>16</sup> Even if cost was not an issue, the world's supply of Pt would not be sufficient to even replace the current number of vehicles, let alone accommodate a growing demand<sup>4</sup>. In addition to this, the cathode is still lagging behind the anode with respect to performance indicating that Pt may not be the ideal catalyst material for the ORR.

One method that is currently being employed to reduce the usage of Pt and enhance the ORR activity revolves around the use of Pt alloys. Various metals, such as other precious metals<sup>17</sup> or non-precious transition metals,<sup>18,19</sup> can be alloyed with platinum to synthesize these

types of catalyst. In some cases multiple metals can be used to create ternary or quaternary alloys.<sup>20</sup> Although these materials have been successful, they still utilize Pt which is not ideal. Efforts to remove the precious Pt metal have been investigated in the form of non-precious metal catalyst (NPMCs).

## 1.5 Non Precious Metal Catalysts

There is a large amount of work being done to reduce and maximize the use of Pt in current fuel cell catalysts which has proven to be successful. However, even a small amount of platinum will impact our worldwide supply and still be fairly expensive. Ideally Pt would be removed from the catalyst altogether, but a metal is still required for the synthesis of active catalyst materials. In order to reduce cost and increase availability, research is ongoing in finding ways to employ non precious metals for the ORR catalysts.

### 1.5.1 The M-N/C Active Site

Much work has been done to synthesize non-precious metal catalysts using metals such as Cobalt (Co) and Iron (Fe).<sup>21-24</sup> There is ongoing debate surrounding the structure of the active site for NPMCs; there has not been nor is there currently a method to determine with certainty what the structure of the most active catalyst is.<sup>25,26</sup> Despite the uncertainty regarding the exact structure, there is general agreement surround the components that make up the active site. The most active catalysts have been found to coordinate transition metals with nitrogen functionalities on a carbon support.<sup>27,28</sup> The role of metal in the active site is also debated and it is thought by some that the nitrogens themselves are solely responsible for the improved activity towards the ORR.<sup>29</sup> However, in the case of iron, due to the low amount of metal necessary to observe an increase in activity (as low as 0.16%)<sup>30</sup>, it is unlikely that these materials are truly metal free. Iron impurities in the carbon materials needed to synthesize these catalysts would be sufficient to improve the activity.

Overall there are many factors that may impact the activity of the catalyst material which include the type of nitrogen, metal precursor and loading, carbon support, method of attachment, and heat treatment conditions.<sup>27,28</sup> Better definition of the active site is necessary to truly determine how each factor impacts the overall catalyst material. One model of the active site, proposed by Dodelet,<sup>31</sup> is the slit pore structure seen in Figure 1.4. The mechanism for the synthesis of this structure is discussed further in a later section. This M-N<sub>4</sub>/C form relates

back to original NPMCs<sup>32</sup> that were first shown to have activity towards the ORR and is the structure that the active sites of this work are predicted to take.

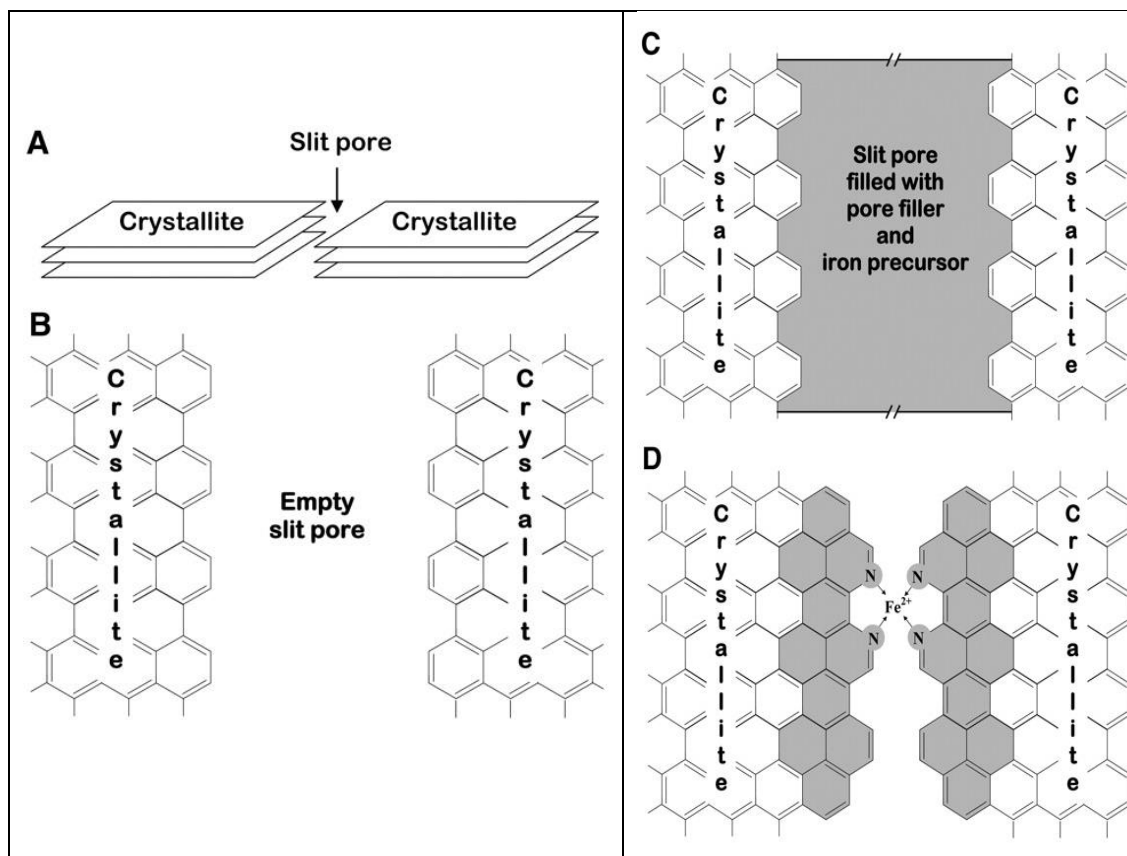


Figure 1.4. Structure of the active site as proposed by Dodelet.<sup>31</sup> From [Lefevre, M.; Proietti, E.; Jaouen, F.; Dodelet, J. Iron-Based Catalysts with Improved Oxygen Reduction Activity in Polymer Electrolyte Fuel Cells. *Science* 2009, 324, 71-74]. Reprinted with permissions from AAAS.

### 1.5.2 Early Materials

These types of materials were first investigated in alkaline environments in 1964 using metal porphyrin structures.<sup>32</sup> These structures had previously demonstrated activity in redox processes of organic molecules<sup>32</sup> and show similarity to the oxygen carrying heme groups (Figure 1.5) present in the human body. It was later demonstrated that  $N_4$  metal complexes were active in an acidic media as well.<sup>33</sup>

The M- $N_x$ /C catalysts were generally synthesized with a high surface area carbon support with their catalytic abilities being impacted by both the selected ligand and metal.<sup>27</sup> In terms of the metal centre, it was seen that Co demonstrated a preference for the two electron process, producing a hydrogen peroxide intermediate, while Fe materials were active towards the four

electron process to directly produce water.<sup>27</sup> Although these catalyst materials were active towards the ORR, their stability rendered them impractical for fuel cell applications.<sup>33</sup> However, information surrounding the active site and impacts of the metals and ligands can be determined from studying these non pyrolyzed materials.

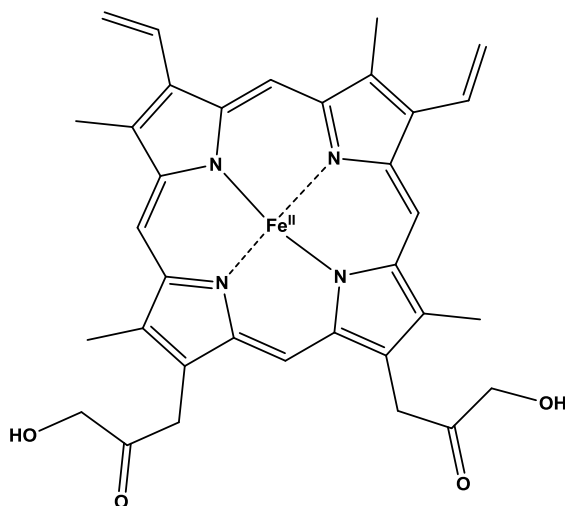


Figure 1.5. Structure of heme B, a component of a protein in the blood that transports oxygen.

Early M-N<sub>x</sub>/C materials demonstrated some activity towards the ORR however stability became a problem especially in acidic environments.<sup>33</sup> In order to address this issue, higher temperature heat treatments (400 – 1000°C) were utilized in the synthesis of these materials.<sup>27</sup> Overall, pyrolysis has a positive impact on the performance of the catalysts; however, due to the high temperatures and metal content the structure of the active sites may be altered. This makes it difficult to determine what the active site looks like and how this relates to the activity of the catalyst.

### 1.5.3 Metal Precursors and Ligands

Initial materials used bulky metal porphyrin structures to integrate metals into the catalyst. Figure 1.6 illustrates two examples of these bulky C/N structures. In 1964, Jasinski expanded on the applications of metal phthalocyanine catalysts that were being used for various purposes such as the catalytic degradation of hydrogen peroxide and oxidation of a variety of organic compounds.<sup>32</sup> Jasinski tested Co, Ni, Pt, and Copper (Cu) and determined that the cobalt phthalocyanine (CoPc) was the most active. Since then it has also been determined that Fe based catalysts present comparable activity to that of Co.<sup>23</sup> Due to the lower cost<sup>34</sup>, abundance, and preferential ORR reduction pathway<sup>27</sup>, Fe is a commonly used transition metal for these

materials. More current materials use a variety of ligands and precursors including organic molecules, organic polymers, inorganic salts or gasses.<sup>27,28,35</sup>

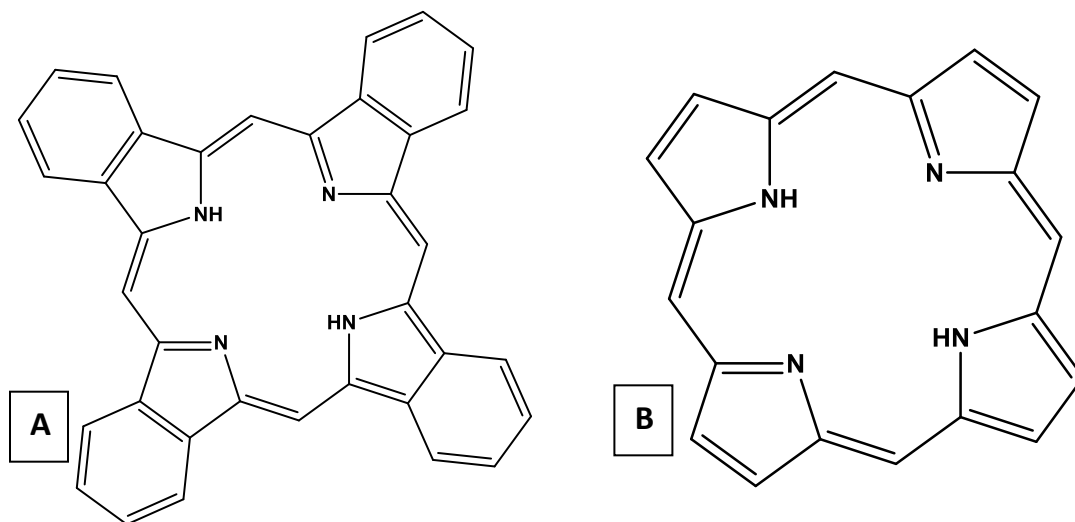


Figure 1.6. Examples of structures used for early NPMCs; (A) Phthalocyanine and (B) Porphine.

Active Fe-N/C catalysts are generally prepared by integrating nitrogen into a carbon backbone coupled with coordination to iron. Typically this involves physisorption of both the nitrogen and iron followed by a high temperature (600 – 1000°C) pyrolysis, which is sometimes performed in the presence of ammonia (NH<sub>3</sub>).<sup>31</sup> As this process involves physisorption of the nitrogen, a variety of linkages can form leading to uncertainty regarding the structure of the active site. Figure 1.7 illustrates the possible nitrogen linkages that may form when carbon supports are exposed to a nitrogen source.

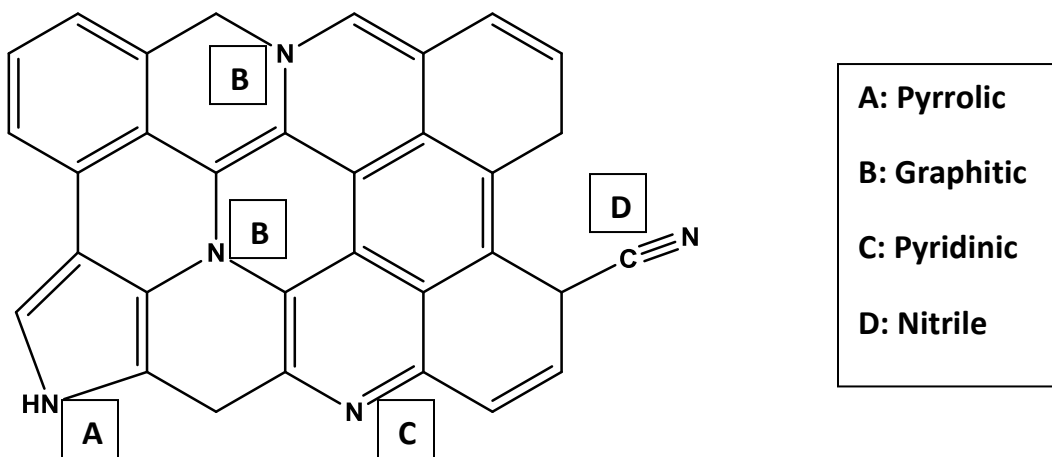


Figure 1.7. Representation of the different types of nitrogen linkages on a carbon support.

The variety of methods used to introduce N into the carbon backbone allows for a wide variety of catalyst materials and active sites. There are various sources of Fe that can be used which increases the variability with the ORR catalysts. More commonly, inexpensive Fe salts such as iron(II) acetate or iron(III) chloride are used in place of larger cyclic structures such as those utilized in early materials. This generally leads to a wide variety of catalytically active sites with different types of N-species that may or may not be coordinated to Fe. This can therefore make it difficult to relate ORR activity to any one specific active site structure making optimization more difficult and variable.

#### 1.5.4 Metal Loading

The metal type and method to introduce it into the carbon material is a key factor in synthesizing an active catalyst. In addition to this the amount of the metal and, likely linked to that, the number of active sites will also impact the overall activity. Since a variety of carbon supports are utilized in literature and each procedure varies, it is difficult to determine the ideal amount of metal. It has been determined within studies that there is an ideal ratio and going above or below this percentage will negatively impact the activity of the material.<sup>36,37</sup>

Depending on the method used, it may be difficult to keep the amount of metal within the ideal range. It has been shown that loadings of Fe at 0.16 wt% are sufficient to yield materials with high activity and a plateau is seen in materials with a weight percent above 0.5.<sup>30</sup> The low amount of required iron also makes it difficult to prepare catalyst materials that are metal free and are said to work via the catalytic ability of nitrogen alone. Trace amounts of iron in carbon supports may integrate into the active site during the synthesis process. Although complete removal of trace iron is difficult, removal of excess iron is achievable if the iron uptake step introduces too much of the metal.

In 2008, Dodelet reported using an acid leaching technique<sup>38</sup> in order to remove any excess iron that may have been impeding the activity of the catalyst. Initial materials were prepared with an iron loading of 10% which was reduced to 6.2% following treatment in acid. Samples were treated at room temperature in a solution of sulphuric acid at a pH of 0.5 for 12 hours, after which they were filtered and dried in an oven overnight. Dodelet determined that the removal of this excess iron did improve the overall activity of the material indicating that dissolution of iron not bound to an active site negatively affects performance. Further adding to the uncertainty of the role of Fe in the active site, catalyst materials were also prepared by

treatment with Cl<sub>2</sub> to further reduce the amount of iron to 3.3%. Despite the very low content, the materials treated with Cl<sub>2</sub> were shown to be more active than those that were treated in acid alone. This indicated that either there was Fe coordinated in the active sites which made it unable to be transported out with the Cl<sub>2</sub> treatment or Fe is not in the active sites at all. Studies have been done that propose Fe (or other non-precious metals) are not part of the active site but only work towards creating an active N based catalytic centre.<sup>39,40</sup>

### 1.5.5 Carbon Support

High surface area, disordered carbon materials generally provide the best support for these catalysts.<sup>27,35</sup> These materials will offer a large number of potential catalytic sites as well as undergo sufficient rearrangements during heat treatment to improve activity. Over the years a variety of supports have been utilized with the three more common carbon blacks<sup>41</sup> listed in Table 1.1 with their corresponding surface areas. It is well known that nitrogen plays a key role in the activity of these materials; therefore the ability of the carbon to successfully integrate nitrogen groups is a factor in selecting the backbone. In addition to the impacts from the surface area, it has been shown that the porosity of the carbon support will impact the success of the catalyst material with investigations into the impact of mesopores<sup>42</sup> and micropores.<sup>43</sup>

**Table 1.1. Comparison of surface area for select carbon black materials.**

<b>Carbon Support</b>	<b>Surface Area (m<sup>2</sup>/g)</b>
Black Pearls 2000	1755
Ketjen Black EC600JD	1492
Vulcan XC-72R	234

The method of introducing nitrogen will impact the factors that need to be considered regarding the carbon support. One of the more common methods of nitrogen impregnation is through the use of high temperature pyrolysis under ammonia (NH<sub>3</sub>).<sup>27,35,44</sup> The treatment of carbon materials with NH<sub>3</sub> also causes etching via gasification which creates micropore structures that helps improve the catalytic activity with a mass loss of 30 – 50% creating the most active materials.<sup>45</sup> The more disordered the carbon material, the more effective this NH<sub>3</sub> treatment is.<sup>27</sup> Methods to increase the disorder of carbon materials, such as ball milling, have been employed to improve activity.<sup>28</sup> Ball milling allows for the materials to be crushed and ground into a fine powder which impacts the structure of the starting carbon materials.

An alternative method involves the use of microporous materials as the main support rather than creating the micropores via the  $\text{NH}_3$  heat treatment.<sup>46</sup> In this study, Lefèvre et al used microporous Black Pearls 2000 carbon black (micropore area of  $934 \text{ m}^2/\text{g}$ ) with iron(II) acetate. It was determined that there was not a high enough N content with the base carbon to successfully create active sites. In order to introduce N without the  $\text{NH}_3$  heat treatment, Lefèvre et al used 1,10 – phenanthroline (Figure 1.8). The carbon support, nitrogen containing compound, and iron precursor were ball milled in order to fill the micropores without impacting the microstructure of the carbon. Following the pore filling step, the materials were heat treated at  $1050^\circ\text{C}$  under argon and then  $950^\circ\text{C}$  under  $\text{NH}_3$ . It was found that the  $\text{NH}_3$  step continued to improve the catalyst activity despite starting with a highly microporous material and high nitrogen content. Figure 1.4 illustrates the proposed structure of the active site as it is subjected to each stage of the synthesis.<sup>46</sup> Although these materials provided good activity towards the ORR, their stability was not ideal and this aspect needs to be further optimized.

The heat treatment step is an important aspect of the NPMC synthesis as it provides a method of altering the carbon support. The transformations of the carbon and changes in its structure have been studied.<sup>47</sup> Easton et al. annealed amorphous films made of carbon, nitrogen and a transition metal, prepared via sputtering, at various temperatures to study changes in the composition and carbon structure. It was determined that as the temperature increased, the samples transformed to a mixture of amorphous and graphitized carbon. This transformation was catalyzed by the added metal. As higher levels of graphitization occurred, more nitrogen was lost from the sample and eventually the loss was so great the activity began to decline. This indicates that the level of graphitization in both the initial and final material is important; with the heat treatment relating these two aspects to each other.

### 1.5.6 Chemical Modification

The use of 1,10 – phenanthroline by Lefèvre et al provided a middle ground between bulky porphyrin compounds and adsorbed surface nitrogen. These materials yielded acceptable activity towards the ORR, however the active site still remains undefined. It is possible to create a more defined active site by using a chemisorption method to covalently attach a molecule in place of physisorption.<sup>48</sup> Pauric et al used two chemical reactions to couple 5,6-diamino-1,10-phenanthroline (aphen, Figure 1.8B) to Black Pearls 2000; a benzimidazole coupling<sup>49</sup> (Figure 1.9B) and a diazonium coupling<sup>50</sup> (Figure 1.9A). Both these reactions provide a clear method of

attachment which allows for a more accurate prediction of the active site. In addition to synthesizing active catalyst materials, it has also been confirmed that the type of nitrogen plays an important role in the overall activity.<sup>48</sup> The most active catalyst materials appear to be formed when pyridinic type nitrogens are involved,<sup>51</sup> making aphen an ideal precursor.

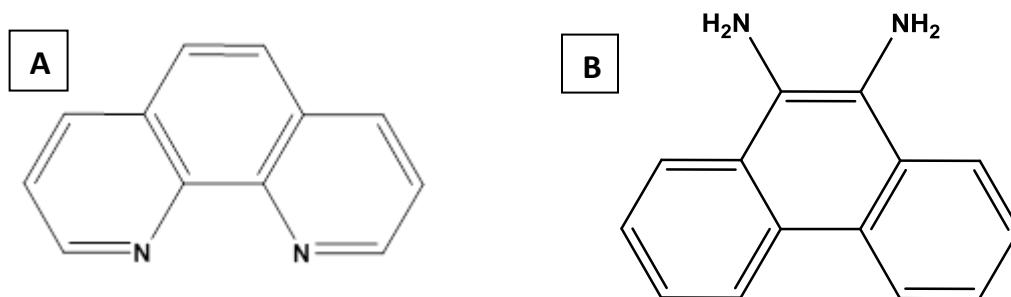


Figure 1.8. Structure of the nitrogen containing precursors (A) 1,10-phenanthroline and (B) 5,6-diamino-1,10-phenanthroline used to synthesize some NPMCs.

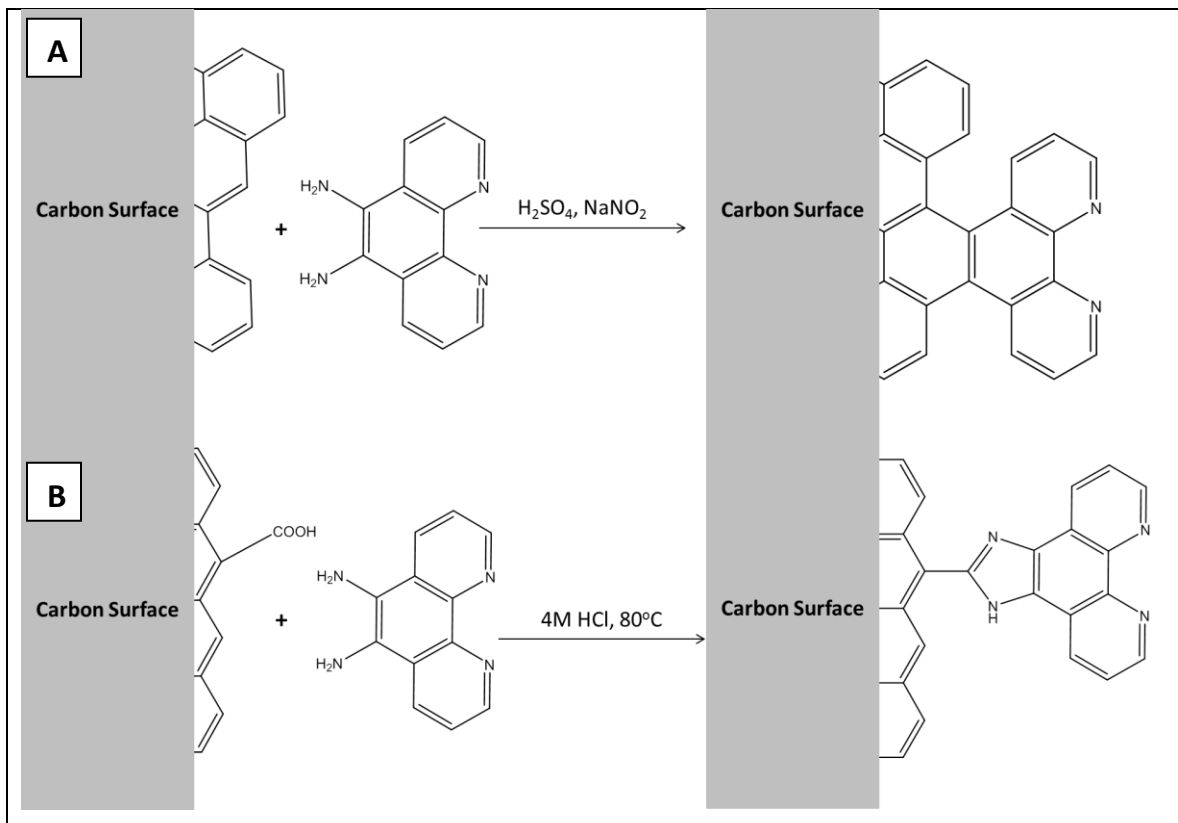
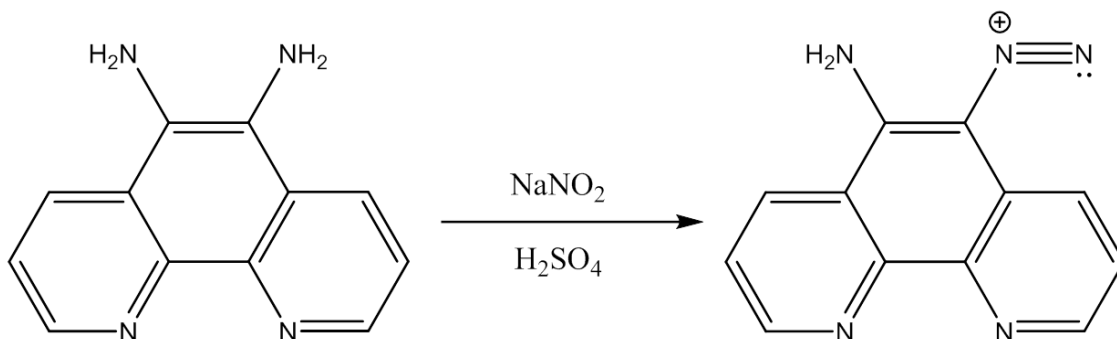


Figure 1.9. Schematic for the (A) diazonium coupling reaction and (B) benzimidazole coupling reaction.

The focus of this work is the diazonium coupling which requires the conversion of the aphen to a diazonium salt before further reaction with the carbon support (Figure 1.10). This is

accomplished by reaction with sodium nitrite and sulphuric acid, though any strong acid will facilitate the reaction<sup>52</sup>.



**Figure 1.10. Partial diazotization of apheh to the diazonium ion for the diazonium coupling reaction, further reaction converts the second amine to a diazonium functionality.**

Following the diazotization of apheh, it will undergo dediazonation generating a radical (Figure 1.11). The formation of the radical is dependent on the acceptance of an electron, which can be obtained a variety of ways<sup>53</sup>. For use as a catalyst precursor, this reaction typically takes place in an electrochemical cell in which the electron is supplied by a reduction at the electrode surface<sup>54,55</sup>. Without the aid of an electrode, this reduction can be photoinduced, occur radiolytically, or be aided by a metal ion<sup>53</sup>. In the case of the reaction with a carbon black system a spontaneous radical reactions will occur<sup>77</sup> and facilitate the completion of the reaction with the generation of nitrogen gas as a strong driving force.

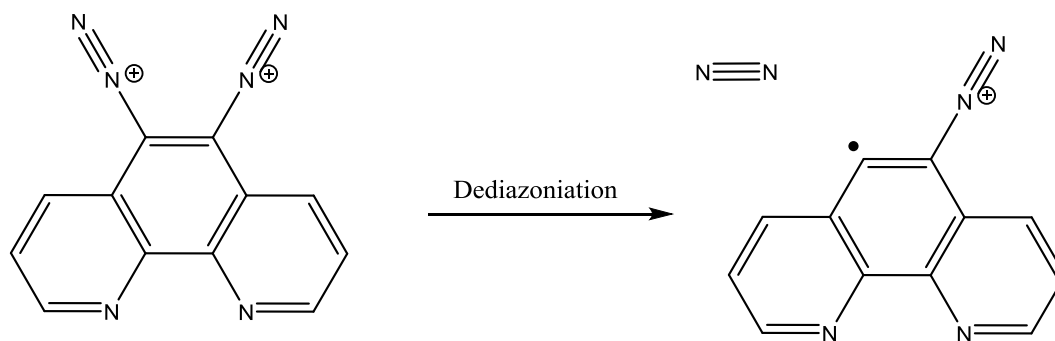


**Figure 1.11. Partial dediazonation reaction of the diazonium ion to generate a radical which will reaction with the carbon support. It is proposed here that further dediazonation will occur once the first radical reactions with the carbon support.**

The reaction seen in Figure 1.11 is the proposed pathway for this work, however it should be mentioned that the reaction of a 1,2 diazonium ion has not been confirmed and may not attach

in this manner. The formation of the radical may not be stable due to the close proximity to the cation.

### 1.5.7 Heat Treatment Conditions

The structure of the active site remains uncertain though there is general agreement that a heat treatment step is required for the synthesis of an active catalyst. The increased activity of materials after heat treatment has been proposed to be attributed to 4 potential causes; improving the dispersion of the ligand, catalyzing a change in the carbon material, coordinating the metal to N, and allowing the M-N complex to integrate into the carbon support.<sup>35</sup> The acceptance of these proposed reasons is varied with some researchers supporting one of the aspects while others agree that it may be a combination of factors.

In addition to the disagreement surrounding the function of the heat treatment, there is still uncertainty regarding the active site and whether the heat treatment impacts the type of linkage that is observed. There is some acceptance that at lower heat treatment temperatures the N<sub>4</sub> structure is maintained while at higher temperatures N<sub>2</sub> is present, though many believe it is likely that a mixture of the two are present.<sup>35</sup> Despite the disagreement, there is evidence that the active site is Fe-N<sub>4</sub>/C, which has been supported by Mössbauer spectroscopy.<sup>56,57</sup> In addition to the Fe-N<sub>4</sub>/C active site, iron carbide and iron oxide have been detected in some materials.<sup>57</sup> Iron oxide has been shown to form in cases where the surface nitrogen is low, and although displays some activity towards the ORR, it is not desirable to have in the materials.<sup>58</sup> Iron carbide on the other hand is completely inactive and is detrimental to the overall functioning of the catalyst.<sup>47</sup>

Heat treatments in literature vary, with the majority remaining in the 600°C to 1000°C range. It is essential to determine the optimal temperature for these syntheses as heating too low or too high can be detrimental to the catalytic activity. The heat treatment largely impacts the level of graphitization; if too low the material will not form correct active sites, and if too high the species involved in the formation of active sites (ex. nitrogen) may be driven off.<sup>47</sup> Figure 1.12 is a representation of the proposed active site following heat treatment in this work, modelled after the slit pore method proposed by Dodelet.<sup>31</sup> The heat treatment requirements will vary in literature depending on the carbon support and method of catalyst synthesis. Ideally this step would be removed in order to make these materials less expensive and easier to synthesize, however it has been determined that it is crucial to have a high temperature heat treatment for

the formation of an active catalyst. Determining a way to reduce or remove the heat treatment step and still maintain an active catalyst would be a big step forward in the area of non-precious metal catalyst.

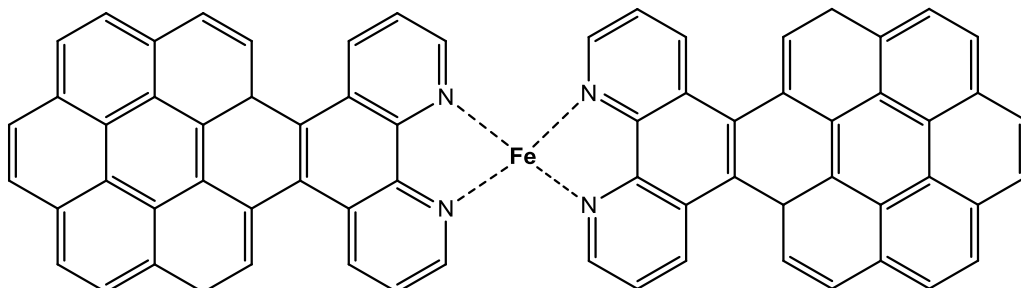


Figure 1.12. Proposed active site modelled after the slit pore method proposed by Dodelet.<sup>31</sup>

## 1.6 Thesis Objective

The ORR is greatly facilitated by the catalytic site, therefore utilizing carbon supports that will best integrate these sites is important. A high surface area carbon with a more disordered structure is ideal as it allows for more incorporation of nitrogen and a greater potential for rearrangement upon heat treatment.<sup>59</sup> The type of nitrogen and method of introduction is an important step to ensure the formation of active catalyst sites. In addition to this, the Fe source and final heat treatment need to be investigated to ensure optimal conditions are being employed.

This work aims to synthesize a cathode material for the ORR with a large amount of well-defined active catalyst sites to improve performance of current fuel cells. The diazonium coupling reaction was used in place of a physisorption method to allow for definition of the active site and high surface area carbons were selected to increase the active site density. Previous studies completed by Paoric<sup>48</sup> compared the benzimidazole and diazonium coupling reactions with work being done to optimize the former synthetic route. This work will expand on the diazonium coupling reaction and optimize the conditions for these catalyst materials.

An additional carbon support, graphene oxide (GO), was used in the absence of a high temperature heat treatment. GO has a high surface area and a very ordered structure. By combining this carbon support with a glycerol reflux to introduce iron, the bridging of the catalyst site may be facilitated and the need for a high temperature heat treatment may be reduced or removed entirely.

Overall, this synthesis method strives eliminate the uncertainty and variety in the active sites of current non-precious metal catalyst by replacing the physisorption method of attachment with a chemical coupling reaction. The aim is to use this procedure to create active catalyst with performance which approaches that of Pt and exceeds current NPMC materials.

# **Chapter 2**

## **Experimental**

## 2.1 Catalyst Synthesis

Catalysts were synthesized in a 3 step process; a nitrogen containing compound (aphen) was coordinated to a carbon support, iron was introduced, and the catalysts were then heat treated. Two series were completed using two different carbon supports, Black Pearls 2000 carbon black (BP) and Ketjen Black EC600JD (KB), with varying ratios of aphen to carbon. The most successful ratios were then selected to optimize the conditions of each step of the process by using different carbon supports, iron salts and heat treatments outlined in the sections below.

### 2.1.1 Precursor Materials

#### 2.1.1.1 5,6-diamino-1,10-phenanthroline (Aphen)

Aphen was synthesized by colleagues using a method as reported by Pauric et al.<sup>48</sup> Samples were used as received.

#### 2.1.1.2 Iron Salts

Iron(II) acetate and Iron(III) chloride salts were used as purchased from Sigma Aldrich.

#### 2.1.1.3 Carbon Supports

BP 2000 carbon black was donated by Cabot Corporation and used as received.

KB (EC600JD) was purchased from Akzo Nobel Surface and used as received.

Graphene oxide was synthesized using a modified Hummers method as reported by Dimiev et al.<sup>60</sup> 1 g of graphite flakes was stirred with 140 ml of concentrated sulphuric acid (Fischer Scientific) for 10 minutes. 1 g of potassium permanganate (Sigma Aldrich) was added after the 10 minutes and the solution continued to be stirred. 3 Additional 1 g aliquots of  $\text{KMnO}_4$  were added over 3 days with continued stirring. After all additions of  $\text{KMnO}_4$  the solution was quenched with 100 mL of a 10% HCl solution and stirred overnight. The solution was then filtered, rinsed with DI and dried in the oven overnight.

### 2.1.2 Diazonium Coupling of Aphen to Carbon

A diazonium coupling reaction was used to attach aphen to BP and KB as adapted from previous work from our group.<sup>48</sup> 200 mg of BP or KB was added to a stirring solution of 1 equivalent aphen in 10 ml deionized water, 4 equivalents sulfuric acid and 2 equivalents sodium nitrite (Sigma Aldrich; superfine flowing, 99.5%). The ratio of aphen to BP was varied according to Table 2.1, and the ratio of aphen to KB was varied according to Table 2.1. The solution was stirred for

30 minutes at room temperature and the product was rinsed with DI and collected via suction filtration using a glass frit. The material was placed in a 100 °C oven and dried overnight. BP treated with aphen will now be referred to as BPS1, BPS2, BPS3, BPS4, and BPS5 according to the order of increasing ratio. KB treated with aphen will now be referred to as KBS1, KBS2, KBS3, KBS4, and KBS5 according to the order of increasing ratio.

Chemical attachment of aphen to graphene oxide was completed as stated above. For all graphene oxide samples a ratio of 1.2 mmol aphen/g carbon was used. Graphene oxide samples treated with aphen will now be referred to as GOS4.

**Table 2.1. Black Pearls 2000 series ratios for samples 1 through 5.**

<b>Sample Identification</b>	<b>Ratio (mmol aphen/g BP)</b>
BPS1	0.343
BPS2	0.604
BPS3	0.871
BPS4	1.18
BPS5	1.37

**Table 2.2. Ketjen Black EC600JC series ratios for samples 1 through 5.**

<b>Sample Identification</b>	<b>Ratio (mmol aphen/g KB)</b>
KBS1	0.359
KBS2	0.586
KBS3	0.935
KBS4	1.24
KBS5	1.51

### **2.1.3 Iron Coordination**

#### **2.1.3.1 Iron(III) Chloride**

Each modified carbon was soaked in a 10 mM solution of iron(III) chloride hexahydrate and deionized water for 48 hours to coordinate iron to the aphen-carbon structure. The product was filtered and dried as before and then ground into a fine powder. Samples that have been soaked in iron(III) chloride will be denoted with Fe after the sample identification (e.g. BPS4Fe denotes a sample of carbon BP reacted with aphen and soaked in iron(III)chloride).

#### **2.1.3.2 Iron(II) Acetate**

Each modified carbon BP sample was soaked in a 10 mM solution of iron(II) acetate in either a 50:50 mixture of deionized water and isopropyl alcohol (IPA) or deionized water (DI) alone. The procedure was followed as stated above. Samples that have been soaked in iron(II) acetate with

DI:IPA will be denoted with FeA after the sample identification and those that have been soaked iron(II) acetate with DI alone will be denoted with FeB. (e.g. BPS4FeA indicates a sample of carbon BP reacted with aphen and soaked in iron(II) acetate and DI:IPA while BPS4FeB denotes a sample of carbon BP reacted with aphen and soaked in iron(II) acetate and DI only).

Select samples that were soaked in iron(II) acetate were further processed to remove any excess Fe that may have been present. These samples (following heat treatment) were soaked in a sulphuric acid solution at pH 0.5 for 24 hours, rinsed, filtered and dried. Sample which have been treated to leach out Fe are denoted with an L following the sample name. (BPS4FeA700L denotes a sample of carbon BP reacted with aphen and soaked in iron(II) acetate and DI:IPA, heat treated at 700°C and acid leached).

To avoid the acid leaching step, a few samples were soaked in a 0.35 mM solution of iron(II) acetate instead of the 10 mM solution. These samples were prepared in a 50:50 mixture of DI and IPA. Samples that have been soaked in the lower concentration of iron(II) acetate are denoted with the word “Low” following the sample name. (e.g. BPS4FeLow700 indicates a sample of carbon BP reacted with aphen and soaked in 0.35 mM iron(II) acetate and DI:IPA and heat treated at 700°C).

#### **2.1.4 Heat Treatment**

50 mg of each sample were pyrolyzed under nitrogen at a specific temperature for two hours in a tube furnace (Barnstead/Thermolyne 21100). Samples that have undergone a heat treatment will be hereafter denoted with “FeXXX” after the sample identification, where XXX refers to the heat treatment temperature on the Celsius scale (e.g. BPS4Fe700 refers to a sample of carbon BP reacted with aphen and soaked in iron(III) chloride and heat treated at 700°C).

Two heat treatment series were completed, one for BP sample set and one for KB sample set. The following four heat treatment temperatures were used: 600 °C, 700 °C, 800 °C, and 900 °C. Any samples outside of the heat treatment series were pyrolyzed at 700 °C.

#### **2.1.5 Glycerol Reflux Treatment**

Reaction of graphene oxide with iron(III) chloride was completed using a reflux in glycerol. 10 mL of a 10 mM iron(III) chloride solution was prepared in a round bottom flask and attached to a reflux condenser and placed in a sand bath. 100 mg of GOS4 was added to the round bottom flask as the solution was stirring. The temperature was maintained at 270 °C for 3 hours. The

reaction was then cooled, filtered and dried overnight in the oven. This sample will be referred to as GOS4Gly.

## 2.2 Characterization

All samples were characterized using a combination of physical and electrochemical measurements to assess structure, activity and efficiency.

### 2.2.1 Electrochemical Measurements

A Pine Instruments AFCBP1 bipotentiostat or WaveDriver 20 bipotentiostat/galvanostat controlled using AFTERMATH software was used for all electrochemical measurements. All measurements were performed in a 0.5 M H<sub>2</sub>SO<sub>4</sub> (aq) at room temperature using a 3 electrode cell that employed a saturated calomel or silver silver chloride reference electrode, Pt counter electrode, and glassy carbon working electrode. All potentials reported here have been corrected to the reversible hydrogen electrode (RHE).

#### 2.2.1.1 Preparation of Inks and Deposition

300  $\mu$ L of a 5% Nafion<sup>®</sup> solution and 200  $\mu$ L isopropyl alcohol/deionized water (50:50 V/V) were added to 10 mg of each catalyst. Following a 30 min sonication, 5  $\mu$ L were deposited onto glassy carbon disk and dried for 5 minutes yielding a catalyst loading of 0.53 mg/cm<sup>2</sup>. A rotating ring disk electrode (RRDE) was used with a 5 mm glassy carbon disk and a platinum ring with a 7.5 mm inner diameter and 8.5 mm outer diameter. (Pine Instruments)

A loading study was also completed by varying the amount of carbon used to make the inks. For this series inks were made with 1.25 mg, 2.5 mg, 5 mg, and 10 mg of carbon dispersed in the solution indicated above.

#### 2.2.1.2 Cyclic Voltammetry

Cyclic voltammograms (CVs) were obtained to observe changes in activity in the absence of O<sub>2</sub> by placing the working electrode in an N<sub>2</sub> purged solution with the conditions listed in Table 2.3. All data was recorded at four different scan rates; 100 mV/s, 50 mV/s, 20 mV/s, and 10 mV/s. All presented data was obtained using a scan rate of 10 mV/s unless otherwise specified.

Table 2.3. Conditions for cyclic voltammetry measurements

Parameter	Value
Number of Segments	4
Initial Potential	0.4 V
Initial direction	Rising
Upper Potential	1 V
Lower Potential	-0.2 V
Final Potential	0.4 V

### 2.2.1.3 Linear Sweep Voltammetry and Dual Electrode Cyclic Voltammetry

Linear sweep voltammograms (LSVs) were obtained to assess activity and efficiency of the catalyst materials using conditions listed in table 4 where applicable. Following a background LSV under N<sub>2</sub>, all data was recorded under O<sub>2</sub> at five different rotation rates; 100 rpm, 400 rpm, 900 rpm, 1600 rpm, and 2500 rpm. All presented data was obtained at a rotation rate of 900 rpm unless otherwise specified. Limiting current is determined from the point at which the measurements plateau and the onset potential is defined as the potential at 5% of the limiting current.

RRDE collection experiments were used to determine number of electrons transferred and hydrogen peroxide measurements. The ring potential was held at 1.2 V to oxidize any evolved H<sub>2</sub>O<sub>2</sub>. The number of electrons and percent hydrogen peroxide was calculated using this data and equations 2.1 and 2.2. I<sub>R</sub> is the faradaic current at the ring, I<sub>D</sub> is the faradaic current at the disk, n is the number of electrons observed in reaction, and N is the collection efficiency (0.19).

$$\%H_2O_2 = 100 * \left(4 - \frac{n}{2}\right) \quad 2.1$$

$$n = 4 * \frac{I_D}{\left(I_D + \left(\frac{I_R}{N}\right)\right)} \quad 2.2$$

### 2.2.2 Thermogravimetric Analysis (TGA)

TGA was used to determine the composition of the samples by analyzing the temperatures at which mass losses occur. A TA instruments SDTQ600 thermogravimetric analyzer was used for all samples. Samples were run under air at a ramp rate of 20°C/min to a temperature of 100°C. All data was processed using the TA thermal Advantage Analysis software.

### 2.2.3 Raman Spectroscopy

Raman spectroscopy was used to determine the structural changes in the carbon before and after heat treatment. A Renishaw Raman Imaging Microscope System 2000 equipped with an argon ion (514 nm) laser was used for all samples. Data was collected and processed using the Renishaw-WiRE Gramsn software. Calculation of the  $I_G/I_D$  ratio was completed using TableCurve 2D version 5.01 by fitting 4 Gaussian curves centred around the G band ( $\sim 1590\text{ cm}^{-1}$ ), the D band ( $\sim 1315\text{ cm}^{-1}$ ), and the D3 band ( $\sim 1522\text{ cm}^{-1}$ ) and D4 band ( $\sim 1169\text{ cm}^{-1}$ ). These peaks results from graphitic carbon, disordered carbon, amorphous contained within a graphitic structure and  $\text{Sp}^2$ - $\text{Sp}^3$  C-C bonds respectively.

### 2.2.4 X-Ray Photoelectron Spectroscopy (XPS)

Samples were sent to Queen's University for XPS measurements. A Thermo Instruments 310 – F Microlab equipped with a monochromatic Mg K $\alpha$  X-ray source ( $h\nu = 1253.6\text{ eV}$ ) was used for all samples. A Gaussian shaped profile with a Shirley background was used to fit all the data. Peak broadening was limited to 2 eV.

### 2.2.5 Scanning Electron Microscopy (SEM) and Transmission Electron Microscopy (TEM)

The microstructure and nanostructure of the catalyst materials were investigated using SEM and TEM respectively. A JEOL JSM 6400 instrument was used for all SEM measurements at UOIT. Samples were sent for TEM measurements to either the University of Waterloo or Western University. Western employs a Zeiss Axioskop2 MAT instrument while Waterloo uses a Zeiss Libra 200 MC microscope.

### 2.2.6 Brunauer-Emmett-Teller Analysis (BET)

BET analysis was used to investigate changes in the surface area and pore sizes/volume before and after heat treatment. A Quantachrom Instruments Nova 1200e Surface Area and Pore Size Analyzer was used for all samples. Data was collected and processed using the NovaWin software.

**Chapter 3**

**Detailed Study of Fe-N/C  
Catalysts Prepared by the  
Diazonium Coupling  
Reaction**

### 3.1 Method Validation

Work was done to ensure that the data obtained would be accurate and reliable. In order to do so, standard electrochemistry data was collected for a standard Pt based catalyst and compared to literature. Johnson Matthey HiSpec 3000 20% Pt (JM20%Pt) on carbon black (Alfa Aesar) was used as a standard material to validate the electrochemical methods.

The electrochemical surface area (ECSA) of platinum can be calculated from the hydrogen desorption peak present in the CV obtained under nitrogen. The integrated charge under this peak has been shown to directly relate to the surface area of Pt ( $210 \mu\text{C} = 1\text{cm}^2$ ).<sup>61</sup> Figure 3.1 shows the CV recorded at a scan rate of 10 mV/s in an  $\text{N}_2$  saturated solution of 0.5 M  $\text{H}_2\text{SO}_4$  for JM20%Pt. The area under the hydrogen desorption peak, shown in Figure 3.1) was calculated using the AfterMath software. Using the ink loading of the Pt catalyst (5  $\mu\text{L}$  loading of a 0.02 mg/ $\mu\text{L}$  solution) and the integrated charge, the ECSA of the standard material was found to be  $25.8 \text{ m}^2/\text{g}_{\text{Pt}}$ . It has been reported that the ECSA of JM20%Pt is approximately  $41.6 \text{ m}^2/\text{g}_{\text{Pt}}$ .<sup>61</sup> The deviation from literature is due to the method of ink preparation; a higher amount of Nafion was utilized in the inks prepared for this study which would lower the ECSA measurements.

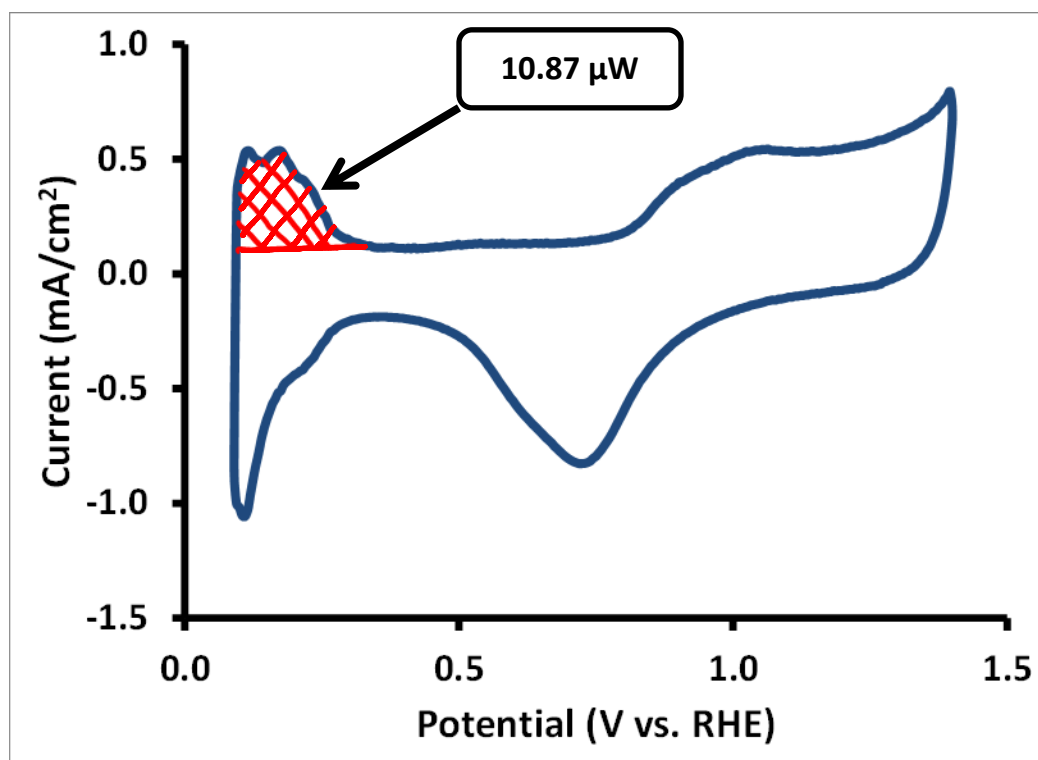


Figure 3.1. CV results for Johnson Matthey 20% Pt on carbon black. Measurements were obtained at 10 mV/s in an  $\text{N}_2$  saturated 0.5M sulphuric acid solution.

Rotating disk measurements were completed at 5 different rotation rates (100 rpm, 400 rpm, 900 rpm, 1600 rpm, and 2500 rpm) in an O<sub>2</sub> saturated 0.5M H<sub>2</sub>SO<sub>4</sub> solution and used to construct a Koutecky-Levich plot to compare the mechanism of the reaction to theoretical measurements. Figure 3.2 shows the linear sweep measurements for the standard materials at each rotation. The expected change in the limiting current as the rotation rates are varied is observed. As the rotation rate is increased, mass transport losses become less as the diffusion layer becomes smaller.

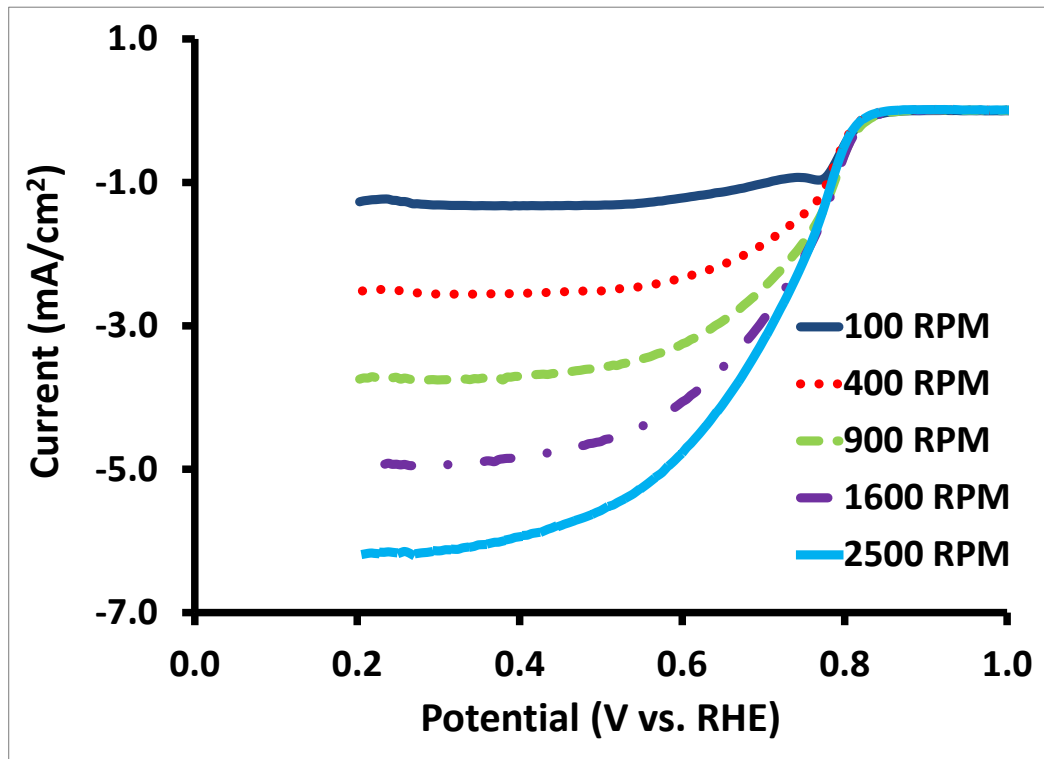


Figure 3.2. Rotating disk measurements for JM20%Pt at various rotation rates in an O<sub>2</sub> saturated 0.5M sulphuric acid solution.

Theoretical curves were calculated for the 4 electron and 2 electron oxygen reduction reaction pathways using the Levich equation (Equation 3.1). For each rotation, two limiting currents were calculated; one for the two electron process and one for the four.

$$I_L = (0.620)nFAD^{\frac{2}{3}}\omega^{\frac{1}{2}}\nu^{-\frac{1}{6}}C \quad \text{Equation 3.1}$$

$I_L$  is the Levich current (limiting current),  $n$  is the number of electrons transferred (2 or 4), and  $\omega$  is the rotation rate in rad/s. The remaining variables,  $F$  (Faraday's constant),  $A$  (electrode area),

D (diffusion coefficient),  $\nu$  (kinematic viscosity), and C (analyte concentration), were constant for all calculations and were  $9.65 \times 10^{-4}$  cm<sup>2</sup>/s,  $0.196$  cm<sup>2</sup>,  $1.93 \times 10^{-5}$  mol/cm<sup>3</sup> respectively.<sup>62</sup> Figure 3.3 compares JM20%Pt to the theoretical two and four electron curves. It can be seen that the standard material follows the 4 electron pathway as it almost overlaps directly with the theoretical curve. Both the ECSA data and Koutecky-Levich analysis indicate that the standard material tested in the lab corresponds to Pt materials in literature. Overall the electrochemical measurements were accurate and show that the data collected in this work is reliable.

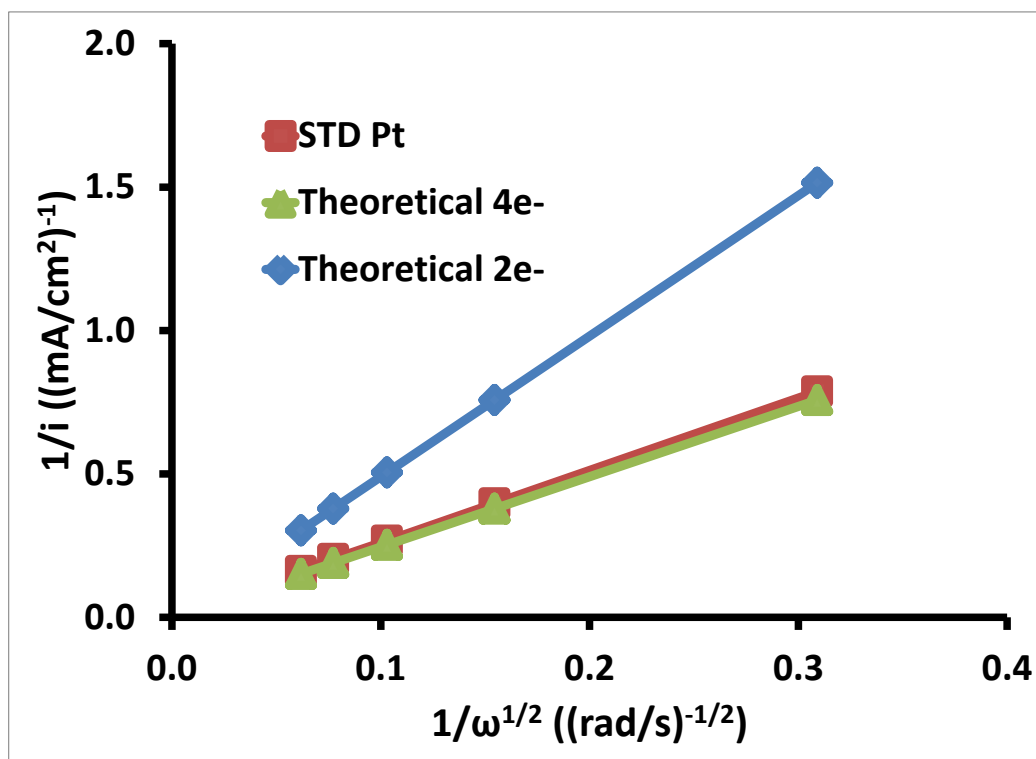


Figure 3.3. Koutecky-Levich analysis for JM20%Pt compared to the theoretical 2 and 4 electron oxygen reduction processes.

### 3.2 Non-Precious Metal Catalyst Studies

With the electrochemical methods confirmed, further aspects of the synthesis were investigated and optimized. Impacts of the heat treatment temperature and ink concentration were explored with the optimal conditions being employed for all catalysts synthesized in this study.

#### 3.2.1 Optimization of Heat Treatment Temperature

Heat treatment temperatures vary in literature and are dependent on various factors such as the base carbon used as well as the reaction conditions. In order to determine the optimal heat

treatment temperature for our synthetic method, both the BP and KB series were heat treated at various temperatures, post diazonium coupling (1.2 mmol apen/g carbon) and Fe soaking. Figure 3.4 shows the ORR activity for each series with varying temperature. It can be seen that although the onset potential for the BP set is roughly the same for all but the 600°C treatment, a better limiting current is achieved at 700 °C, indicating that there are more active sites present. Regarding the KB series, it is clearly evident that 700 °C is the ideal temperature. Overall this study indicates that the optimal temperature is 700 °C for both the BP and KB series.

Figure 3.5 illustrates the effect of the different heat treatment temperatures on the hydrogen peroxide production. The hydrogen peroxide production was low for all samples in the BP series treated above 600°C, which follows the same trend as the onset potentials. The main difference is in the limiting current which supports 700°C as the optimal heat treatment temperature for the synthesis. In terms of the KB series, it is clear that the onset potential, limiting current, and hydrogen peroxide production for the samples treated at 700°C exceeded that of the others in the series.

Overall the 700°C heat treatment temperature yielded the best performance from both series and was used for the remainder of the heat treatments. The importance of using an optimal temperature is stressed in this study as variations of 100°C result in loss of performance.

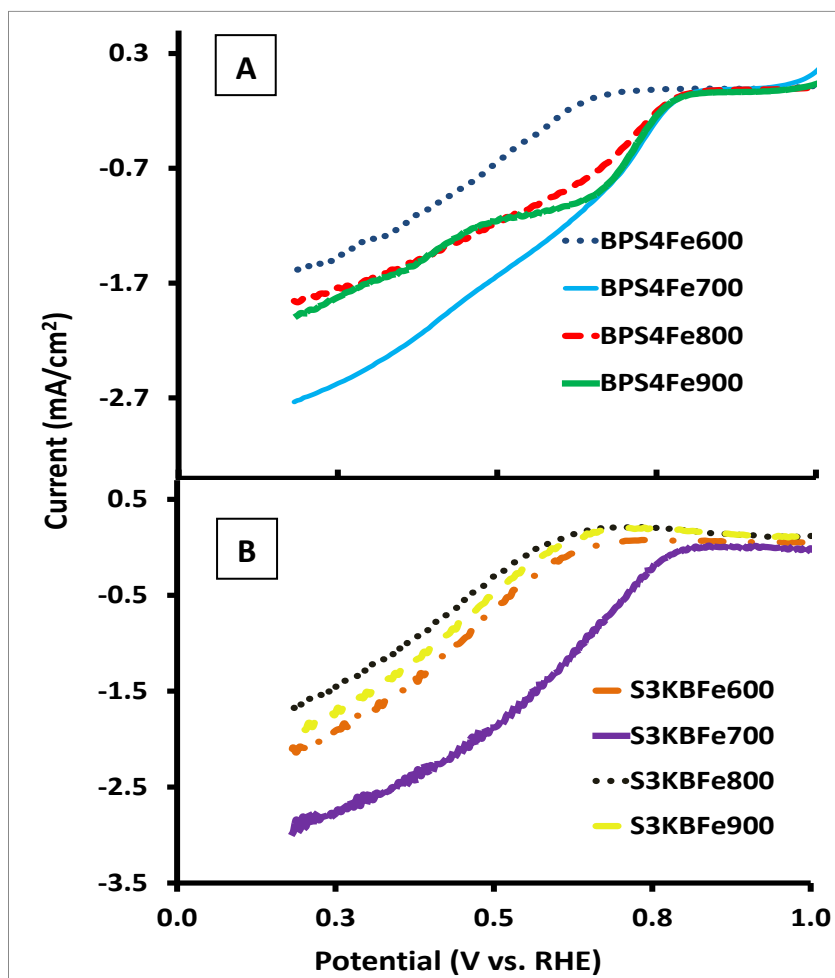


Figure 3.4. ORR activity for (A) BPS4Fe and (B) KBS3Fe treated at four different temperatures to determine optimal heat treatment conditions. Measurements were obtained at 900 rpm in an O<sub>2</sub> saturated 0.5M sulphuric acid solution.

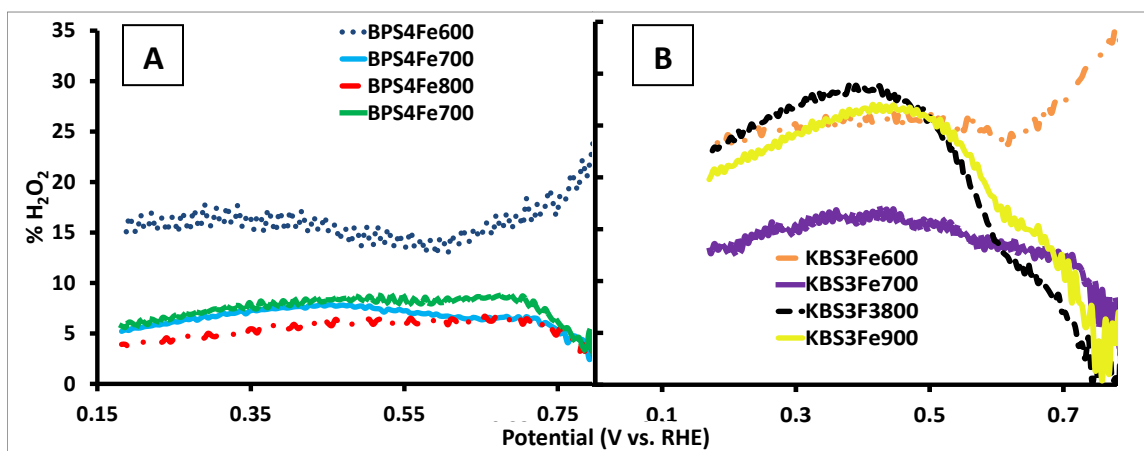


Figure 3.5. Hydrogen peroxide production of (A) BPS4Fe and (B) KBS3Fe treated at four different temperatures to determine optimal heat treatment conditions.

### 3.2.2 Impact of Catalyst Ink Concentrations

The effects of catalyst loading on the electrode, and consequently catalyst layer, were investigated. Inks were prepared as indicated in section 2.2.1.1 with varying amounts catalyst material. The concentration of each prepared ink varied which impacted the ink loading on the glassy carbon electrode. Figure 3.6 A and B compare the ORR activity and hydrogen peroxide production for the different ink compositions. These results clearly indicate that the catalyst loading will influence the activity, efficiency, and hydrogen peroxide production. In general, the higher the loading the more active and efficient the catalyst, which correlates to a lower hydrogen peroxide production. The efficiency, activity, and hydrogen peroxide production of the highest loading gave the best results; therefore this loading was used for all future catalyst inks.

In terms of the activity, it is possible that the lower loadings are impacted by a higher amount of binder (Nafion). In preparing the different ratios, the catalyst mass was increased but the solvent remained constant. The higher amount of Nafion in the low loadings may result in issues transporting  $O_2$  to the active sites. With the higher loadings of the catalyst, there will be a lower ratio of Nafion and therefore better access to the active sites and fewer transport issues. The same issue impacts the limiting current and therefore the efficiency of the materials; if the oxygen is having a harder time accessing the active site in the lower loadings then the efficiency will also suffer.

It is likely that the increased area and thickness of the inks allows for an artificially low hydrogen peroxide reading as this species can be react at another catalyst site before leaving the catalyst layer and being detected by the electrode. However it is possible that even the 4 electron pathway involves a hydrogen peroxide intermediate which means that as long as the hydrogen peroxide can be reduced to water at another catalytic site the catalyst is still successful. Hydrogen peroxide is a very strong oxidizer and it is when it is able to interact with parts of the catalyst that is not the active site and cause degradation of the catalyst.

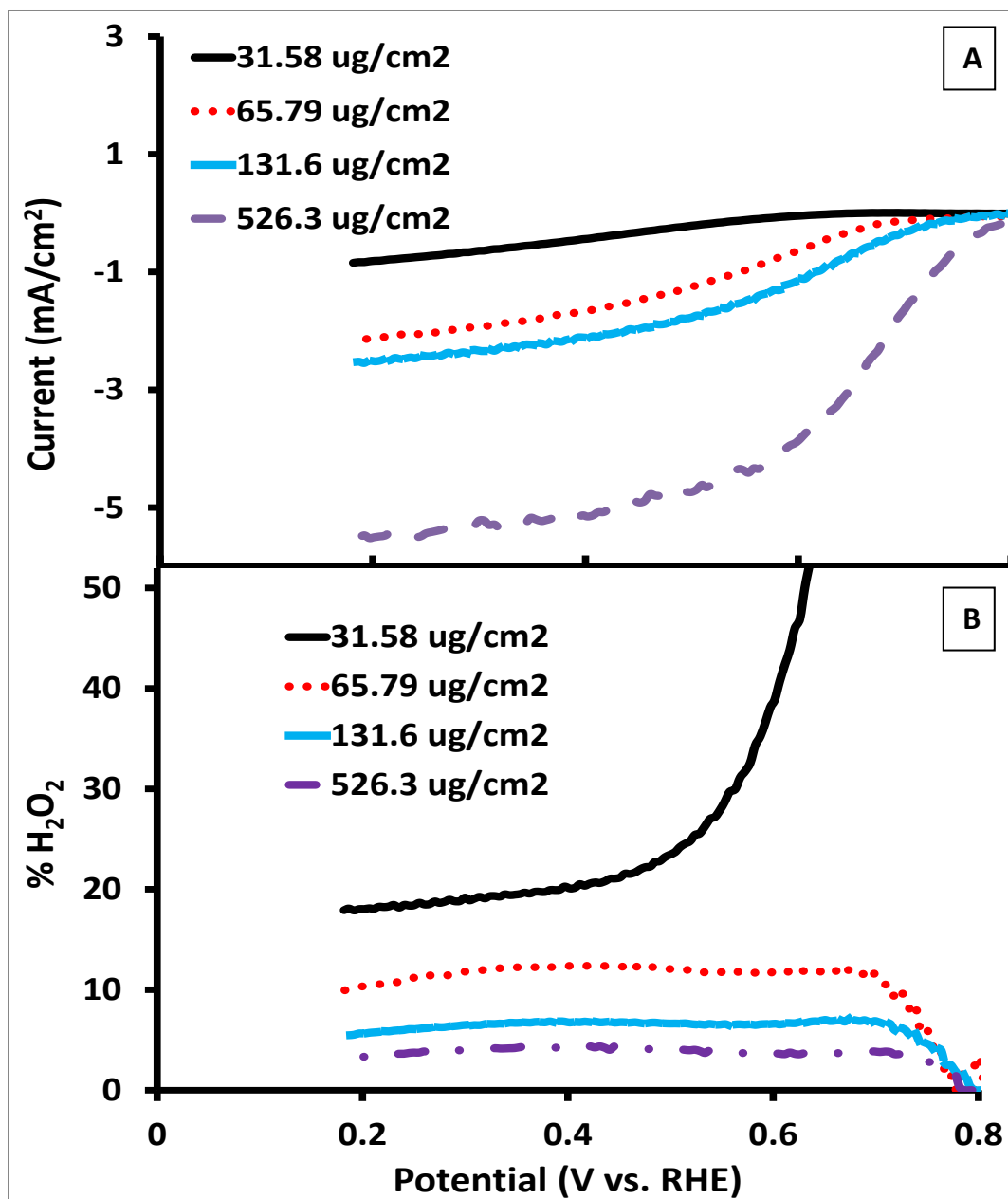


Figure 3.6. Comparison of performance of BPS4Fe700 at different catalyst loadings as seen by the (A) ORR activity and (B) hydrogen peroxide production

### 3.3 Results & Discussion: Black Pearls Series Catalysts

#### 3.3.1 Impact of Aphen Loading

One of the key aspects of NPMCs is the nitrogen content, and it will greatly impact the overall performance of the catalyst. The impact of aphen loading, linked to the nitrogen content, was studied to determine if there is an optimal amount of aphen that can be coupled to the carbon

support. Five different ratios were prepared by varying the amount of apphen on the carbon support as described in section 2.1.2.1. These materials were characterized using a variety of techniques which will be discussed in this section.

Upon coordination to the carbon surface it is predicted that the apphen will undergo the redox process as shown in Figure 3.7, resulting in a wave at 0.65 V vs. RHE.<sup>48</sup> CVs obtained for catalyst materials post diazonium coupling all display a symmetric peak occurring at 0.65 V vs. RHE which can be used to assess the effectiveness of the coupling reaction.

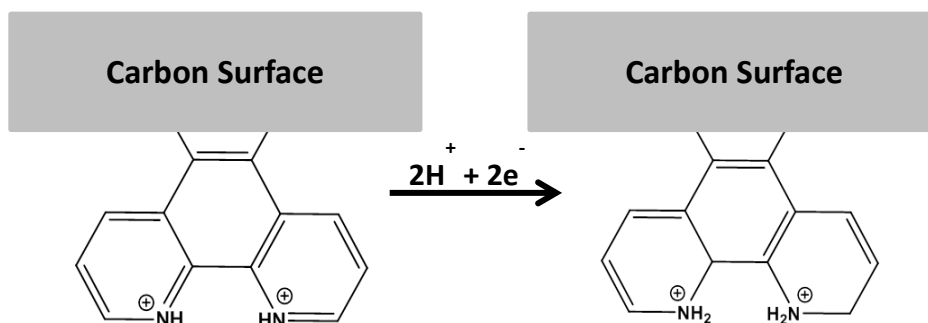


Figure 3.7. Proposed redox activity of the apphen groups on the carbon surface resulting in the peak seen at 0.65 V vs. RHE in CV measurements.

Figure 3.8 shows the CVs obtained for the BP series and clearly displays the changes in peak height with varying apphen loadings. Initially the peaks heights increase with increasing ratios which corresponds to a higher amount of redox active apphen present on the carbon surface. The peak heights then plateau and a slight decrease is observed.

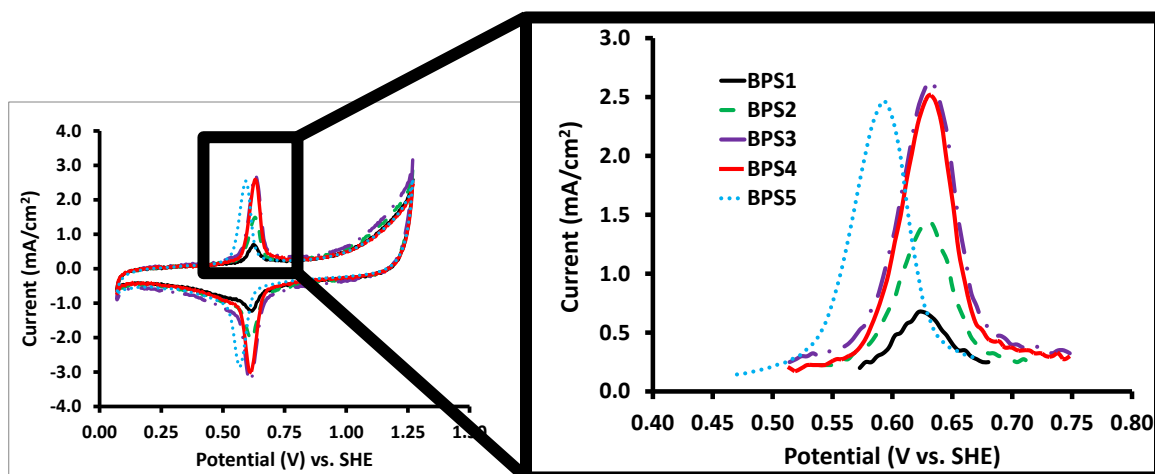


Figure 3.8. Cyclic voltammograms for each prepared ratio of BP and Aphen. Measurements are recorded at a scan rate of 10 mV/s in an N<sub>2</sub> saturated 0.5 M sulphuric acid solution.<sup>63</sup>

In order to clearly see the relationship between these two aspects, the area under the oxidative peak was measured and from this the charge transferred was calculated (Figure 3.9). Initially there is a rise in transferred charge as the Aphen amounts are increased and eventually it plateaus (0.9 mmol aphen/g carbon) and then decreases (1.5 mmol aphen/g carbon). Although this could indicate that the higher amounts of Aphen are detrimental to the catalyst material, this may not necessarily be the case. These measurements are limited as they are only able to detect what is electrochemically available and active.

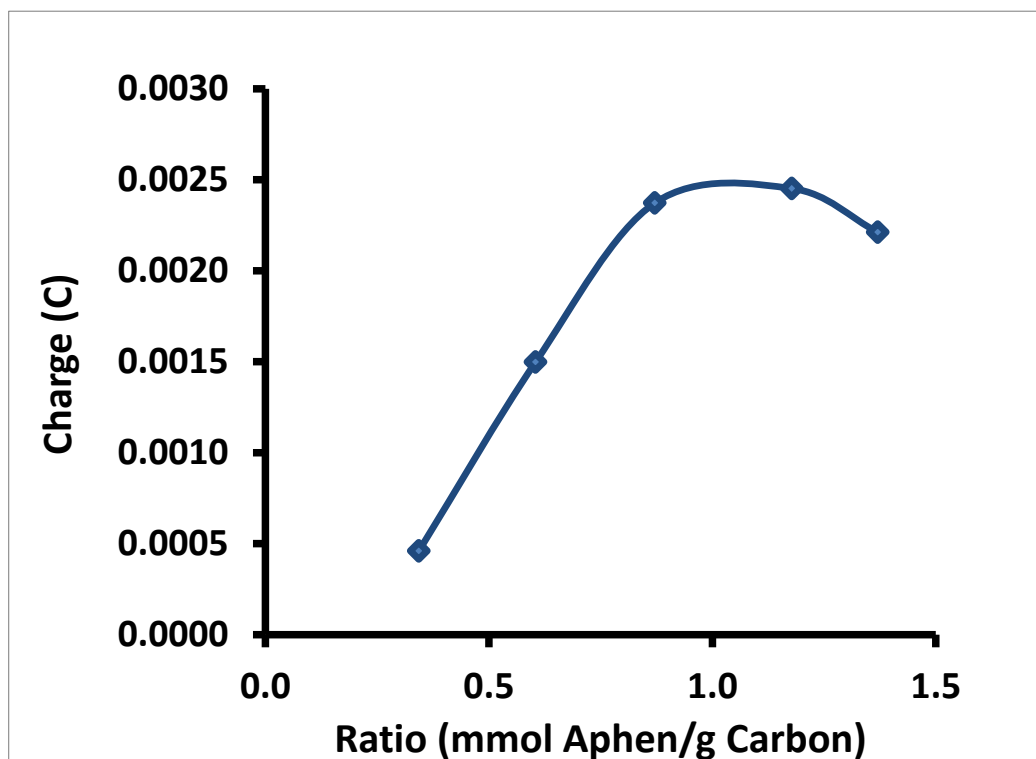


Figure 3.9. Relationship between charge transferred and ratio for BPS1-BPS5.

The diazonium coupling reaction is very effective at coupling diazonium ions to carbon support, but it is also possible to couple the diazonium ions to aphen molecules already attached to the carbon surface<sup>64-66</sup> (Figure 3.10).

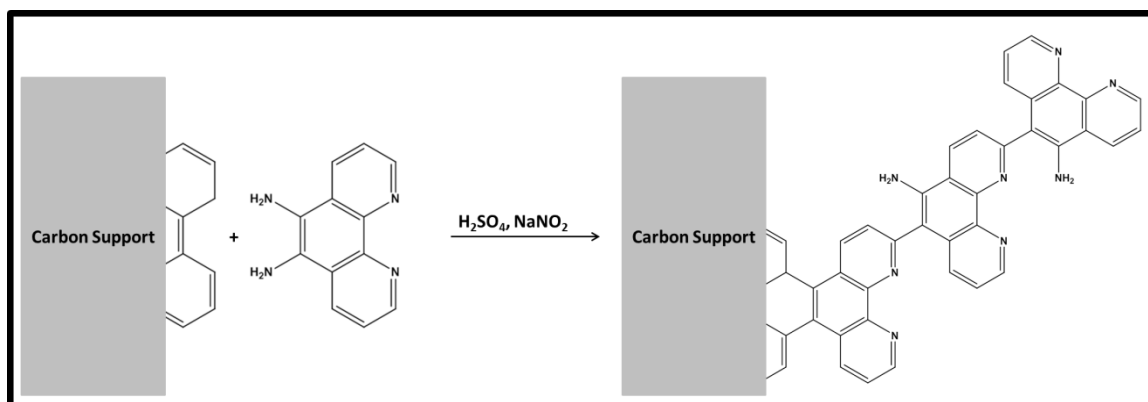


Figure 3.10. Proposed mechanism of the multilayer formation from the diazonium coupling reaction.

This results in a multilayer formation that is not electroactive impacting the perceived amount of apheh bonded to the surface.<sup>67</sup> Therefore, it is likely that at higher ratios more apheh was loaded but it is not detectable by the electrochemical measurements used in this study.

Once samples were soaked in  $\text{FeCl}_3$  and heat treated, it can be seen that there is a decrease in the peak around 0.65 V vs. RHE (Figure 3.11). This indicates that the species responsible for these waves has been either changed or evolved off during heat treatment. However, small peaks remaining corresponding to small amounts of apheh that remained intact.

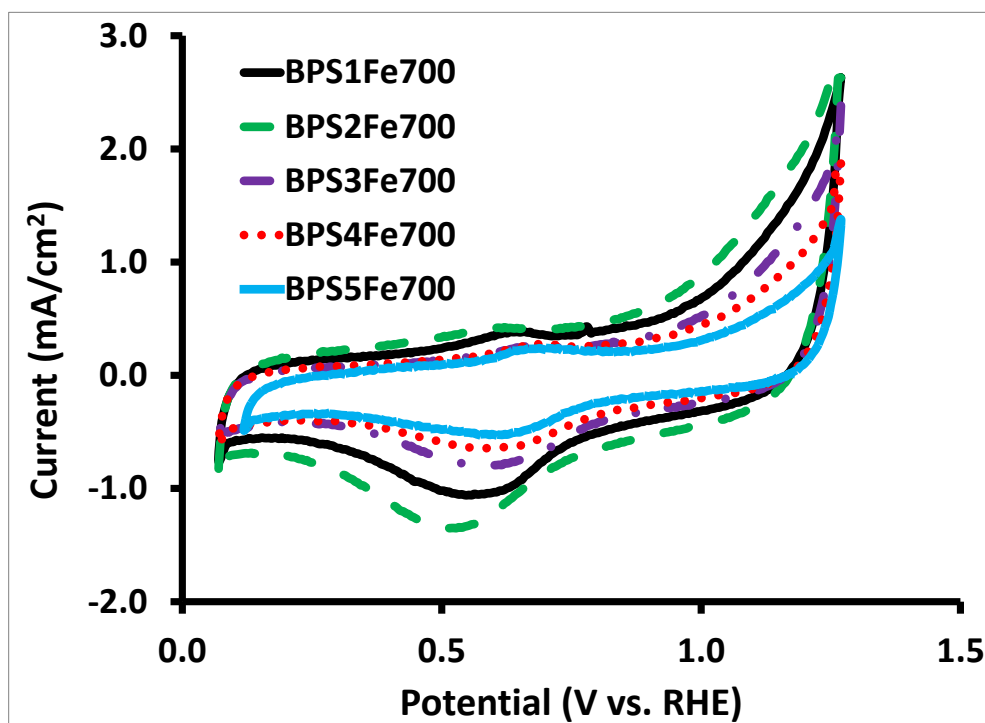


Figure 3.11. Cyclic voltammograms for each prepared ratio of BP with Aphen and iron following heat treatment. Measurements were obtained at a scan rate of 10 mV/s in an  $\text{N}_2$  saturated 0.5 M sulphuric acid solution.

ORR activity is assessed using the onset potential which is the potential at which the material begins to catalyze the ORR. Onset potential is determined by calculating the potential that occurs at 5% of the limiting current.<sup>68</sup> The limiting current is the current at which the measurements plateau and gives a measure of the efficiency of the catalyst. Figure 3.12 illustrates the change in both the activity and efficiency measured for BPS1 to BPS5 (Figure 3.12A) and BPS1Fe700 to BPS5Fe700 (Figure 3.12B). The best onset potential obtained for this series was 0.78 V vs. RHE for BPS4Fe700 which also gave the best limiting current of  $-5.52 \text{ mA/cm}^2$ .

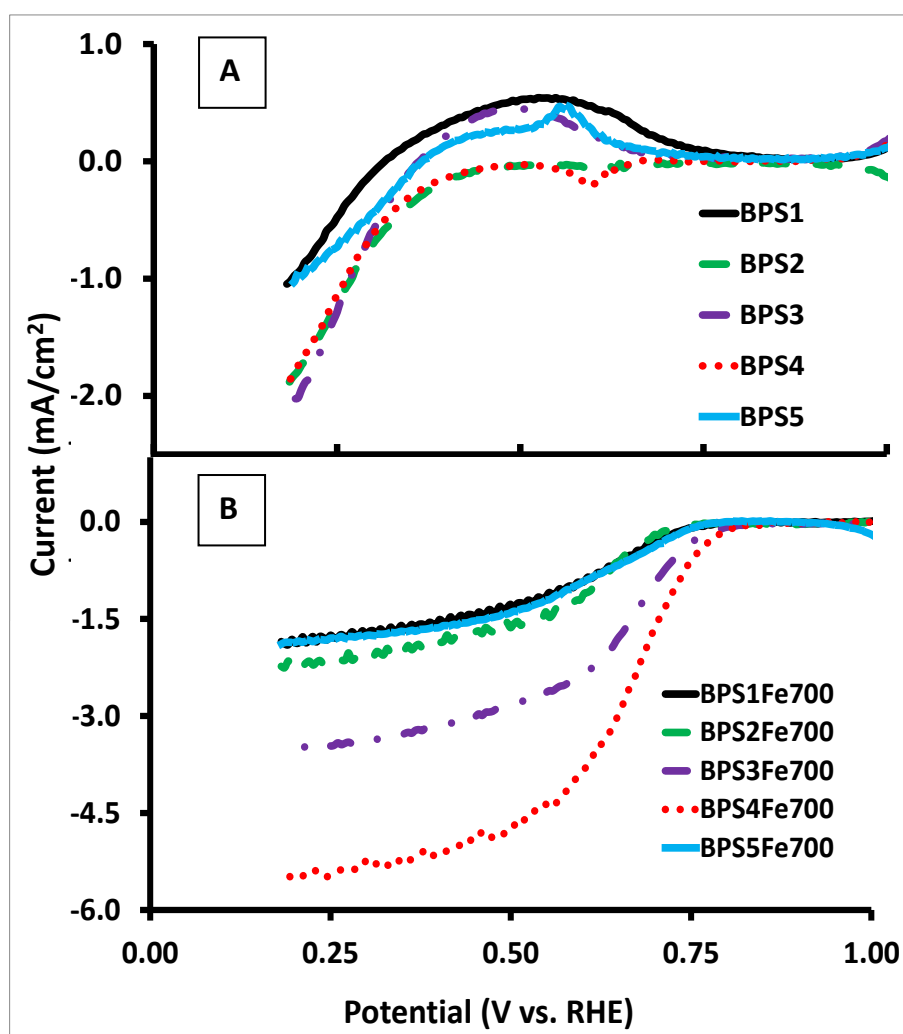


Figure 3.12. Change in ORR activity before (A) and after (B) treatment. Measurements were performed at 900 RPM in an  $\text{O}_2$  saturated 0.5 M sulphuric acid solution.

Figure 3.13 shows the relationship between the onset potential of BPS1Fe700 to BPS5Fe700 and their respective ratio of initial aphen loading. A large gain is seen between BPS3Fe700 and BPS4Fe700 that was not observed for BPS3 and BPS4. This indicates that it is likely that higher loadings of Aphen are creating multilayer structures as the onset potential continues to increase after the plateau we see in Figure 3.9. It is possible that the aphen that was not initially covalently bound to the carbon surface is still able to form active sites and upon heat treatment. Although this seems plausible for BPS4Fe700, there is still a drop in activity for BPS5Fe700 indicating that high amounts of aphen are ineffective. It is likely that at high aphen to carbon ratios that some aphen form a monolayer on carbon as described, but the multilayer side reaction is more prevalent. This indicates that these multilayers are less thermally stable than the monolayer and that the monolayer is more effective at forming active sites. An alternate, thermally unstable, polyaniline type aphen linkage has been observed in previous work, which can be detected by a peak that appears at 0.65 V vs. RHE in CV measurements under N<sub>2</sub>.<sup>48</sup> This peak was not seen in this work indicating that the primary contribution to the thermal loss of aphen is due to the multilayer formation and not the polyaniline type linkage.

The formation of the multilayer creates a scenario similar to that of the physisorption method of synthesizing these materials. The excess aphen present in the multilayer is not chemically bound to the carbon surface directly, and if active sites are formed, it is more difficult to define the structure. The difference in the onset potential between BPS4Fe700 and BPS5Fe700 is very small and it is possible that small differences may be due to the precision of the onset potential determinants.

Further supporting the idea that excess aphen is detrimental, is the lack of correlation between the onset potential and the limiting current (Figure 3.14). Although there is a drop in onset potential between BPS4Fe700 and BPS5Fe700, the latter sample still yields the second highest onset potential of the series. Despite the reasonable onset potential, the limiting current achieved by BPS5Fe700 is the second worst of the series. This indicates that although active sites are forming, there are far fewer of them than expected considering the increase in ratio. This can be accounted for if there is a multilayer formation that is thermally unstable. In this case there would be a loss of the extra aphen rather than active site formation.

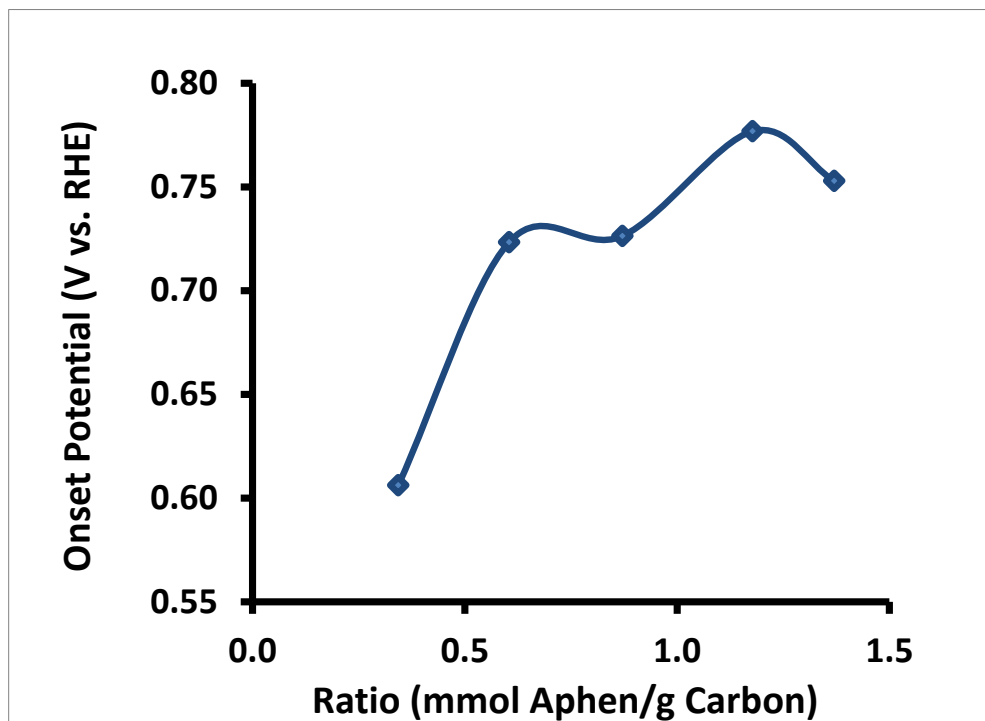


Figure 3.13. Relationship between onset potential and ratio for BPS1Fe700 to BPS5Fe700.

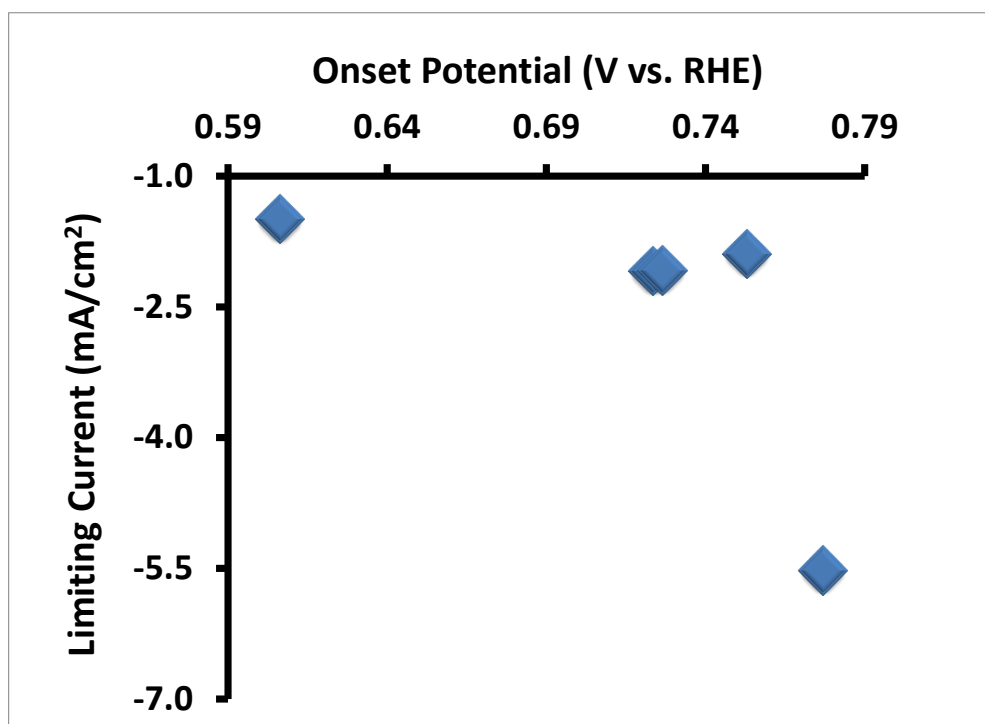


Figure 3.14. Comparison of the limiting current and onset potential for BPS1Fe700 to BPS5Fe700.

Overall the diazonium coupling reaction was successful in the modification of the BP support. Increasing the ratio of aphen to BP resulted in detection of higher amounts of electrochemically active aphen for the lower ratios; however at higher ratios multilayers are forming, potentially preventing detection of all aphen present. These multilayers are not as thermally stable as the monolayers and during heat treatment will either form additional active sites or evolve off. Assessment of the activity of the BP catalyst continued with analysis of the amount of hydrogen peroxide produced and the possible mechanism used for the ORR. The number of electrons and the amount of hydrogen peroxide produced was calculated from the RRDE measurements using Equations 2.1 and 2.2. Figure 3.15 summarizes the hydrogen peroxide data showing trends for BPS1 to BPS5 (Figure 3.15A) and BPS1Fe700 to BPS5Fe700 (Figure 3.15B). It can be seen that there is a drastic improvement in the produced  $H_2O_2$  comparing BPS1-5 to BPS1-5Fe700, further supporting the successful modification of the carbon support and formation of active sites.

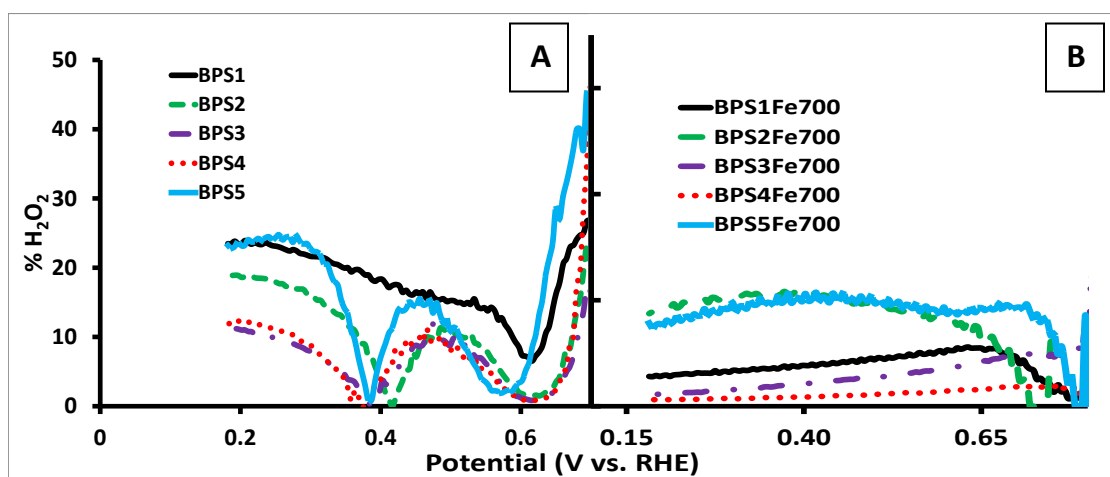


Figure 3.15. Comparison of hydrogen peroxide production for BPS1 - BPS5 (A) to BPS1Fe700 – BPS5Fe700 (B) treatment. Measurements were collected at 900 RPM in an  $O_2$  saturated 0.5M sulphuric acid solution with the ring potential held at 1.2V.

The reduction in  $H_2O_2$  production is an anticipated trend; however analysis of BPS1Fe700 to BPS5Fe700 does not show a trend. BPS4Fe700, with the best onset potential and limiting current, resulted in the lowest  $H_2O_2$  production as expected, but the remaining samples did not have a correlation between their hydrogen peroxide production and onset potential. Figure 3.16 compares the hydrogen peroxide production to the aphen loading for BPS1Fe700 to BPS5Fe700.

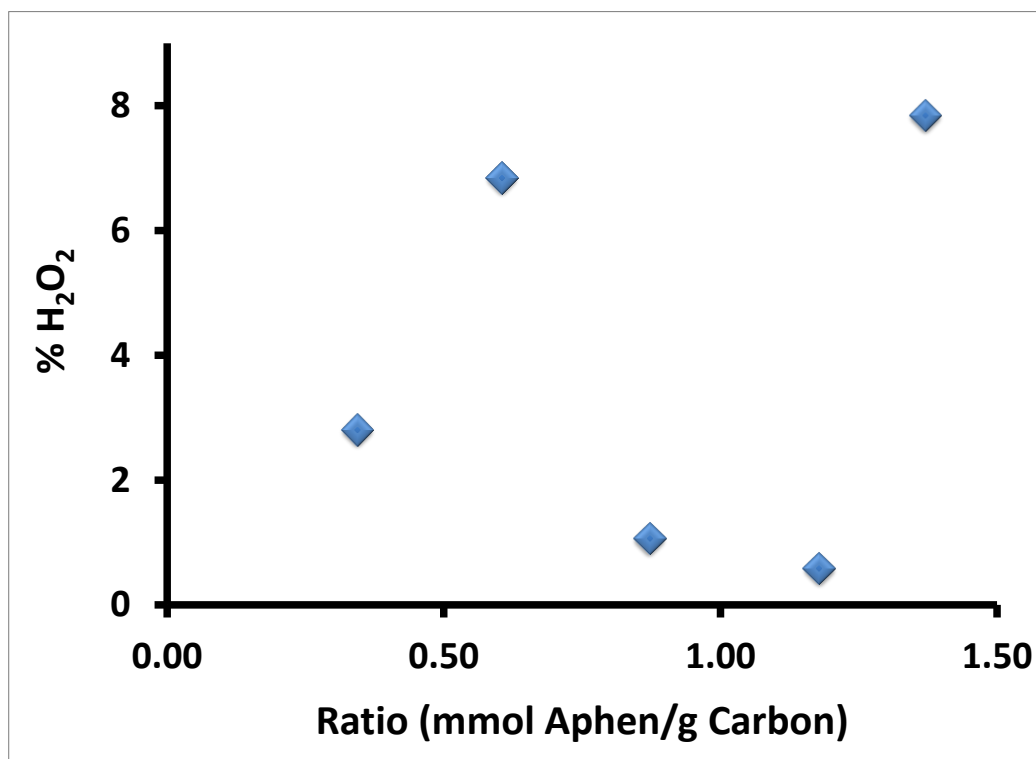


Figure 3.16. Comparison of the hydrogen peroxide production and ratio for BPS1Fe700 to BPS5Fe700.

In order to explore this aspect in more detail Koutecky-Levich analysis was completed on the BPS1-5Fe700 series to determine what ORR pathway was taking place. Figure 3.17 compares the theoretical curves for the two and four electron ORR pathway to the BPS1-5Fe700 series. The results of these calculations indicate that BPS2Fe700 and BPS3Fe700 align with the two electron process and BPS4Fe700 was closer to the four electron process, with some discrepancies in the lower RPM region. These data also correspond to their H<sub>2</sub>O<sub>2</sub> production, with the latter sample having a lower percentage than the former two.

Discrepancies arise with BPS1Fe700 and BPS5Fe700, both lying above the theoretical 2 electron process. This deviation may be a result of alternate redox activity occurring at the electrode as it is possible that both BPS1Fe700 and BPS5Fe700 had a very low number of active sites. This indicates that both these samples may have so few accessible active sites that alternate redox processes are occurring on the carbon surfaces.

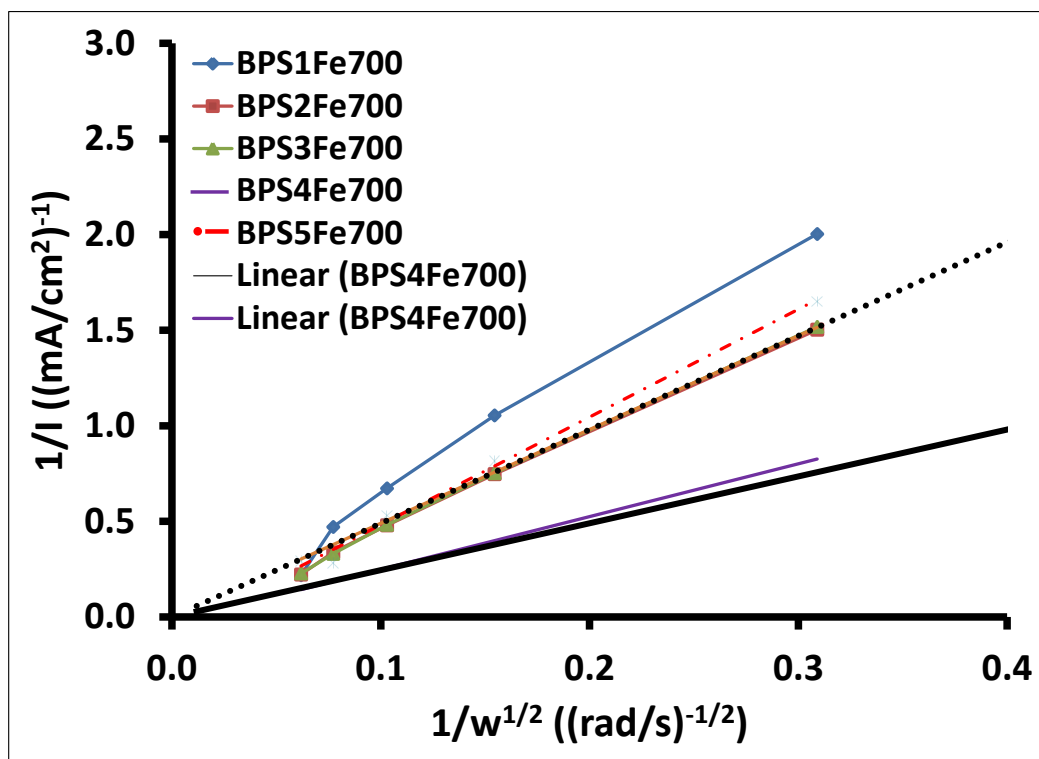


Figure 3.17. Koutecky-Levich analysis for the BP series compared to the theoretical two and four electron processes.

Table 3.1 summarizes key results obtained in the study of BPS1Fe700 to BPS5Fe700. It is evident that BPS4Fe700 outperformed all other materials in the series. This sample yielded the highest onset potential, lowest limiting current, and lowest H<sub>2</sub>O<sub>2</sub> production. How this relates to the other aspects will be discussed later in the section.

Table 3.1. Summary of information regarding the activity for the final catalysts in the BP series.

Sample (Name)	Onset Potential (V vs. RHE)	Limiting Current (mA/cm <sup>2</sup> )	H <sub>2</sub> O <sub>2</sub> Production (%)	Nitrogen Content (%)	Surface Area (m <sup>2</sup> /g)	I <sub>D</sub> /I <sub>G</sub> Ratio
BPS1Fe700	0.61	-1.49	2.81	2.35	1210.9	1.04
BPS2Fe700	0.72	-2.09	6.85	1.97	1069.4	1.01
BPS3Fe700	0.73	-2.08	1.07	2.15	1545.9	N/A
BPS4Fe700	0.78	-5.52	0.59	3.26	1048.3	1.02
BPS5Fe700	0.75	-1.89	7.85	3.75	1775.5	N/A

Comparing the activity of the BP series, it can be seen that overall the onset potentials and limiting currents are relatively close in value. Although differences of 10 mV are significant in terms of onset potential, duplicate measurements were not performed for these materials. It is therefore possible that the differences in activity are not as significant as discussed in these

results as deviations of 2-3 mV may be within experimental error. However it is still clear that at least BPS4Fe700 has the best performance and will be treated as the most active sample for the remainder of the discussion of this series. The low limiting current and hydrogen peroxide data support the conclusion that BPS4Fe700 is the most active catalyst of the series.

Although the onset potential of BPS4Fe700 was good in comparison to the rest of the series, it is still below that of JM20%Pt indicating that there is still need for improvement for these catalyst to displace Pt. The calculated onset potential from the standard material was found to be 0.82 V vs. RHE which is not too far off from the 0.78 V vs. RHE seen for BPS4Fe700. Figure 3.18 compares these two samples and it can be seen that although the onset potential is not as good as JM20%Pt, the limiting current is very good.

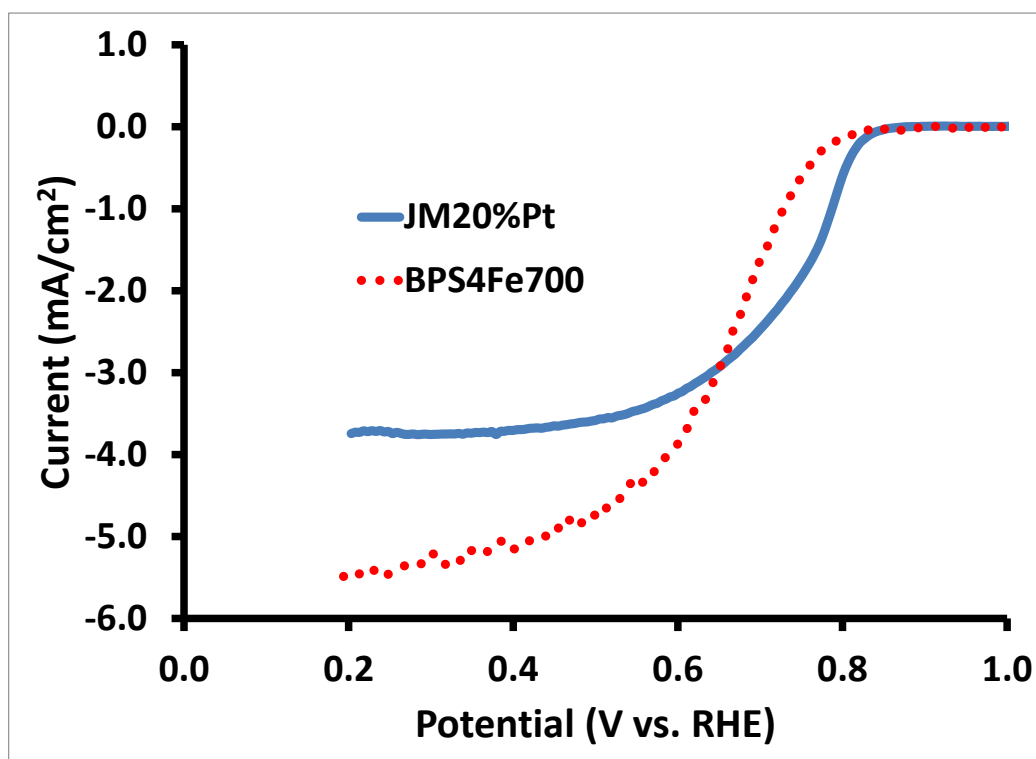


Figure 3.18. Comparison of the activity of BPS4Fe700 to a platinum standard. Measurements were obtained in an O<sub>2</sub> saturated solution of 0.5M sulphuric acid at a rotation rate of 900 rpm.

### 3.3.2 Effects of Modification on Black Pearls Structure

The effects of the catalyst synthesis on the structure of the BPS1-5Fe700 series was investigated by analyzing and comparing the results of BET, XPS, Raman, TEM and TGA experiments. Table 3.2 summarizes the data obtained from BET analysis for BPS1Fe700 to BPS5Fe700. Overall the

pore diameters were roughly the same with varying pore volumes and surface areas. It is also noted that there is an increase in average pore diameter comparing the series to the unmodified BP.

**Table 3.2. Summarized BET data for the BP series with aphen, iron, and after heat treatment.**

Sample	Surface Area (m <sup>2</sup> /g)	Average Pore Diameter Å	Total Pore Volume cm <sup>3</sup> /g
BP	1754.4	15.23	0.933
BPS1Fe700	1210.9	17.00	0.715
BPS2Fe700	1069.4	16.90	0.629
BPS3Fe700	1545.9	16.96	0.959
BPS4Fe700	1048.3	17.00	0.792
BPS5Fe700	1775.5	27.792	1.81

Further investigation into the pore size distribution is represented by the histogram shown in Figure 3.19. Each sample for the BP series is grouped into a range of pore size corresponding to either micropores (less than 20Å) or mesopores (between 20Å and 500Å). A further breakdown of the mesopores section shows the relative amount of pores that may contribute to both pore types (between 22.5Å to 40.5Å). The distribution of pore size is relatively consistent across samples with each sample containing on average 36.3% micropores and 63.7% mesopores with 19% of the pore structures are between 22.5Å to 40.5Å.

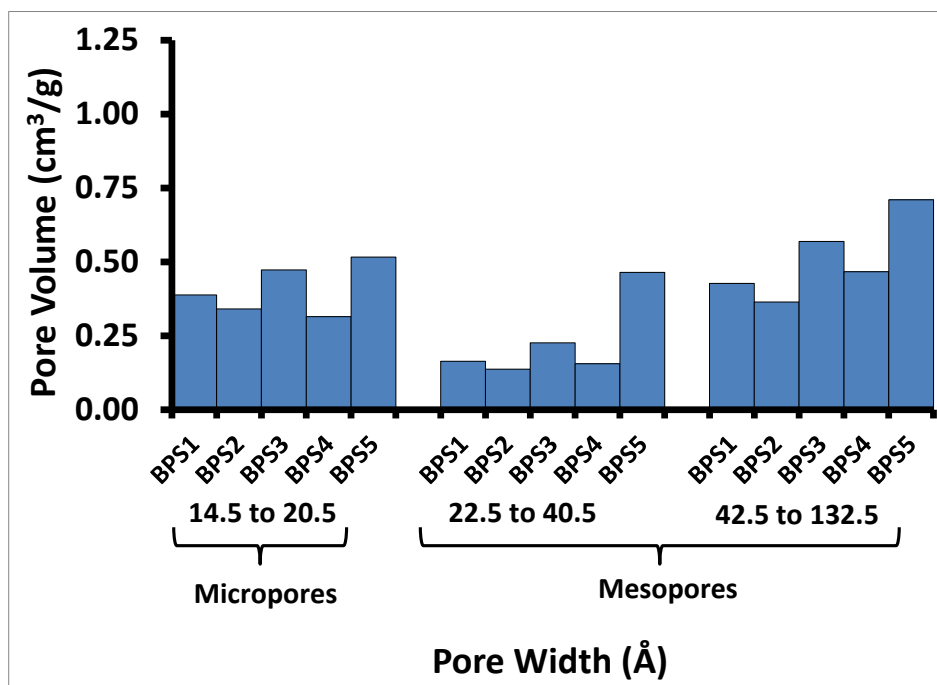


Figure 3.19. Analysis of pore size distribution for the final catalyst of the BP series.

The change in average pore diameter for the series compared to the unmodified BP support indicates that the micropores are likely involved in the active site formation. Comparing the size of apen (9.13Å across) to the pore diameter, and considering two apen molecules are expected to fit across the pore, it is reasonable that a mechanism of rearrangement during heat treatment slightly enlarges the pores to accommodate the active site. The surface area and pore volume for the BP series show a correlation, lower surface area is present with lower pore volumes. Since the pore diameter is remaining consistent, the changes in surface area are likely due either to the amount of pores or the depth of pores in the material. As the samples become graphitized during the heat treatment, the surface area will decrease as pores and other surface defects are reduced. It is also possible that the active sites forming in the pores block access during the BET measurements which will result in artificially low pore volume and surface area measurements.

The best sample of the series displayed the lowest surface area and the second lowest pore volume, indicating that a larger effect from the heat treatment occurred with BPS4Fe700 than the other samples in the series. The lower surface area is likely due to a higher degree of graphitization, which allows formation of the active site, coupled with a higher density of active

sites in the pores. This may also indicate a higher degree of chemisorbed aphen which was not lost upon heat treatment.

Overall there was not a trend in the surface area and pore volume data making it difficult to assess the true effects of the surface structure. The decrease in surface area and pore volume seen in the best sample may also be indicative of the loss of a high amount of nitrogen functionalities resulting in formation of fewer active sites in the samples that perform poorly.

In order to further assess the changes in the structure, Raman spectroscopy was performed with BPS1-5 and BPS1-5Fe700. Figure 3.20 compares the spectra for BPS1-5 (Figure 3.20A) to BPS1-5Fe700 (Figure 3.20B). Each spectra was deconvoluted with contributions from the G band ( $\sim 1590\text{ cm}^{-1}$ ), the D band ( $\sim 1315\text{ cm}^{-1}$ ), the D3 band ( $\sim 1522\text{ cm}^{-1}$ ) and the D4 band ( $\sim 1169\text{ cm}^{-1}$ ). These peaks results from graphitic carbon, disordered carbon, and amorphous carbon contained within a graphitic structure respectively.<sup>69</sup> A sample of the fit for the deconvolution can be seen in Figure 3.21; four Gaussian peaks were found to contribute to the spectra with an  $R^2$  value of 0.99207. All spectra were fitted to at least an  $R^2$  value of 0.99.

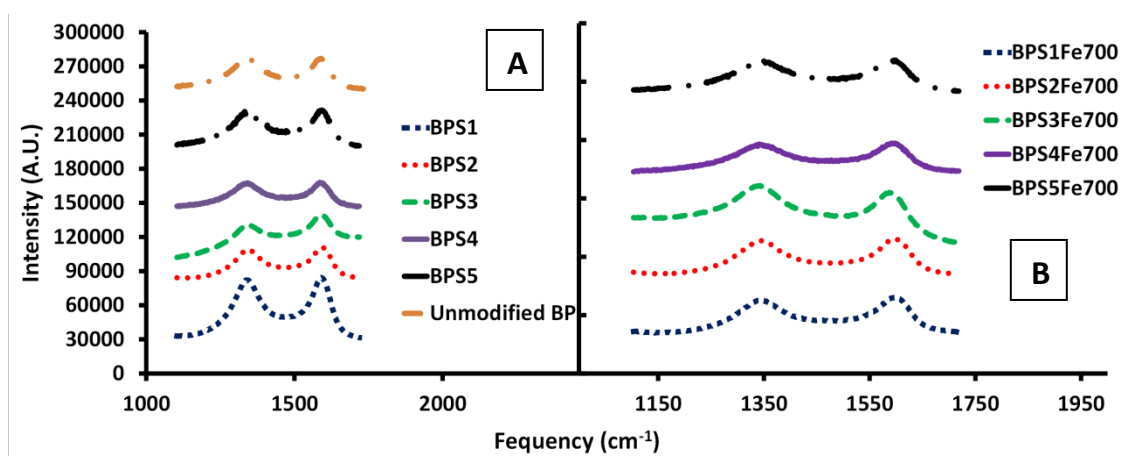


Figure 3.20. Raman data for all catalyst materials from the BP series compared to unmodified BP

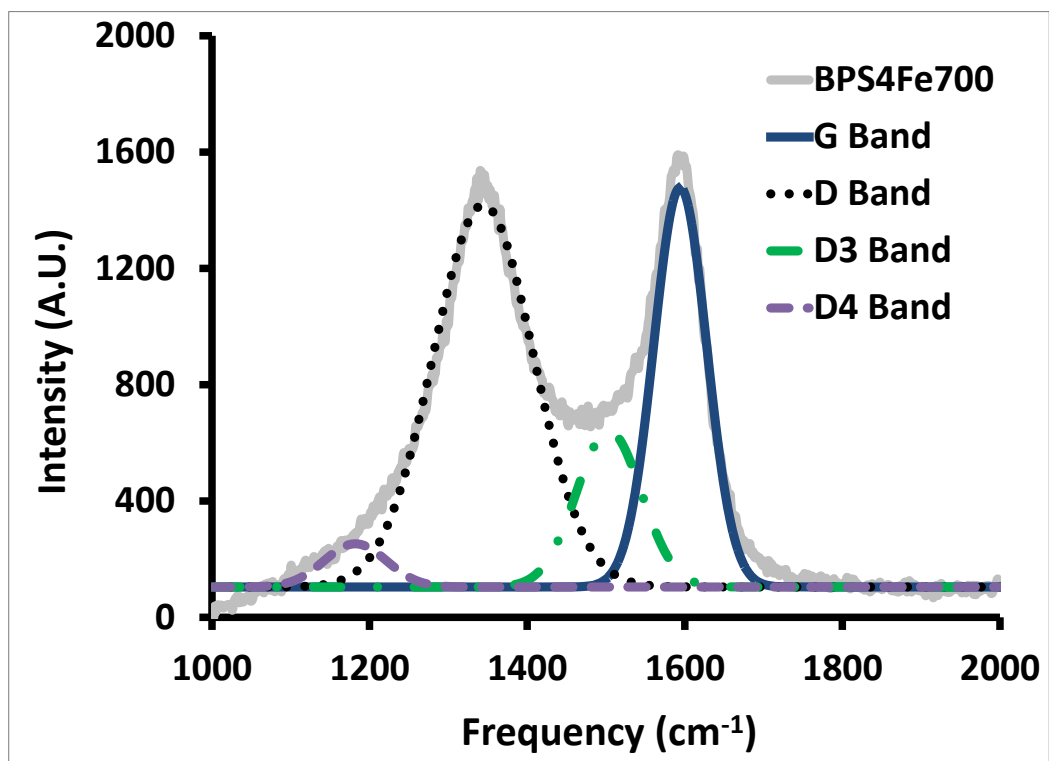


Figure 3.21. Sample of deconvolution fit for the Raman spectra of BPS4Fe700. All spectra were fitted with four peaks to an  $R^2$  value of at least 0.99.

Figure 3.22 directly compares the  $I_G/I_D$  ratios of unmodified BP to all samples in the BP series. It can be seen that the diazonium coupling reaction alone impacts the level of graphitization (comparing BP to BPS1-5). It is possible that the conditions of the reaction allow for a reduction in the amount of amorphous carbon altering the  $I_G/I_D$  ratio. In order to verify the effects of the solvent, exposure of the bare carbon support to the solvent system without the aphe molecule would need to be completed. Alternatively, isolation of the diazonium ion prior to the reaction with the carbon support can be completed to see the effects of the aphe alone. BPS2 indicates a higher level of graphitization pre heat treatment and iron uptake which may be due to errors in the mass of BP or aphe used for this ratio. BPS2 also shows some inconsistency with the rest of the series for other electrochemical and physical characterization and it is likely an error in preparation contributed to this.

Figure 3.22 also shows the change in the level of graphitization as samples move through the synthesis from BPS1-5 to BPS1-5Fe700. One of the largest changes in graphitization occurred with BPS4Fe700 further emphasizing the importance of the rearrangement of the material to form active sites during the heat treatment process. Comparing these results to the BET

measurements, it is likely that the loss of surface area is due to a combination of changes in pore size and structure as well as graphitization. Considering BPS2, there was no change in level of graphitization which supports the argument that loss in surface area is due to pore size and structure changes alone.

Although a large change in the degree of graphitization for BPS1Fe700 was observed as well, it is likely that not enough nitrogen was present to allow for effective formation of active sites. Therefore the importance of the amount of nitrogen in combination with changes in the surface structure and level of graphitization is stressed.

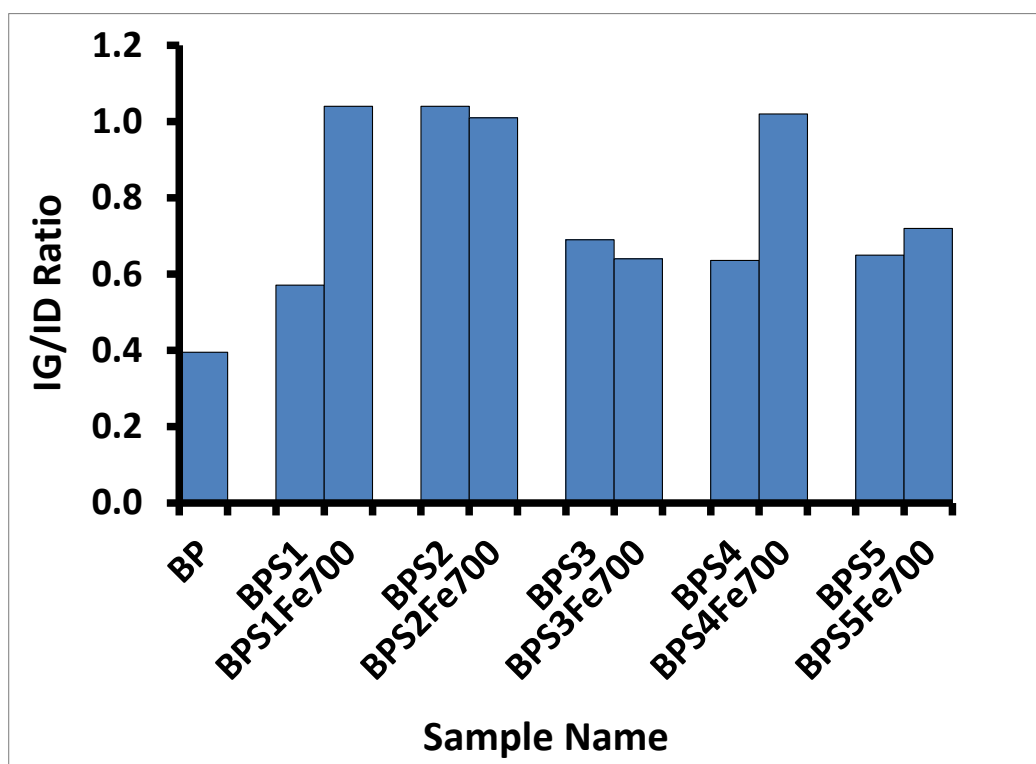


Figure 3.22. Comparison of the IG/ID ratio for each sample in the BP series.

Analysis of the nitrogen content and impact on the catalyst activity was completed by XPS. Figure 3.23 shows the N-1s narrow scan spectra obtained for BPS1-5Fe700 and BPS3. XPS results seen in literature for Fe-C/N materials fit peaks using 3 main contributors; pyridinic, pyrrolic, and graphitic centered around 398 eV, 400 eV, and 402 eV respectively.<sup>70</sup> Considering the only source of nitrogen in this work is a result of the diazonium coupling reaction with aphen, it is likely that only pyridinic nitrogen functionalities would be present in final catalyst materials. Prior to heat treatment it would be expected that 3 nitrogen contributions are possible;

pyridinic and pyridinium (Figure 3.24A) from the pyridinic nitrogen functionalities in aphen, and amine ( $\sim 400$  eV)<sup>71</sup> from unreacted amines on aphen. Upon heat treatment it is expected that the pyridinic functionalities would remain and it is unlikely that these structure would be converted to graphitic or pyrrolic type nitrogen. Other N species that are structurally similar to pyridinic nitrogen have been reported in literature, and have been observed in XPS experiments with peaks centered around 401.2 eV (pyridinium, Figure 3.24A), 400.6 eV (pyridone, Figure 3.24B), or 403.2 eV (pyridine-N-oxide, Figure 3.24C).<sup>72</sup> These structures could easily form from the protonation or partial oxidation of aphen modified carbon materials. Therefore these nitrogen functionalities were considered in place of the pyrrolic and graphitic nitrogen types when performing the XPS deconvolution.

Comparing BPS3 (Figure 3.23F) to the remaining samples in the series clearly illustrates a change in the nitrogen functionalities present. BPS3 contained peaks at 399 eV and 401 eV which we have attributed to pyridinic and protonated pyridinic type nitrogen functionalities respectively. There does not appear to be a peak representing the amine functionality indicating that a monolayer (or multilayer) is present rather than surface adsorption or polyaniline type linkages. BPS1-5Fe700 all display an additional peak at  $\sim 400$  eV which we have attributed to pyridone (Figure 3.24B).

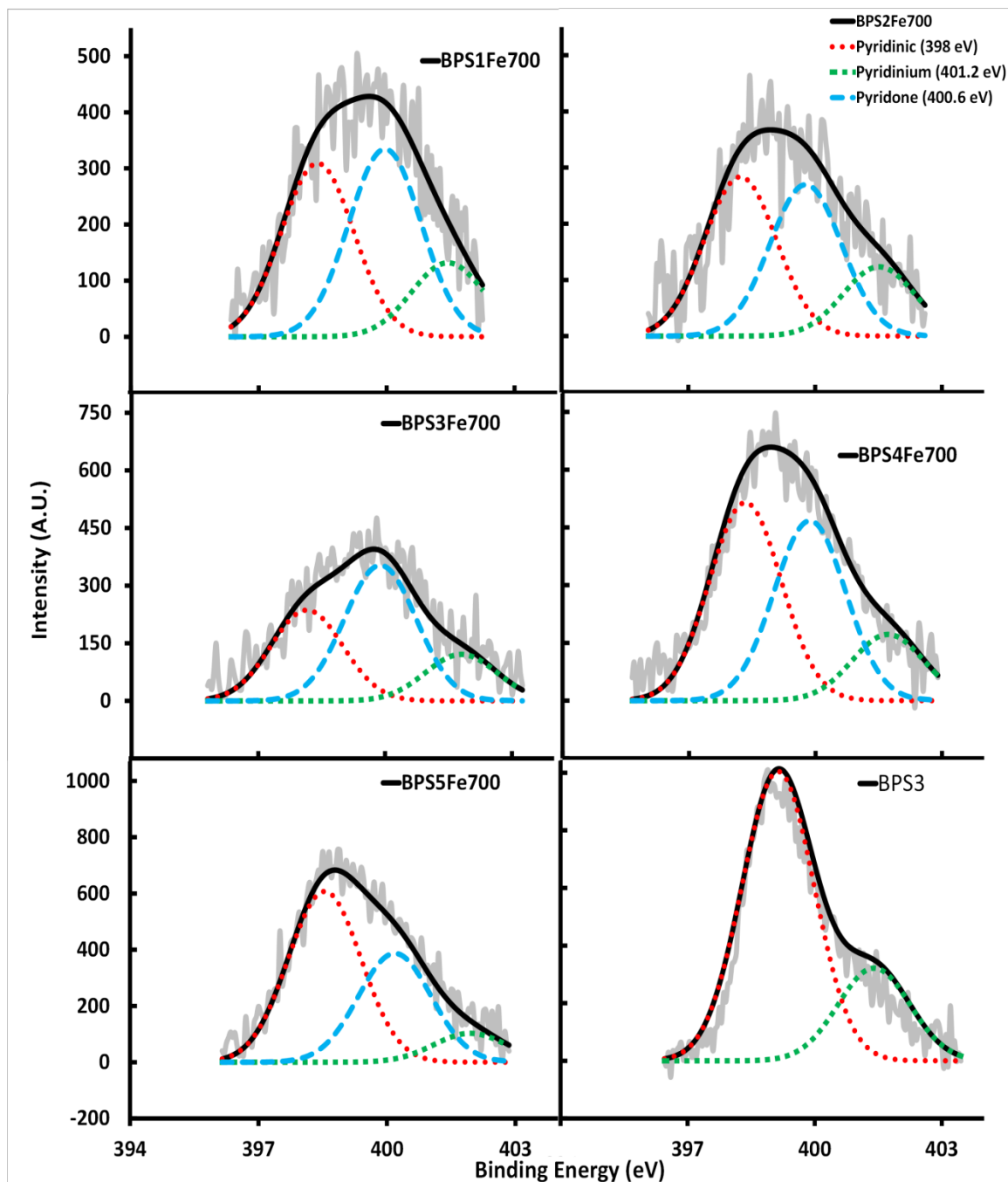


Figure 3.23. N-1s Narrow scan XPS data for final catalysts materials of the BP- series.

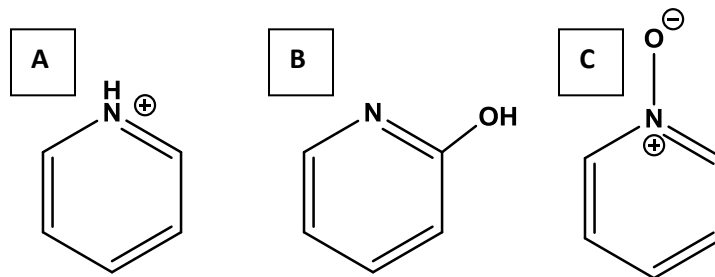


Figure 3.24. Possible nitrogen functionalities present in the catalyst materials; (A) pyridinium, (B) pyridone, and (C) pyridine-N-oxide.

Table 3.3 compares the nitrogen percentage that was added to carbon from the diazonium coupling of the aphen molecule to the amount of nitrogen detected via XPS. For every mole of aphen added, two moles of nitrogen should have been incorporated into the carbon backbone. Accounting for the mass of BP used as well as the additional carbon from the aphen molecule itself, the nitrogen percentage was determined. The onset potential and carbon to nitrogen ratio are also compared to these nitrogen percentages. Comparing the amount of nitrogen added to the amount determined by XPS for each sample, it can be seen that the measured nitrogen content is higher than the amount added. Although there is an added amount of nitrogen from aphen, there is also a loss of nitrogen and carbon due to the heat treatment process as the sample graphitizes affecting the nitrogen percent. There does not appear to be a trend in the amount that the nitrogen percentage increases by when comparing each ratio. This indicates that different levels of aphen attachment as well as graphitization may be occurring with the different ratios. If the aphen modification differs, the iron content would also be different as would the amount of graphitization. In addition to this, the optimal heat treatment may not be ideal for all samples altering the percentage of carbon and nitrogen lost at this step. Since the formation of an active catalyst is dependent on a narrow temperature range, the samples other than BPS4 may not be rearranging to form the correct active site which would impact the activity as well as the nitrogen content. A trend is seen with the onset potential and ratio; the higher the ratio the more active the catalyst with the exception of BPS5Fe700. Reasons for the inconsistency for BPS5Fe700 have been discussed previously and are likely a result of a multilayer formation of the aphen molecule.

**Table 3.3. Comparison of the amount of nitrogen added to black pearls via diazonium coupling of apheh to the measured amount of nitrogen from XPS analysis.**

<b>Sample</b>	<b>Nitrogen Added (Wt%)</b>	<b>Nitrogen Content (Wt%)</b>	<b>C:N Ratio</b>	<b>Onset Potential (V vs. RHE)</b>
BPS1Fe700	0.785	2.35	36.06	0.61
BPS2Fe700	1.33	1.97	44.83	0.72
BPS3Fe700	1.86	2.15	37.41	0.73
BPS4Fe700	2.42	3.26	24.84	0.78
BPS5Fe700	2.75	3.75	21.96	0.75

Overall an increase in added apheh did result in a lower carbon to nitrogen ratio indicating successful increase in the total nitrogen content. This higher nitrogen content is also coupled with a higher activity with the exception of BPS5Fe700. In addition to this the nitrogen content, the activity is likely tied to the heat treatment which has only been optimized for BPS4. In order to fully understand the impact of the nitrogen type on the activity of the catalysts, further studies into the optimal conditions for each ratio are recommended.

In addition to the nitrogen content, the iron content will impact the activity of the materials. TGA was completed for BPS4Fe700 and BPS2Fe700 by combusting samples in air and measuring the change in mass. It was determined that the iron content for BPS4Fe700 was 3.9% while BPS2Fe700 contained 0.93%. Overall BPS4Fe700 outperformed BPS2Fe700 in all areas; therefore it is clear that even small changes in the nitrogen or iron content will affect the overall activity of the materials.

TEM imaging was completed to study the structure and morphology of the BP series. Figure 3.25 shows images of the best samples (BPS4Fe700) at various magnifications (Figure 3.25B-F) compared to as received BP (Figure 3.25A). It can be seen that the carbon materials maintain its amorphous appearance, though you can begin to see some order on the 20 and 10 nm scale.

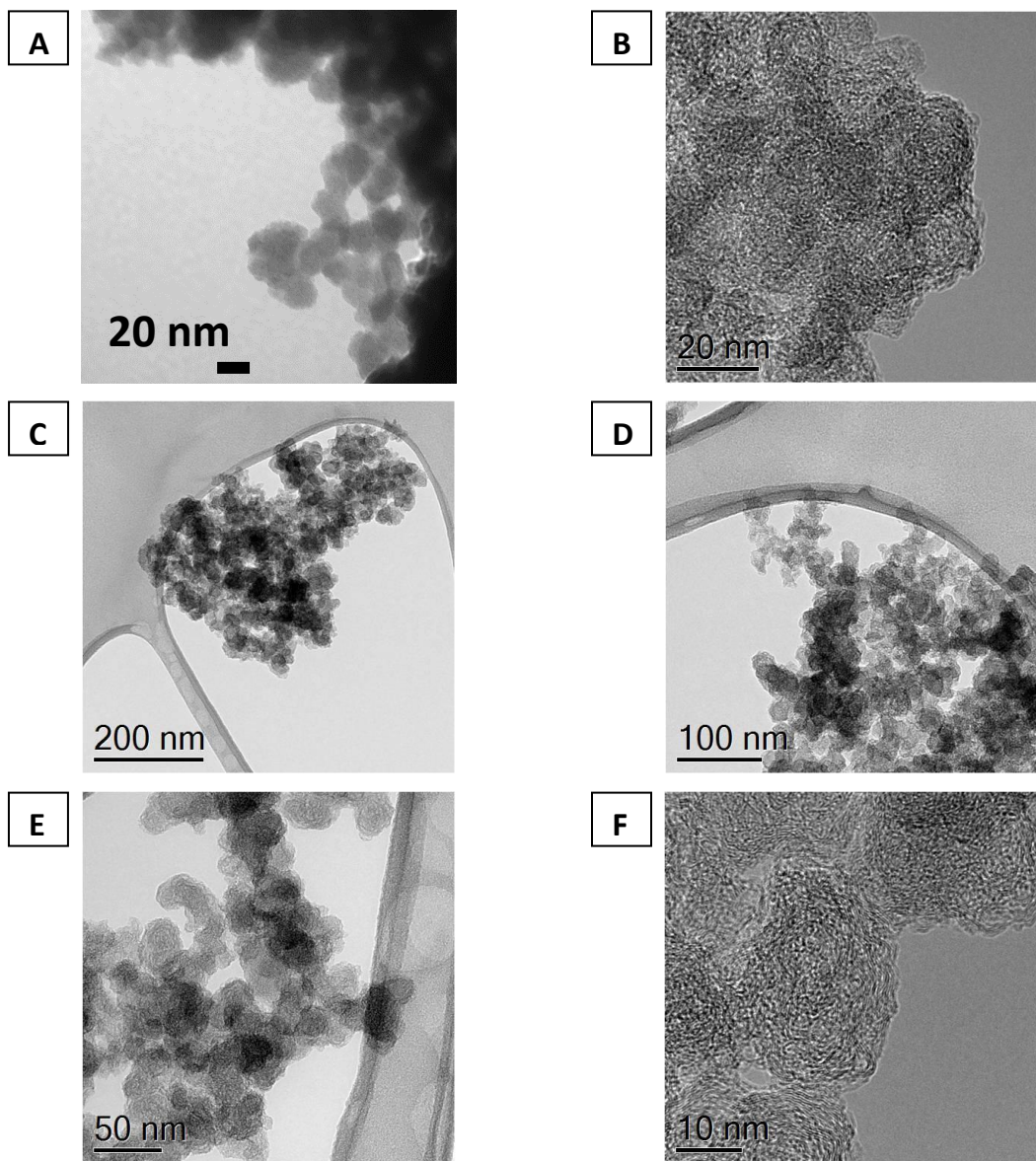


Figure 3.25. TEM images of BPS4Fe700 at 142000X, 250000X, 31500X, 50000X, 80000X, and 400000X magnification for A-F respectively.

### 3.4 Results & Discussion: Ketjen Black Series Catalysts

#### 3.4.1 Impact of Aphen Loading

Analysis of the results obtained for BPS1-BPS4 determined a trend relating the amount of aphen to the overall activity. It was observed that increased aphen loading resulted in increased activity; however there was a decline with the highest loading. In order to determine if difference in carbon structure would affect catalyst performance, another carbon support, KB, was used.

Figure 3.26 shows the CVs obtained for the KB series and clearly displays the changes in peak height with varying aphen loadings. The peaks are due to the redox activity of the nitrogen groups from the attached aphen molecule, therefore the peak heights can be related to the amount of redox active nitrogens present in the samples. There does not appear to be a trend relating the amount of nitrogen present to the aphen loading with the KB samples; KBS4 demonstrates the weakest activity and KBS5 showing the strongest.

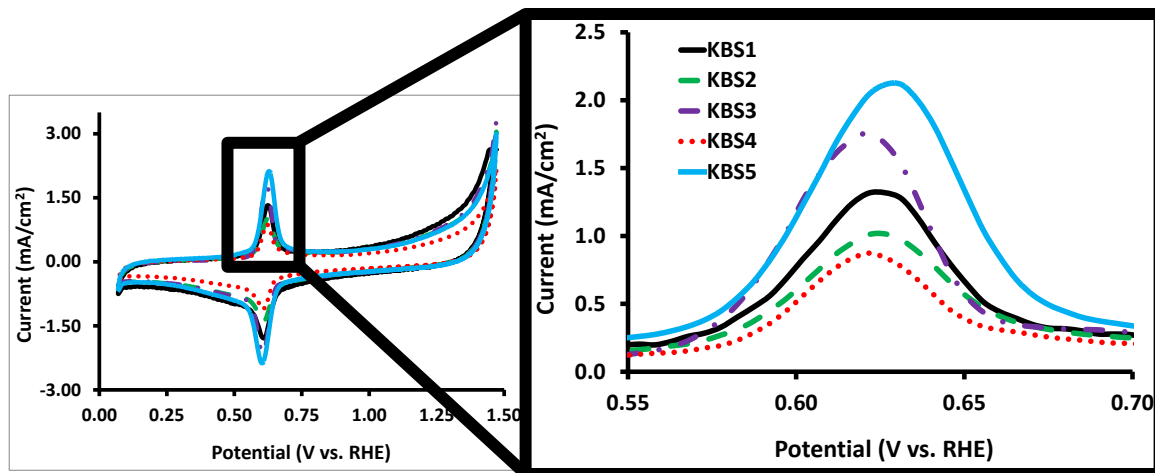


Figure 3.26. Cyclic voltammograms for each prepared ratio of KB and Aphen. Measurements are recorded at a scan rate of 10 mV/s in an  $N_2$  saturated 0.5 M sulphuric acid solution.

In order to clearly see the relationship between these two aspects, the area under the oxidative peak was measured and from this the charge transfer was calculated (Figure 3.26). An oscillation in the transferred charge is observed, which does not seem to correlate to the amount of aphen added. It is possible that the conditions that were optimal for the BP coupling are not ideal for KB. It is likely that, as with BPS5, the aphen is not forming a monolayer which would make it inaccessible and therefore would not show an electrochemical response. It is unclear if this is the case for both KBS2 and KBS4.

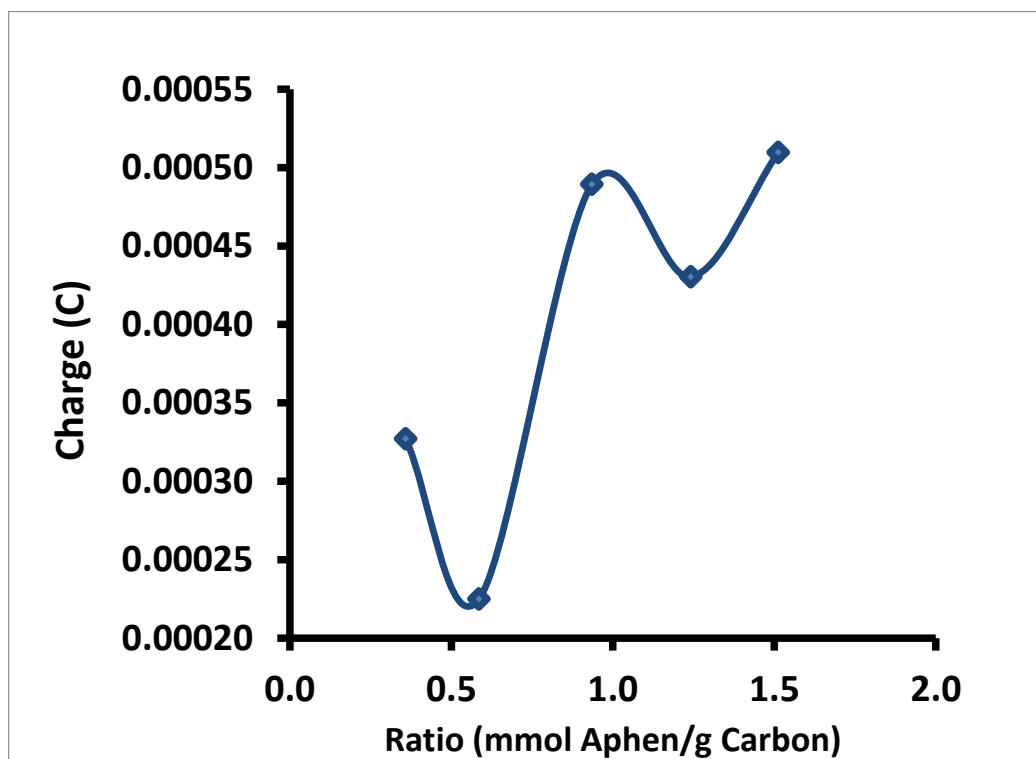


Figure 3.27. Relationship between charge transferred and ratio for KBS1-KBS5.

It can be seen when comparing Figure 3.26 and Figure 3.28 that the iron uptake and subsequent heat treatment did impact the structure of the catalyst. This is indicated by the large reduction in the peaks centered at  $\sim 0.6$  V vs. RHE indicating a change in the aphen or its evolution during heat treatment.

Figure 3.29 illustrates the improvement in activity and efficiency of BPS1 to KBS5 (Figure 3.29A) and KBS1Fe700 to KBS5Fe700 (Figure 3.29B). The best onset potential obtained for this series was 0.70 V vs. RHE for KBS5Fe700 which gave a limiting current of  $-3.02$  mA/cm<sup>2</sup>. The best limiting current for this series was  $-3.23$  mA/cm<sup>2</sup> for KBS3Fe700 which gave an onset potential of 0.68 V vs. RHE.

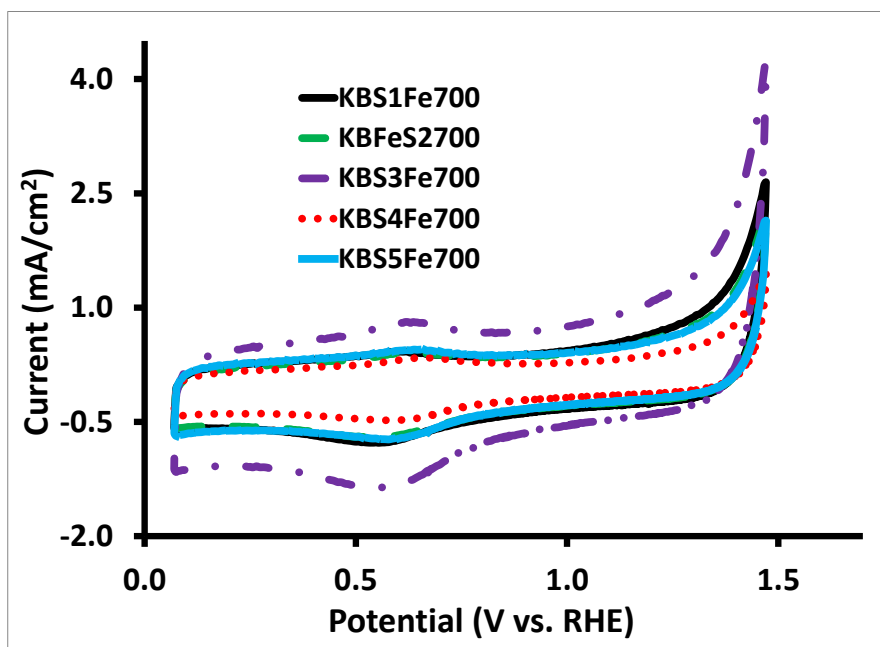


Figure 3.28. Cyclic voltammograms for each prepared ratio of KB with apheh and iron following heat treatment. Measurements were taken at a scan rate of 10 mV/s in an N<sub>2</sub> saturated 0.5 M sulphuric acid solution.

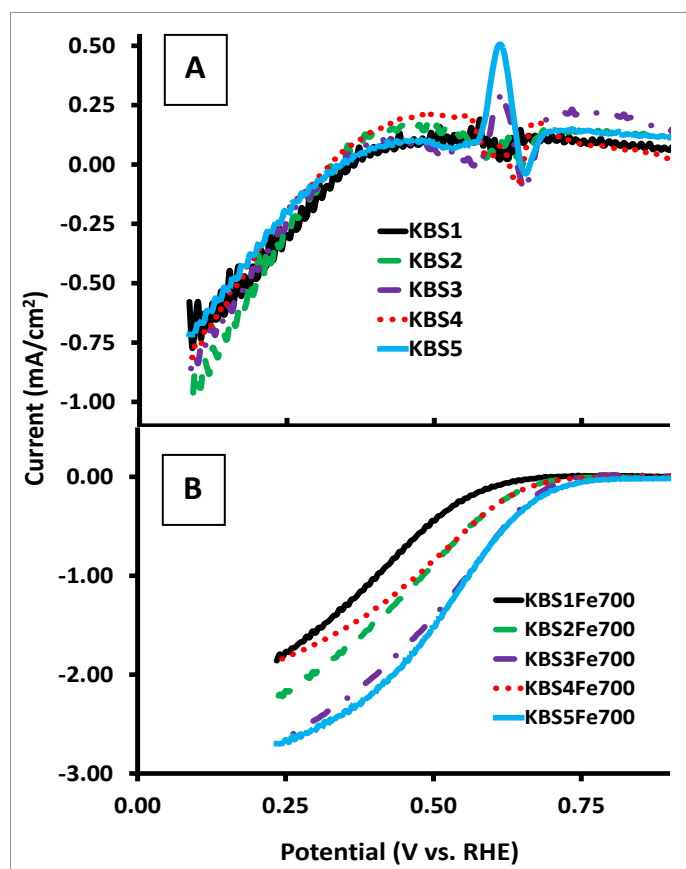


Figure 3.29. Change in ORR activity (A) with apheh alone and (B) with apheh, iron, and post heat treatment. Measurements were performed at 900 RPM in an O<sub>2</sub> saturated 0.5 M sulphuric acid solution at 900 rpm.

Figure 3.30 shows the relationship between the onset potential of KBS1Fe700 to KBS5Fe700 and their respective ratios. The same pattern that was observed for KBS1-5 (Figure 3.30) was not observed for the activity of KBS1Fe700 to KBS5Fe700. The dip in activity for KBS2 is not present for KBS2Fe700 indicating that although the aphen loading did not yield an ideal coverage initially, there was sufficient aphen to coordinate iron and form an active site following the iron uptake and heat treatment steps. This supports the idea that KBS2 had some aphen molecules that were attached by multilayers on the surface rather than a monolayer. Overall a trend is seen with KBS1Fe700, KBS2Fe700, KBS3Fe700 and KBS5Fe700 with higher ratios yielding better onset potentials. This trend is expected as the higher aphen ratio should result in more coordination sites for the iron and therefore more active sites. However KBS4Fe700 has a drop in activity mirroring the drop in transferred charge from KBS4. This indicates that although KBS2 demonstrated the ability to incorporate excess aphen into the support after iron soaking and heat treatment, KBS4 was unable to do so. It is possible that the heat treatment was not ideal for this ratio or that not enough aphen coupled to the carbon surface.

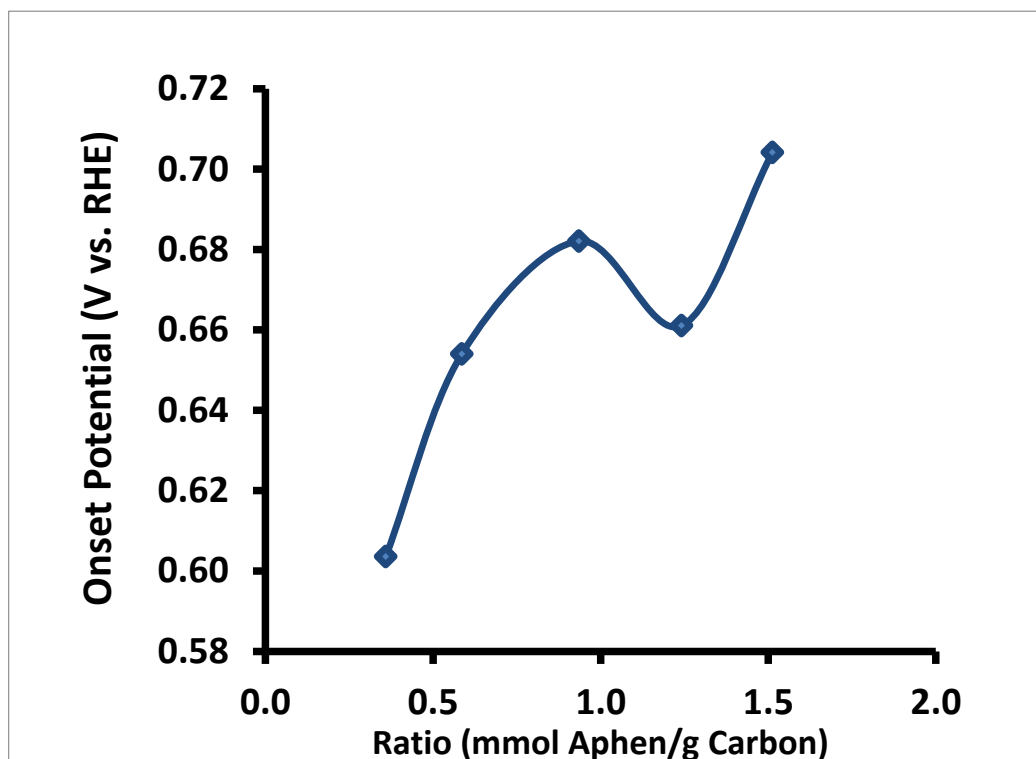


Figure 3.30. Relationship between onset potential and ratio for completed KB series.

Further illustrating the discrepancy with KBS4Fe700, Figure 3.31 shows that this sample also does not have the same correlation between its onset potential and limiting current as the remainder of the series. KBS1Fe700, KBS2Fe700, KBS3Fe700 and KBS5Fe700 show a trend relating higher onset potential to a better limiting current, and although KBS4Fe700 has the worst limiting current of the series, its onset potential is at the midpoint. This discrepancy indicates that something is impacting the ability of the oxygen to get to the active site. This supports the results seen with KBS4 and KBS4Fe700 indicating that there is enough aphen present; however it did not seem to form an active site. It is also possible that variations in the measurements impacted these results as the differences in potentials and currents are very small.

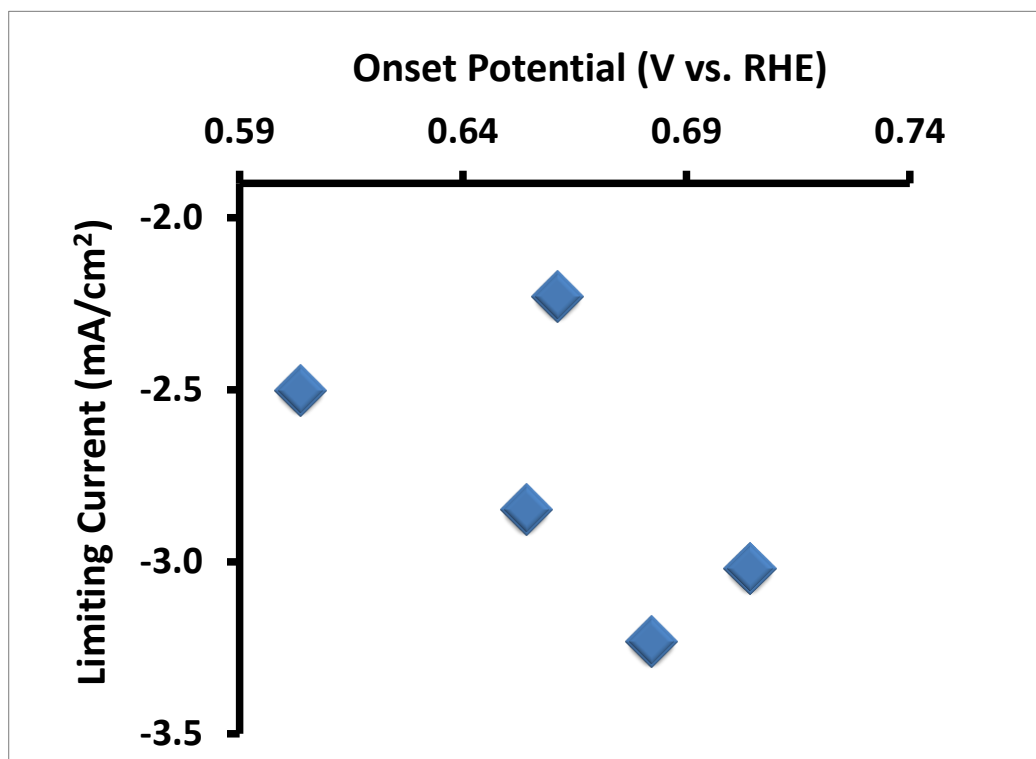


Figure 3.31. Comparison of the limiting current and onset potential for the full BP series.

Overall the diazonium coupling reaction was successful in the modification of the KB support; however a trend was not observed for the performance with respect to the amount of aphen used. It is likely that inconsistencies are due to varying levels of multilayers that are forming on KB and the ability of these multilayers to form active sites upon heat treatment.

Rotating ring disk measurements were obtained and the H<sub>2</sub>O<sub>2</sub> percentage was calculated as stated in section 3.3.1. Figure 3.32 shows the decrease in H<sub>2</sub>O<sub>2</sub> production comparing KBS1-5 (Figure 3.32A) to KBS1-5Fe700 (Figure 3.32B).

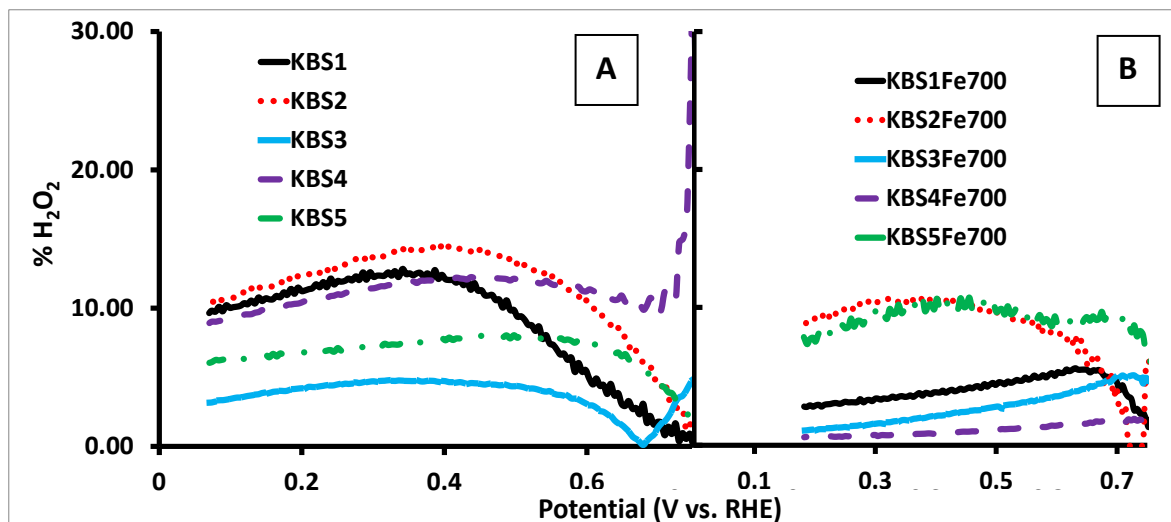


Figure 3.32. Change in hydrogen peroxide production before (A) and after (B) treatment. Measurements were collected at 900 RPM in an O<sub>2</sub> saturated 0.5M sulphuric acid solution with the ring potential held at 1.2V.

The reduction in the hydrogen peroxide production is an anticipated trend; however there does not appear to be a trend relating the aphen loading to hydrogen peroxide production. Figure 3.33 compares the hydrogen peroxide production to the aphen loading for KBS1Fe700 to KBS5Fe700.

In order to explore this aspect in more detail, Koutecky-Levich analysis was completed on the KBS1-5Fe700 set to determine what ORR pathway was taking place. Figure 3.34 compares the theoretical curves for the two and four electron ORR pathway to the KBS1-5Fe700 series. The results of these calculations indicate that for most samples the data appears to sit between the two theoretical curves though slightly closer to the 4 electron process. A trend is seen in with these curves; the lower the H<sub>2</sub>O<sub>2</sub> the closer to the theoretical 4 electron curve the samples are.

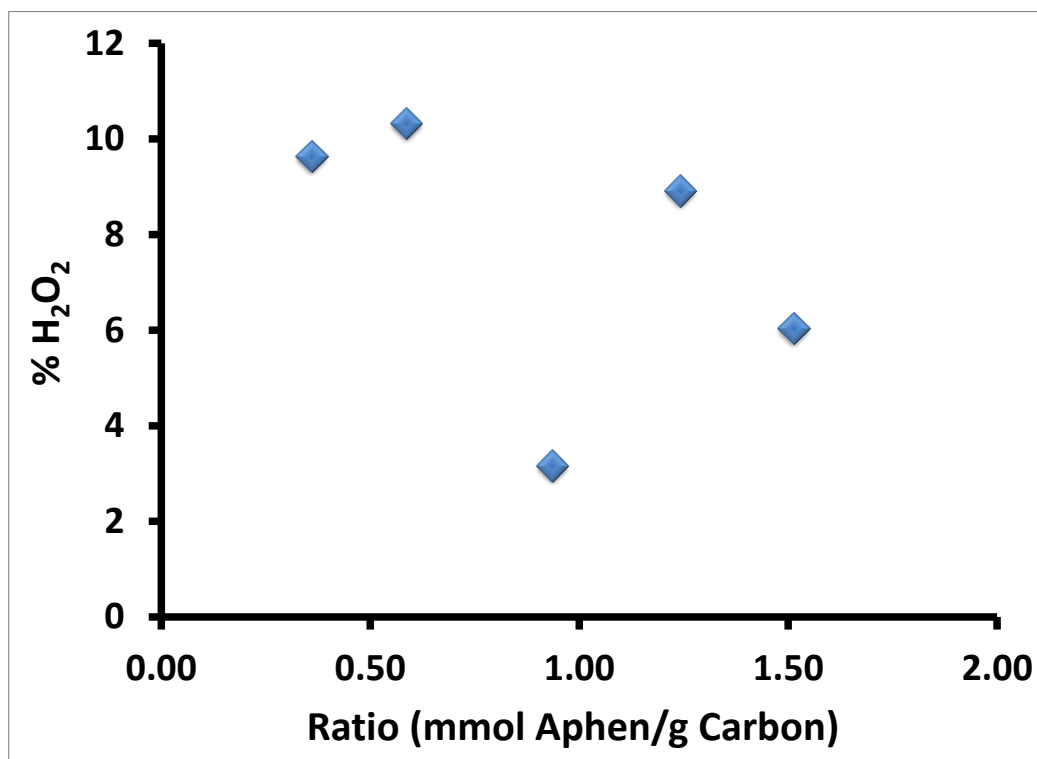


Figure 3.33. Comparison of the hydrogen peroxide production and ratio for KBS1Fe700 to KBS5Fe700

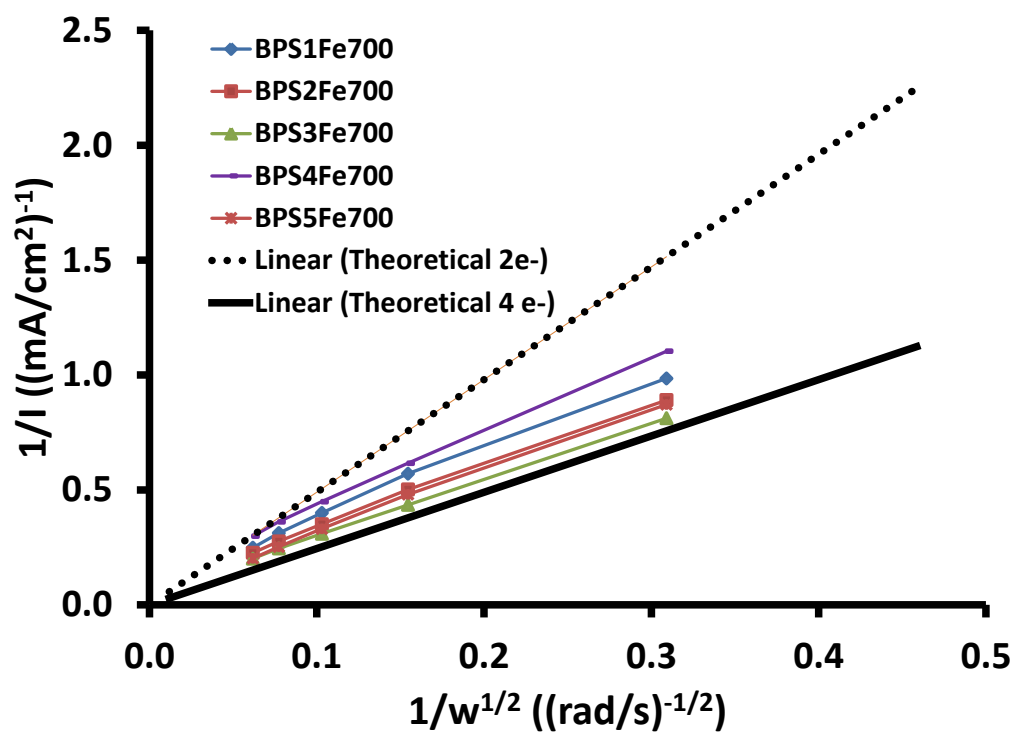


Figure 3.34. Koutecky-Levich analysis for the KB series compared to the two and four electron processes.

Table 3.4 summarizes the key results obtained from the study of KBS1Fe700 to KBS5Fe700. It is evident that KBS3Fe700 and KBS5Fe700 outperformed all other materials in the series.

KBS3Fe700 had the best limiting current, second best onset potential, and lowest hydrogen peroxide production while KBS5Fe700 exceeded KBS3Fe700 only in the onset potential. How this relates to the other aspects will be discussed later in the section.

**Table 3.4. Summary of information regarding the activity for the final catalysts in the KB series.**

<b>Sample (Name)</b>	<b>Onset Potential (V vs. RHE)</b>	<b>Limiting Current (mA/cm<sup>2</sup>)</b>	<b>H<sub>2</sub>O<sub>2</sub> Production (%)</b>	<b>Nitrogen Content (%)</b>	<b>Surface Area (m<sup>2</sup>/g)</b>	<b>ID/IG Ratio</b>
KBS1Fe700	0.60	-2.50	9.64	1.53	1245.5	0.573
KBS2Fe700	0.65	-2.85	10.33	1.74	1023.0	0.283
KBS3Fe700	0.68	-3.23	3.16	1.96	1600.4	0.857
KBS4Fe700	0.66	-2.23	8.92	2.83	868.67	0.563
KBS5Fe700	0.70	-3.02	6.04	4.04	2514.83	0.547

Comparing the activity of the KB series, it can be seen that overall the onset potentials and limiting currents are relatively close in value. Although differences of 10 mV are significant in terms of onset potential, duplicate measurements were not performed for these materials and it is therefore possible that the differences in activity are not as significant as discussed in these results. Although the gap in activity is smaller for this series than the BP, indicating that these differences may be less significant, the catalysts with the highest onset potential were concluded to be the most active and are used for comparison to the best sample of the BP series. Both limiting current and hydrogen peroxide production were the best for the selected samples, supporting their selection as the most active materials of the KB series.

Although these catalyst materials outperform the other samples in the series, their onset potentials and limiting currents are still below that of JM20%Pt indicating that there is still room for improvement. As indicated previously, the calculated onset potential from the standard material was found to be 0.82 V vs. RHE compared to 0.704 V vs. RHE and 0.682 V vs. RHE for samples KBS5Fe700 and KBS3Fe700 respectively. Figure 3.35 compares these two samples with JM20%Pt and it can be seen that both samples are still not reaching the performance of the standard.

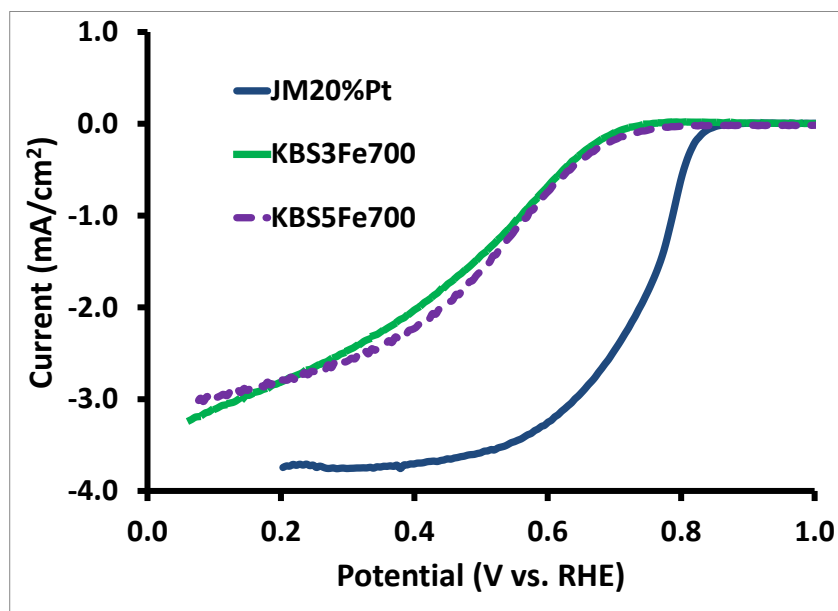


Figure 3.35. Comparison of the activity of KBS3Fe700 and KBS5Fe700 to a platinum standard. Measurements were obtained in an O<sub>2</sub> saturated solution of 0.5M sulphuric acid at a rotation rate of 900 rpm.

### 3.4.2 Effects of Modification on KB Structure

The effects of the synthetic procedure on the structure of the KBS1-5Fe700 series was investigated by analyzing and comparing the results of BET, XPS, Raman, TEM and TGA experiments. Table 3.5 summarizes the data obtained from BET analysis for KBS1Fe700 to KBS5Fe700. Overall the pore size remained relatively constant for all samples with varying surface area and pore volume. Comparing the unmodified KB to the series indicates changes mainly in surface area and pore volume, but not pore size.

Table 3.5. Summarized BET data for the final catalysts of the KB series.

Sample	Surface Area (m <sup>2</sup> /g)	Average Pore Diameter Å	Total Pore Volume cm <sup>3</sup> /g
KB	1492.5	16.96	1.48
KBS1Fe700	1245.5	16.94	1.23
KBS2Fe700	1023.0	16.97	1.05
KBS3Fe700	1027.4	16.93	1.16
KBS4Fe700	868.67	17.00	1.07
KBS5Fe700	1404.5	17.03	1.83

Further analysis into the pore size distribution can be seen in the histogram shown in Figure 3.36. Each sample for the KB series is grouped into a range of pore size corresponding to either micropores (less than 20Å) or mesopores (between 20Å and 500Å). A further breakdown of the

mesopores section shows the relative amount of pores that may contribute to both pore types (between 22.5Å to 40.5Å). The distribution of pore size is relatively consistent across samples with each sample containing on average 14.1% micropores and 85.9% mesopores with 44.4% of the pore structures between 22.5Å to 40.5Å.

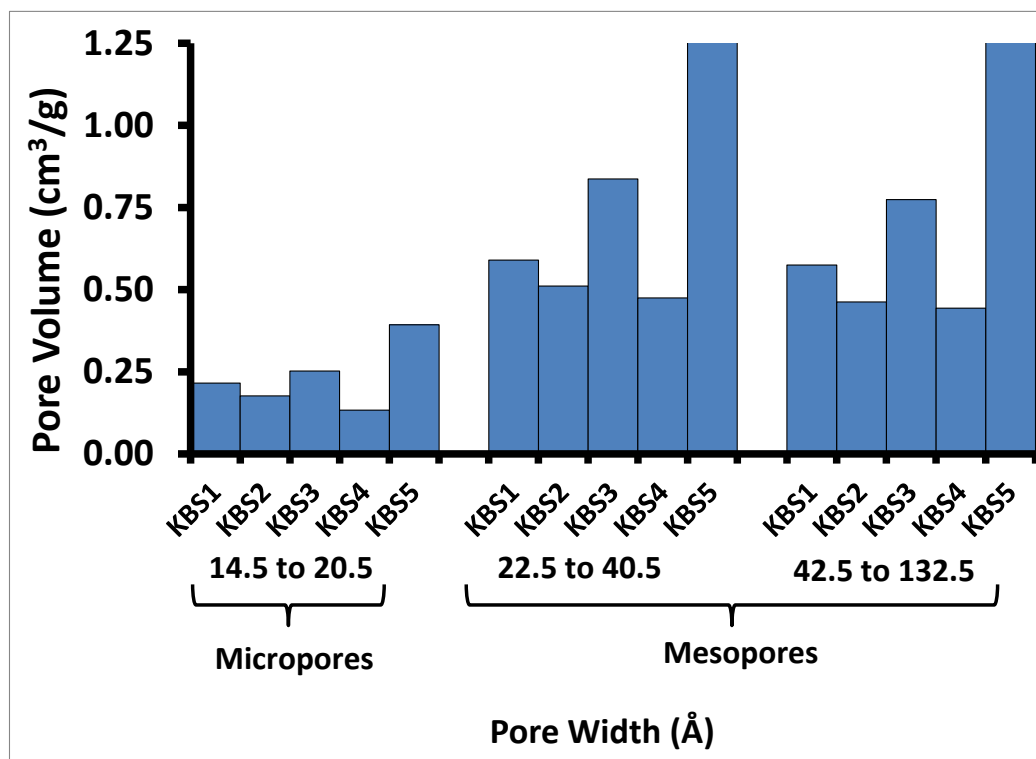


Figure 3.36. Histogram comparing the pore size of the samples prepared with KB after heat treatment and iron soaking.

Variations in surface area and pore volume, with consistent pore diameter, indicate that the extent of graphitization, number of pores and pore depth may be impacted by the different amounts of aphen. As previously discussed, formation of active sites may also block pores resulting in lower surface area and pore volume measurements. Comparing the series to the unmodified KB it is observed that the pore size is consistent with overall decreases in surface area and pore volume only. Since the decrease in surface area, and pore volume, can be attributed to both beneficial and detrimental aspect of the catalyst material, analysis of the BET measurements alone cannot fully assess the relationship between the structure of the catalyst and its activity.

In order to further study the changes in the structure, Raman spectroscopy was performed with KBS1-5 and KBS1-5Fe700. Figure 3.37 compares the spectra for KBS1-5 (Figure 3.38A) to KBS1-5Fe700 (Figure 3.38B). Each spectra was deconvoluted as indicated in section 3.2.2.

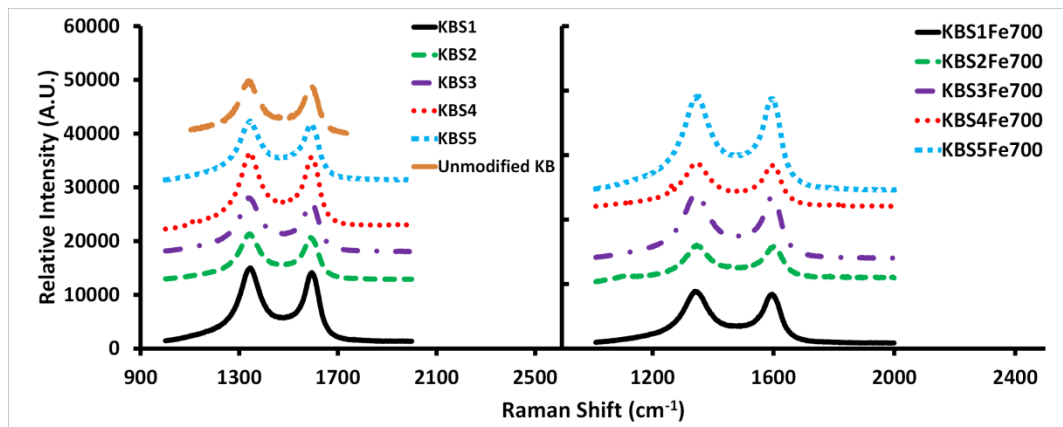


Figure 3.37. Raman data for catalyst materials from the KB series (A) with aphen alone and (B) with aphen, iron, and post heat treatment.

Figure 3.38 compares the  $I_G/I_D$  ratios for all samples in the KB series to the unmodified support. This data indicates that overall there is not much change in the KB structure during the synthesis of the catalyst. It can also be seen that, unlike the BP series, the diazonium coupling reaction did not have a large effect on the overall carbon structure as there is no change in the  $I_G/I_D$  ratio. This indicates that it is likely the solvent effects from the coupling reaction that has removed some amorphous carbon due to its amorphous nature of BP. Since KB is more graphitized, the effects are minimal (and within error) and are not seen with this carbon support. This is likely a result of the level of graphitization inherent to the KB materials. This further supports the argument that changes in surface area seen in the BET measurements are primarily due to changes in the pore structure as the level of graphitization remains relatively consistent between KBS1-5 and KBS1-5Fe700. Although there was no change in graphitization seen within the series, the level of graphitization comparing the ratios may impact the activity. KBS3 and KBS3Fe700 have the highest level of graphitization indicating that this may play an important role in the successful synthesis of the catalyst. However, KBS5 and KBS5Fe700 do not exceed the  $I_G/I_D$  ratio of the remaining materials in the series despite its good performance. This inconsistency further supports the importance of the relationship between the structure and nitrogen content; both aspects need to be optimized in order to synthesize a highly active material.

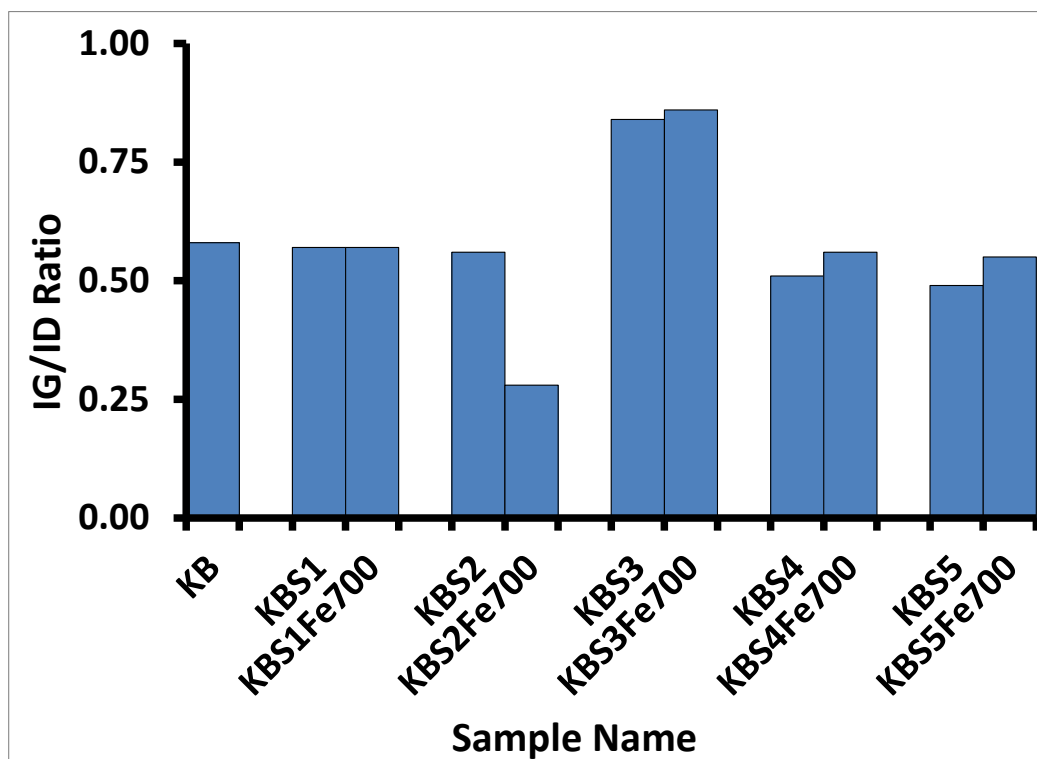


Figure 3.38. Comparison of the  $I_G/I_D$  ratio for each sample in the KB series compared to the unmodified support.

Analysis of the nitrogen content and impact on the catalyst activity was completed by XPS. Figure 3.39 shows the N-1S narrow scan obtained for KBS1-5Fe700. In addition to this, Table 3.6 summarizes the nitrogen content for each sample as well as the ratio between carbon and nitrogen. As with the BP series, it is predicted that nitrogen signals would only arise from different forms of pyridinic type N. Therefore the fits used for the deconvolution of the KB series were centered at 398eV, 400.6eV and 401.2eV corresponding to pyridinic, pyridone, and pyridinium.

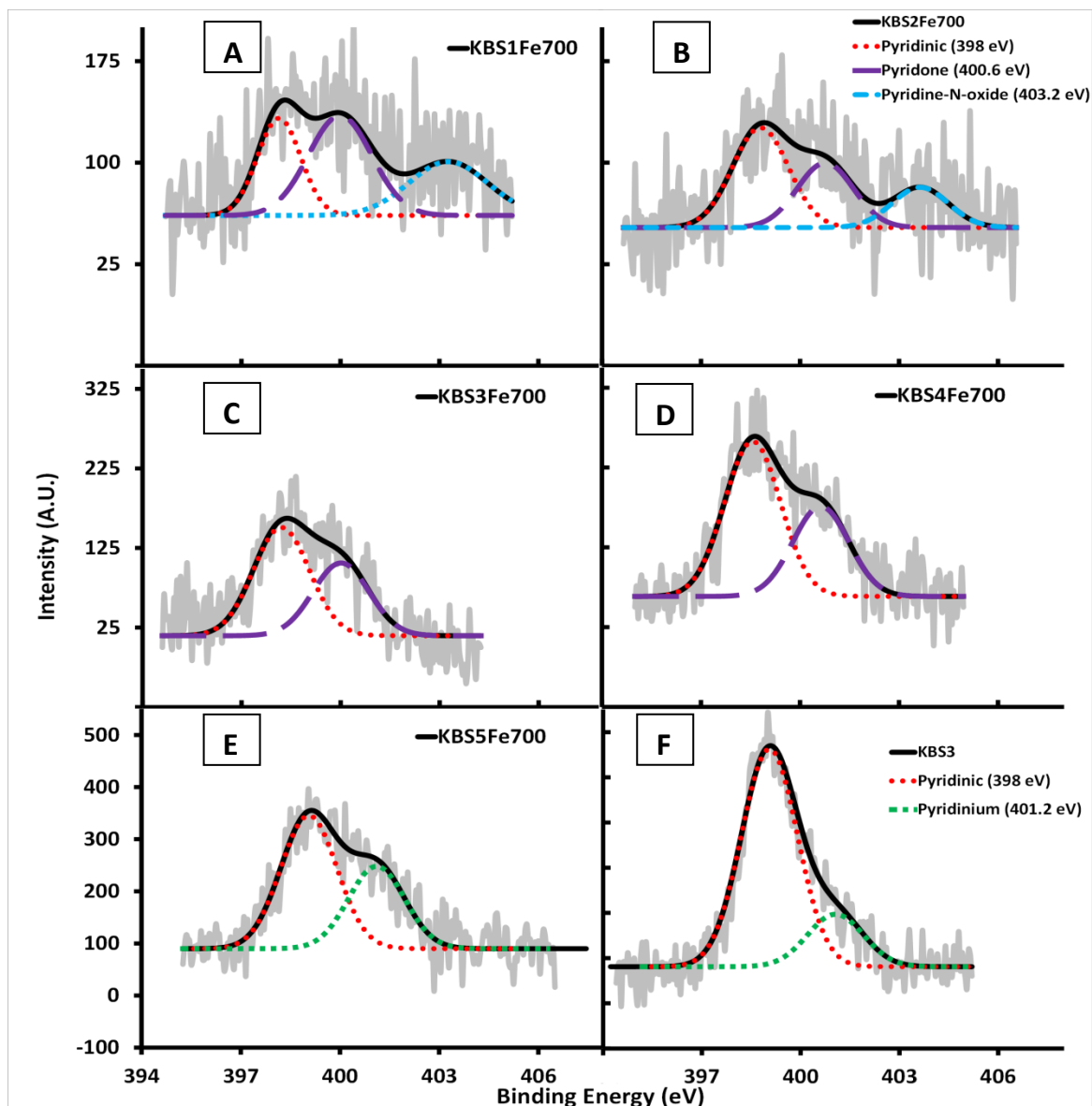


Figure 3.39. N-1s Narrow scan XPS data for final catalyst materials of the KB series.

Analysis of KBS3 indicates two main contributions; pyridinic and pyridinium which were also seen in BPS3. Upon heat treatment KBS5Fe700 retains the same functionalities as KBS3 likely due to the excess of apen that was added to the support. KBS1-4Fe700 lose the contribution from pyridinium and gained pyridone and pyridine-N-oxide which differs from the results seen in BP. This indicates that there is more oxidation of the apen molecule during the synthesis. It may be the incorporation of this additional pyridine-N-oxide functionality that inhibit correct iron coordination and result in lower activity for the KB series.

Examination of the carbon to nitrogen ratio shows a trend; there is a higher amount of carbon compared to nitrogen in KBS1Fe700 with this ratio decreasing as the aphen amounts increases. In addition to this, Table 3.6 compares the amount of nitrogen added via the diazonium coupling reaction to the amount of nitrogen detected by XPS. It can be seen that the amount added and the amount detected do change but no pattern is detected with some samples exceeding the predicted percentage of nitrogen and others falling below it. For most samples there is not a large deviation in expected nitrogen content and amount detected, indicating a less of an impact from graphitization. This agrees with the Raman results which indicate little graphitization occurred during the heat treatment process likely due to the higher level of graphitization in the starting KB material.

**Table 3.6. Summary of XPS data for each final catalyst in the ketjen black series.**

<b>Sample (#)</b>	<b>C:N Ratio (#)</b>	<b>Nitrogen (%)</b>	<b>Added Nitrogen (%)</b>	<b>Onset Potential (V vs. RHE)</b>
KBS1Fe700	57.6	1.53	1.00	0.60
KBS2Fe700	48.4	1.74	1.64	0.65
KBS3Fe700	43.5	1.96	2.6	0.68
KBS4Fe700	30.0	2.83	3.48	0.66
KBS5Fe700	21.3	4.04	4.24	0.70

Overall a trend is seen when comparing the onset potential and ratio of aphen to carbon; the more aphen added, the more active the catalyst. KBS4Fe700 does not follow the trend with a small deviation in the onset potential; however this may be due to differences in onset potential determination or ink preparation.

In addition to the nitrogen content, the iron content will impact the activity of the materials. TGA was completed for KBS3Fe700 and KBS5Fe700 resulting in final iron contents of 2.51% and 10.4% respectively. The difference in iron content can be linked to that nitrogen content seen in Table 3.6.

TEM imaging was completed to analyze the surface of the KB series. Figure 3.40 shows images of one of the best samples (KBS3Fe700) at various magnifications (Figure 3.40. B-F) compared to standard KB without any treatment (Figure 3.40. A). It can be seen that the carbon materials maintains its amorphous appearance, though you can begin to see some order on the 10 nm scale.

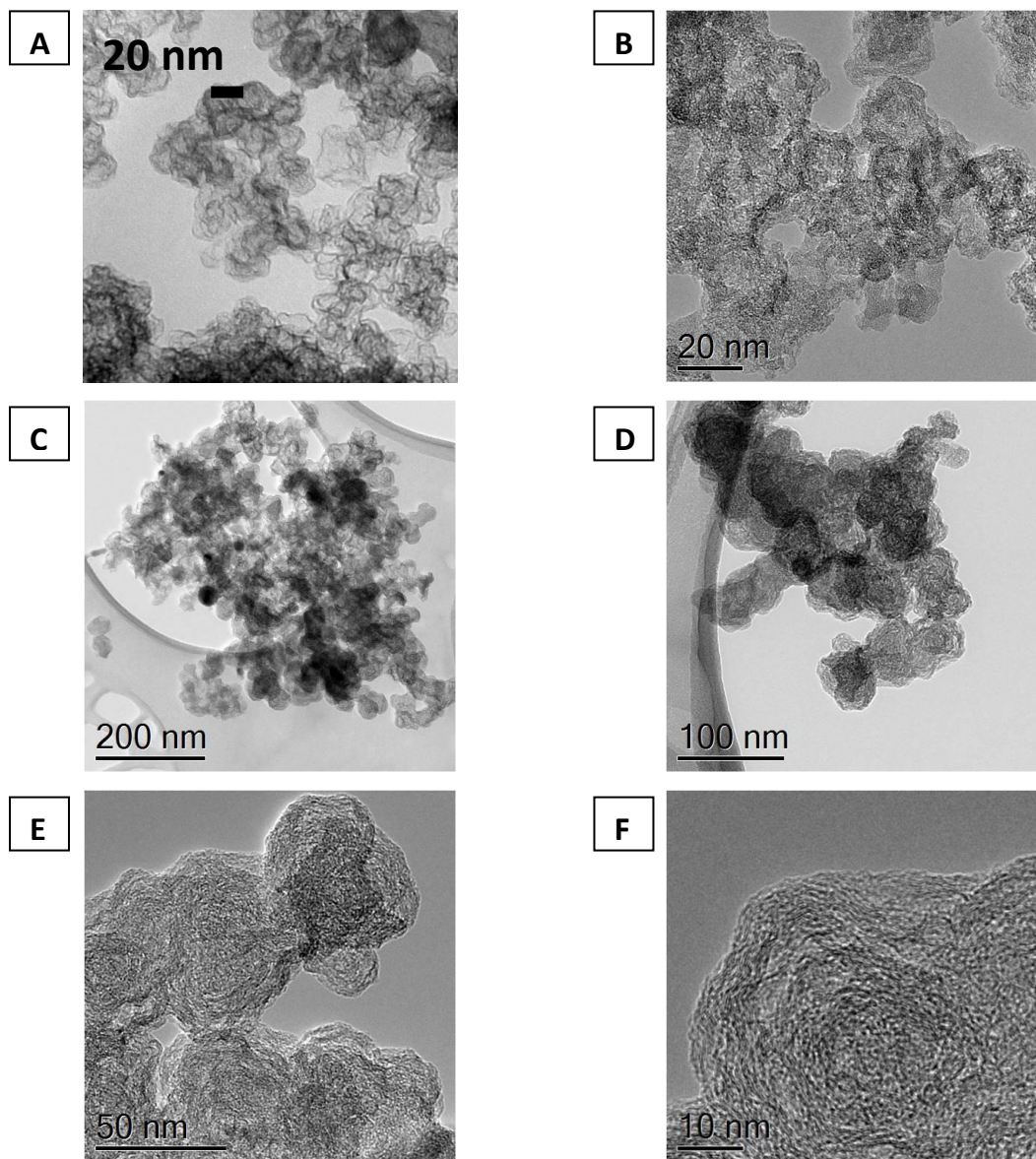


Figure 3.40. TEM images of KBS4Fe700 at 142000X, 200000X, 31500X, 63000X, 160000X, and 400000X magnification for A-F respectively.

### 3.4 Comparison of Base Carbon

A series of 5 varying ratios of aphe to carbon was completed for both BP and KB. Each series was synthesized the same way and underwent identical heat treatments to produce the final catalyst materials; however there were clear differences in the ORR activity. This section will discuss these differences and offer explanations for the trends observed. Figure 3.41 shows the oxidative peak for the aphe redox couple of the best samples of each series after the diazonium coupling reaction. The charge transferred for BPS4 exceeds that for both KBS3 and

KBS5 indicating a higher amount of apen was loaded onto the carbon support. This would be expected when comparing KBS3 and BPS4; however it is unexpected that the higher ratio (KBS5) would still result in a lower loading of apen. Integration of these peaks shows that KBS3 has 66% of the redox active apen as BPS4 and KBS5 has 87%.

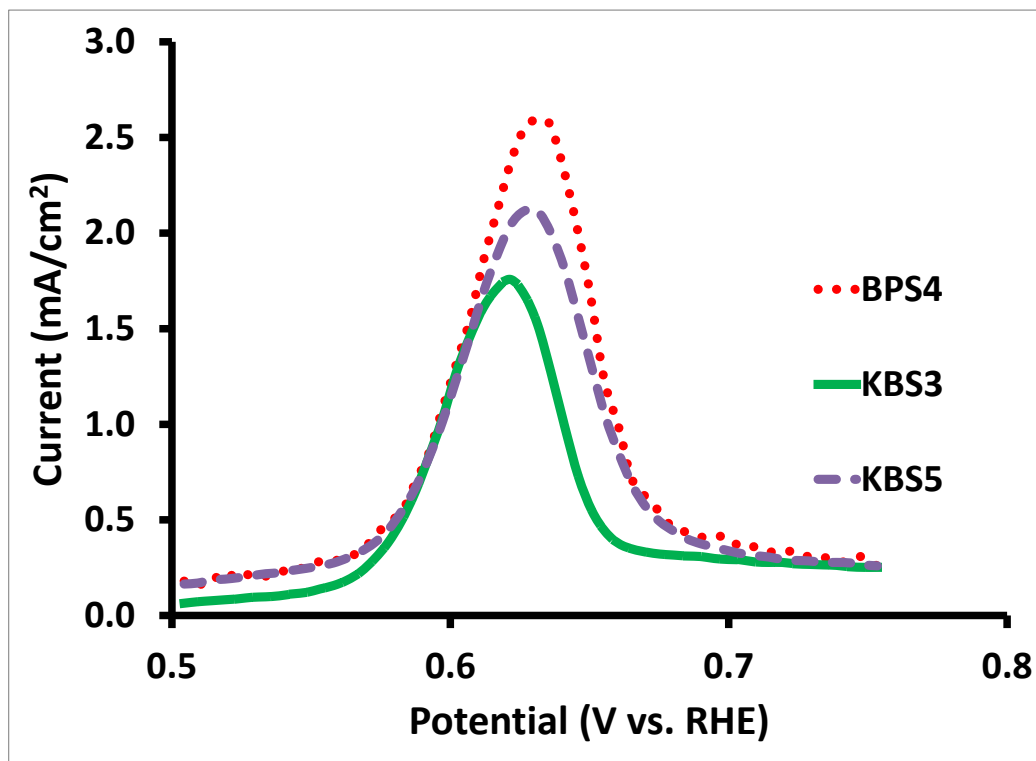


Figure 3.41. Comparison of the oxidative peak for the apen redox couple for the best catalysts of the BP and KB series. Measurements were obtained at a scan rate of 10 mV/s in an N<sub>2</sub> saturated 0.5 M sulphuric acid solutions.

Figure 3.42 compares the amount of apen loaded to the electrochemically active apen calculated from the oxidative peaks. On average 10.6% of the apen used in the diazonium coupling reaction with BP resulted in an electrochemical response upon running the CV's where only 2.95% of the apen used with KB was active. Both carbon supports had low apen coverage as it has been shown it is possible to have ~ 25% coverage when the reaction is completed electrochemically with various azo compounds.<sup>64</sup> It is expected that the active sites are forming in the micropores and mesopores on the carbon support which may be a challenge considering the large size of the apen molecule. The orientation of the apen molecule as well as surface groups on the carbon support will also affect the apen coverage. It has been observed that treating Vulcan XC-72R with a nitric acid solution prior to introduction of iron or nitrogen helped

to increase the overall ORR activity by increasing surface quinone species.<sup>73</sup> Since KB is more graphitized than BP it will also have fewer surface functionalities which may negatively impact the functionalization of the carbon surface. It is possible that more parameters can be optimized to increase the effectiveness of the diazonium coupling reaction for both BP and KB.

The lower percentage of active nitrogen seen with KB indicates that the diazonium coupling reaction was not as effective in modifying this carbon support. The medium for the diazonium coupling reaction was deionized water which would be a challenge for the more hydrophobic KB. This coupled with the expected reactions at the micropores and mesopores decreases the chance of a successful reaction on the KB support. Pre-treating the material to allow for the formation of more surface functional groups and an increased wettability would help ensure better coverage of the carbon surface.

The percentages listed in Figure 3.42 gives a general idea of the amount of aphen that was loaded but will not be indicative of the amounts of active sites due to the incorporation of electrochemically inactive aphen into active sites and the loss of some of these functionalities during the heat treatment. The KB sample with the best onset potential (KBS5) had 21% of the electrochemically active aphen of the best BP sample (BPS4) indicating a significantly higher amount of active aphen present on the carbon support.

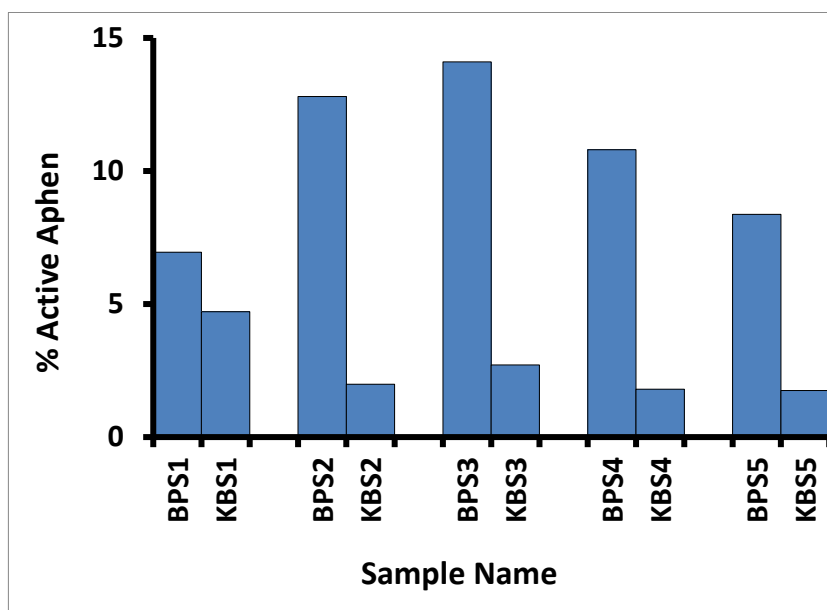


Figure 3.42. Comparison of the amount of active aphen present in BPS1-5 and KBS1-5.

Figure 3.43 compares the activity of the best catalysts of each series following iron soaking and heat treatment. The catalysts maintain the same trend with BPS4Fe700 outperforming KBS3Fe700 and KBS5Fe700; however KBS5Fe700 has 90.64% of the onset potential of BPS4Fe700 and 54.68% of the limiting current. The poor limiting current indicates a lower number of active sites, however the onset potential indicates that although the amount of active sites was significantly less for KB, the active sites that were formed are able to catalyze the ORR at a comparable potential.

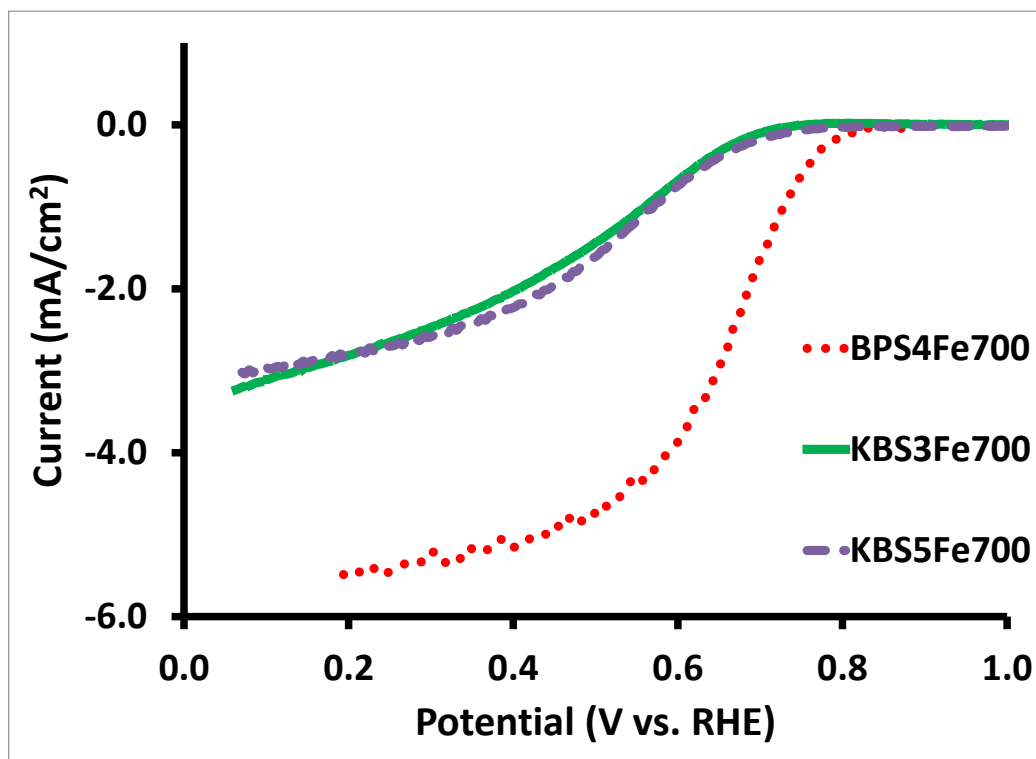


Figure 3.43. Comparison of the activity for the best samples of each series. Measurements were obtained at a rotation rate of 900 rpm in an  $O_2$  saturated 0.5 M sulphuric acid solution.

The onset potentials for the remaining samples in the two series follow the same trend, the BP sample outperform the respective KB ratios. The limiting currents, on the other hand were better for the KB series with the exception of BPS4Fe700. This indicates that there were a larger percentage of good active sites formed on KB than BP compared to the amount of aphen detected after the diazonium coupling reaction. Overall the most active catalyst was still from the BP series which may be due to a variety of factors discussed in this chapter.

Variations in activity between the BP and KB series may be a result of differences in structure both pre and post modification. Table 3.7 summarizes the key structural differences between the samples. The surface area decreases as expected for BPS4Fe700 due to graphitization from the heat treatment. The pore size increases while the pore volume decreases indicating fewer, larger and/or shallower pores are present. Both KBS3Fe700 and KBS5Fe700 also show a decrease in surface area coupled with little change in pore volume and pore size. The Raman results (Figure 3.38) indicated that very little graphitization occurred during the heat treatment since no significant changes in the  $I_G/I_D$  ratio were seen across all KB samples. This observation can be explained by the graphitic nature KB and indicates less transformation is occurring with the KB samples than the BP. The decrease in surface area, but lack of change in pore structure, is likely due to blockages of pores for the formation of active site or other species.

**Table 3.7. Summary of structural information for the best catalysts of each series.**

Characteristic /Sample	BP	BPS4Fe700	KB	KBS3Fe700	KBS5Fe700
Surface Area	1754.7	1048.3	1492.464	1027.4	1404.5
Pore Width	15.2	17.0	17.0	16.9	17.0
Pore Volume	0.933	0.792	1.48	1.16	1.83

Since the mechanism of the formation of the active site is predicted to occur via the slit pore method as proposed by Dodelet et al<sup>31</sup> (Figure 1.4), a more detailed analysis of the pore structure is needed. It may be possible that aphen is able to bond at a pore site to form an active site within the pores on these carbon supports. Figure 3.44 A compares the micropore size between BPS4Fe700 (Figure 3.44A) and KBS3Fe700 (Figure 3.44B). Both histograms are representative of the remaining samples in their respective series, which may offer an explanation for the varied activities in the catalysts. The pore structure of the bare carbon supports can be seen in Figure 3.44B. BP and KB appear to have substantially different pore structures. Prior to any reaction or treatment, BP has a large amount of micropores and few mesopores. KB on the other hand has an even distribution of pore types. Post reaction and treatment causes a reduction in the overall volumes of the pores and a reduction in the number of micropores. BP have a relatively even distribution of micropores and mesopores and a decent separation between these two types. KB has about the same volume in micropores as BP, but a much larger volume in mesopores with a large amount of these mesopores almost overlapping with the micropore range. This would indicate that the micropores present in BP contribute to the formation of a more active catalyst than the mesopores in KB.

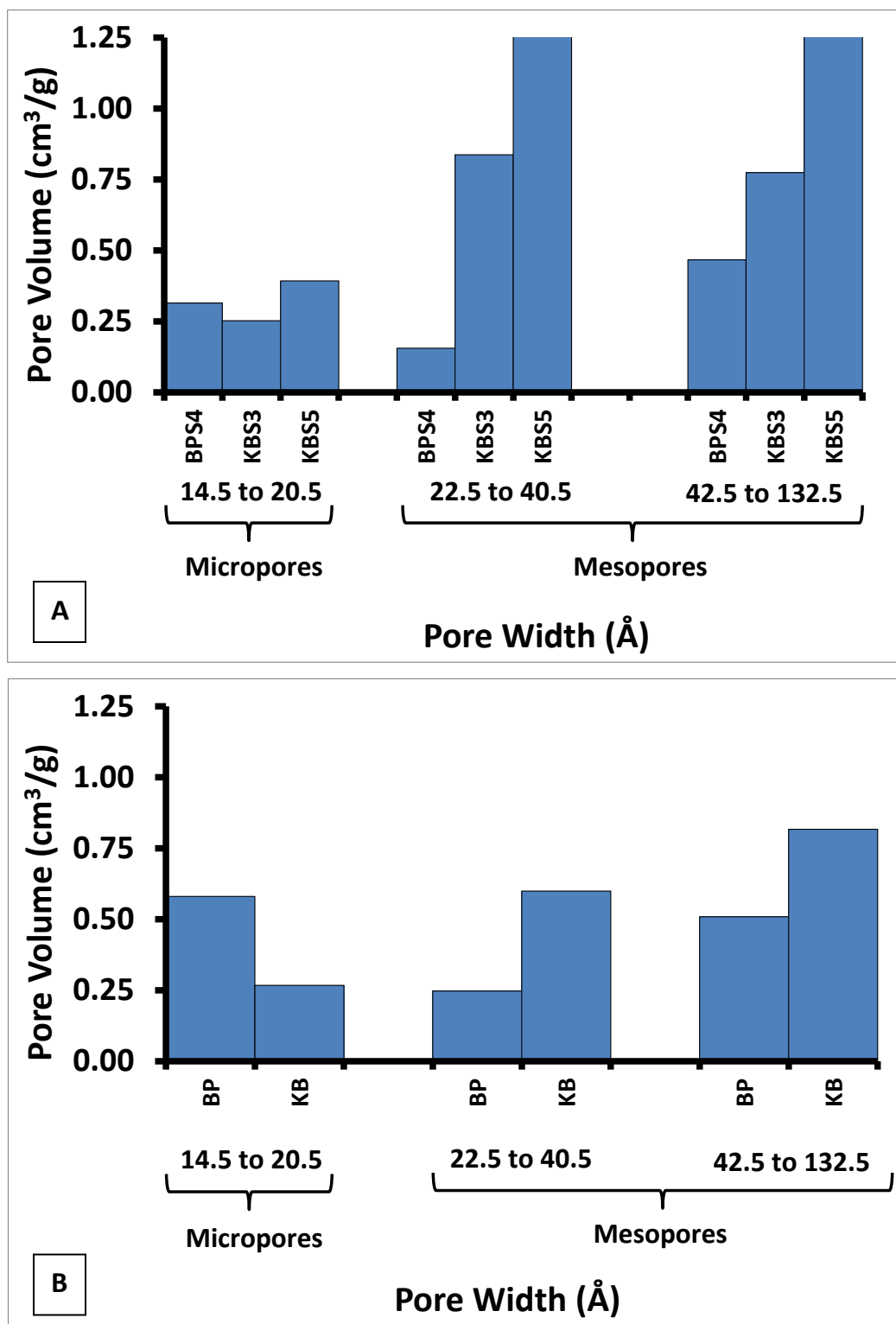


Figure 3.44. Histogram comparing the pore size of the (A) best samples of the BP and KB series and (B) the bare carbon supports.

It has been clearly demonstrated that the structure of the catalyst support plays a key role in the formation of the active site. Another key aspect to successful synthesis of these materials is the nitrogen content, which is linked to the iron uptake. Table 3.8 lists the key characteristics relating to the performance of the BP and KB series and compares them to the nitrogen and iron content. It is evident that BPS4Fe700 outperforms the KB materials in regards to onset potential, limiting current, and hydrogen peroxide production.

Theoretically the higher the nitrogen content, the greater the iron uptake and the more active the catalyst material. This was not the trend observed when comparing the BP and KB series. Table 3.8 shows that although BPS4Fe700 does not have the highest nitrogen or iron content, this material still has the best overall activity. There are likely multiple contributors to this aspect including the type of nitrogen present as well as the level of graphitization that occurs upon heat treatment.

Figure 3.45 shows the XPS for BPS4Fe700 and KBS4Fe700 and compares the types of nitrogen present in each sample. It can be seen that the nitrogen functionalities do differ between the two carbon supports. Both samples have the largest contribution attributed to pyridinic nitrogen which is thought to be the ideal functionality for coordination to iron.<sup>65</sup> Differences arise in the relative amount of pyridone with a larger relative contribution seen for BPS4Fe700. In addition to this, there is also a contribution from pyridinium for BPS4Fe700 not seen in KBS4Fe700. Both pyridinium and pyridone result from the protonation or oxidation of the aphen molecule respectively, which prevents the coordination to iron and formation of the active site. The relative amount of pyridinic nitrogen is higher for KBS4Fe700 despite lower activity; however the pyridinic nitrogen functionalities are not necessarily involved in an active site. Although these functionalities may contribute to the differences seen in the activity of the materials, it is likely that the ability to form active sites during heat treatment has a larger impact.

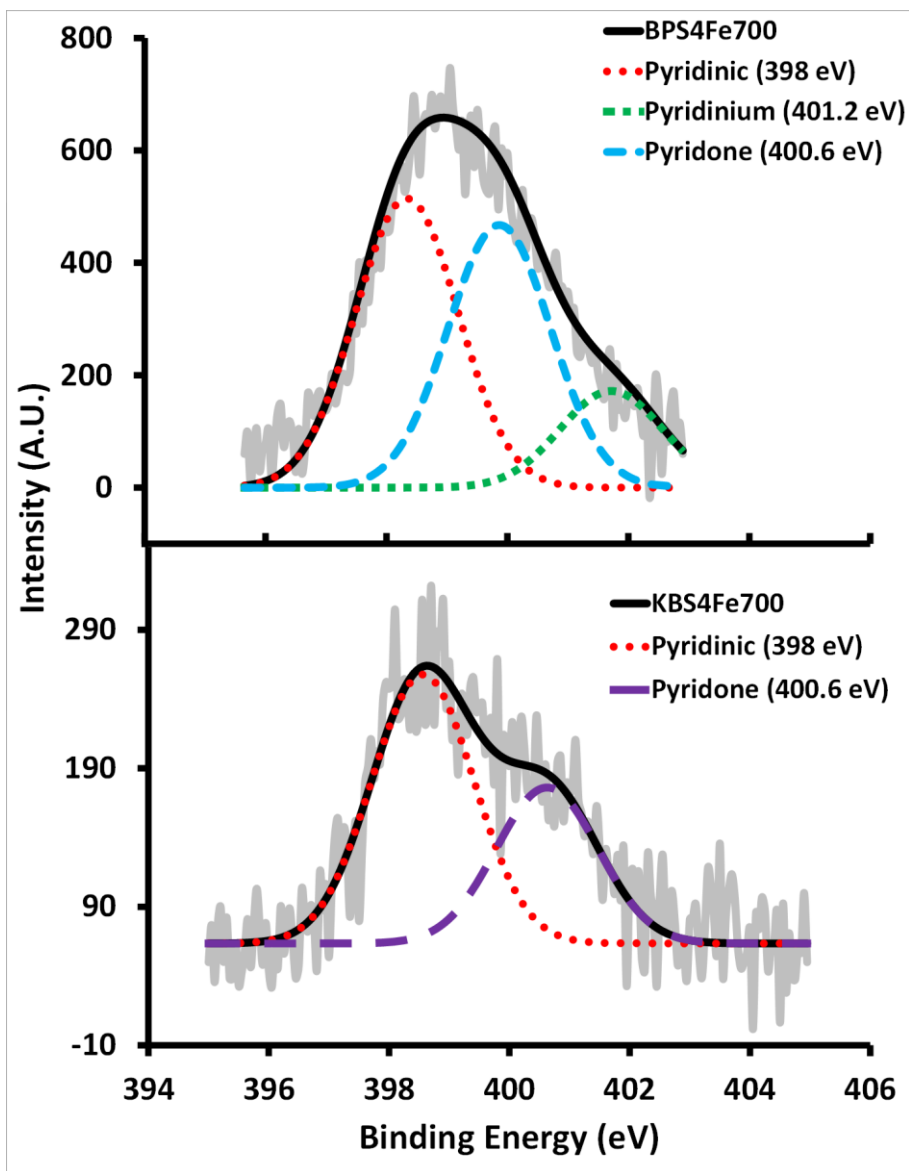


Figure 3.45. Comparison of the N-1s Narrow scan XPS spectra for BPS4Fe700 and KBS4Fe700.

It is likely that, due to the low level of graphitization occurring with KB, the nitrogen present is unable to form active sites correctly. Without the correct amount of rearrangements during the synthesis, the materials are unable to best utilize the nitrogen and iron. This stresses the importance of selecting a carbon support that is able to integrate the nitrogen containing portion and successfully form active sites during the heat treatment step.

Table 3.8. Summary of key features for the best catalysts of each series.

Characteristic/Sample	BPS4Fe700	KBS3Fe700	KBS5Fe700
Onset Potential (V vs. RHE)	0.78	0.68	0.70
Limiting Current (mA/cm <sup>2</sup> )	-5.52	-3.23	-3.02
H <sub>2</sub> O <sub>2</sub> Production (%)	0.59	3.16	6.04
Nitrogen Content (%)	3.26	1.96	4.04
Iron Content (%)	3.95	2.51	10.4

The importance of the different components of the catalyst materials has been demonstrated. Although the onset potential, limiting current, and hydrogen peroxide production are significant measures of the catalysts' success, the mechanism of the ORR is also an important aspect.

Figure 3.46 compares the results of the Koutecky-Levich analysis for BPS4Fe700, KBS3Fe700, and KBS5Fe700 to the theoretical 2 and 4 electron processes. Here it can be seen that all three samples follow close to the theoretical 4 electron process indicating that both supports are able to form some ideal active sites. Although samples synthesized with KB as a support do not perform as well as samples made with BP, the overall ORR mechanism appears to be closer to the four electron process for the series synthesized from KB (Figure 3.31) than for BP (Figure 3.14). The only sample close to the theoretical 4 electron curve is BPS4Fe700, with the remaining samples in the BP trend either lining up with the 2 electron process or lying outside either trend. Taking this into account as well as the analysis of the overall pore structure differences between KB and BP, it is likely that the micropores offer a better structure for an active site formation resulting in better onset potentials as seen with BP. The mesopores also form active sites and since there is a higher volume of mesopores, a better limiting current can be achieved.

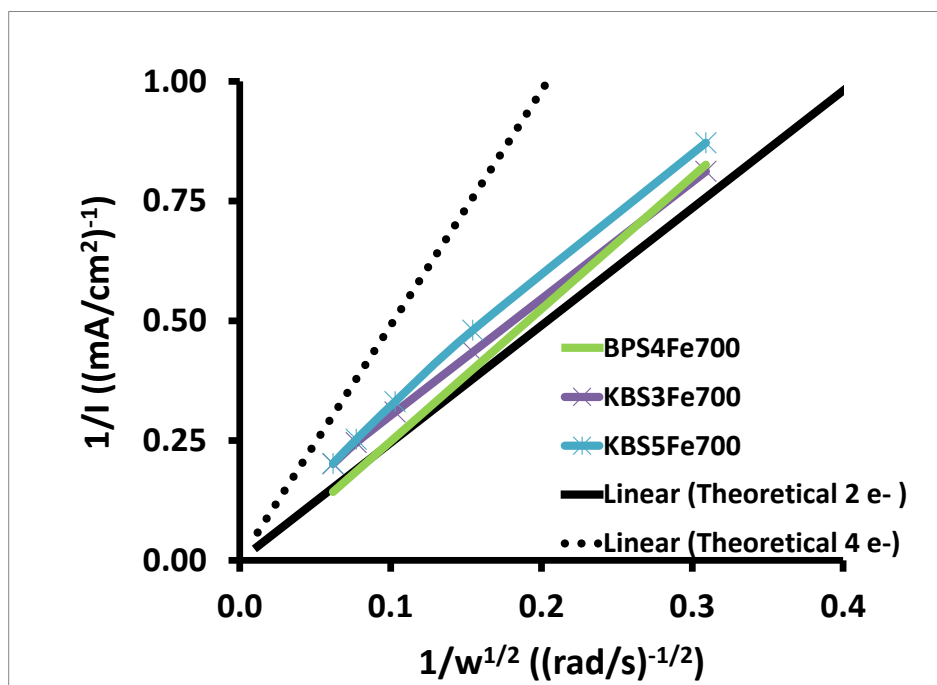


Figure 3.46. Koutecky-Levich analysis for the best samples of the BP and KB series compared to the theoretical two and four electron processes.

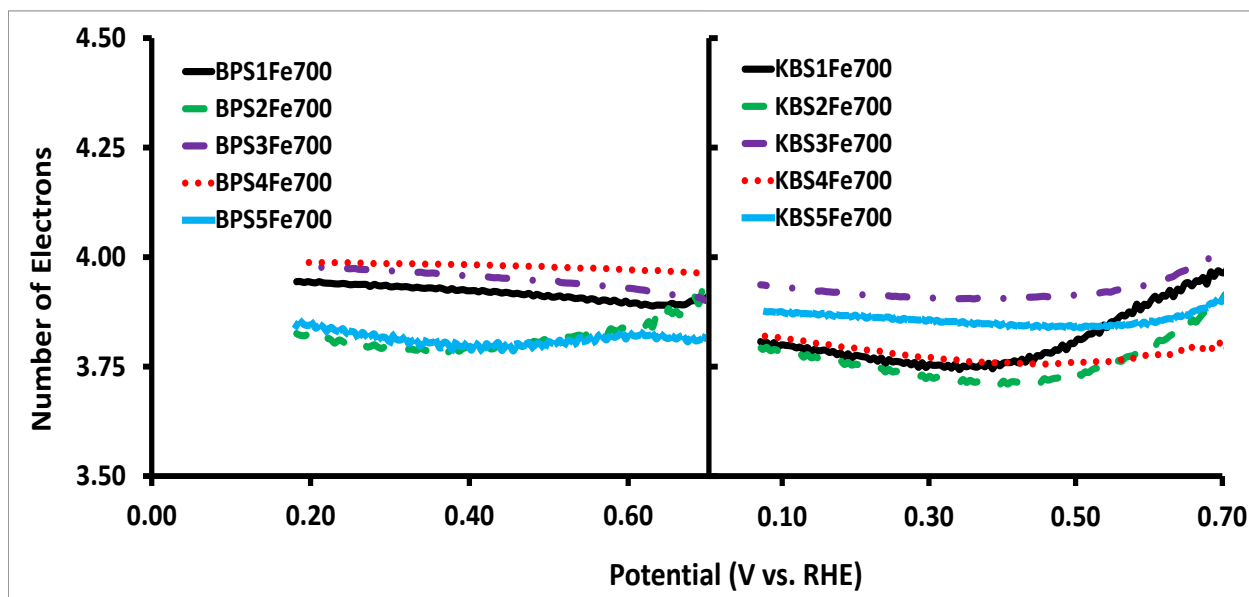


Figure 3.47. Comparison of the number of electrons transferred for the BP and KB series as calculated from the collected ring data.

Analysis of the ring data (Figure 3.47) does not support this discrepancy seen in the Koutecky-Levich analysis, but instead indicates that both carbon supports follow the four electron pathway with slightly differing mechanisms. Since Koutecky-Levich shows primarily a two electron process for the overall BP series, but data collected at the ring indicates a four electron

process, it is likely that the true mechanism for the ORR at the active sites in BP occurs via the hydrogen peroxide intermediate with complete conversion to water as a second step at a different catalytic site (2+2 mechanism).

The carbon support was determined to have a large impact on the overall performance of the catalyst materials. It was clear that the modification of the carbon support via the diazonium coupling reaction was more successful for the BP series. This is likely due to the level of graphitization present with each carbon. KB is more graphitic than BP and therefore has fewer surface oxides groups. This gives KB a more hydrophobic nature which makes it more challenging to react in an aqueous environment. The extent of modification via the diazonium coupling reaction is a key step in this synthesis and needs to be optimized for each new material used.

To a lesser degree, the porosity of the material also impacted the overall performance of these catalysts. BP, having a more microporous structure, formed far more active sites than seen in KB. The amount of graphitization that occurred via heat treatment was also much higher for BP stressing the importance of the heat treatment step in creating active sites. The amount of graphitization that occurs during this step is crucial to the final catalyst performance.

This is further supported by the XPS results which show that the KBS5Fe700 contained significantly more nitrogen than BPS4Fe700 despite a lower activity. This indicates that, although the nitrogen content is an important factor, more important is the ability of the carbon support to successfully incorporate the nitrogen and iron.

Overall, when comparing the BP series to the KB series, BP resulted in better overall performance. This is likely due to the wettability and disordered structure of BP as this support was able to successfully undergo the diazonium coupling reaction and undergo sufficient rearrangements during heat treatment. KB is still a promising material with activity approaching BP and properties that show potential for a better catalyst if optimal conditions are used. It was seen that KB contained mainly the pyridinic nitrogen added during the diazonium coupling reaction which allows for much better control over the active site. Further studies using KB may offer more insight into the structure and formation of the active site.

**Chapter 4**  
**Modifications to NPMC**  
**Synthesis**

Following the study of the carbon support and optimization of the aphen loading, studies were completed to determine if further modifications to the procedure improved the catalysts' activity. Since it was determined that the BP series was a better carbon support than KB largely due to its ability to react with aphen in the diazonium coupling reaction, further experiments were completed using BP as well as the ratio for the best material from the BP series (1.18 mmol aphen/g carbon). This chapter will discuss the use of an alternate iron salt and a unique approach to the synthesis via utilization of a glycerol reflux.

#### 4.1 Changing the Iron Salt

Two series of samples were prepared using iron(II) acetate in place of the iron(III) chloride as it has been used in literature to create active materials.<sup>38</sup> BPS1-4 were used as the starting materials to determine if the previously seen trend (Figure 3.13 and Figure 3.30) remained the same when a new iron source was used. Two different solvents were used for the iron uptake process; deionized water (as with the original series), and a 50:50 mixture of isopropyl alcohol and water to help wet the carbon materials. Figure 4.1 and Figure 4.2 compare the ORR activity and hydrogen peroxide production for these two series soaked in iron(II) acetate. The results of these two studies show that samples soaked in the 50:50 mixture of IPA and deionized water resulted in better onset potential than ones soaked in water alone, however the H<sub>2</sub>O<sub>2</sub> production is slightly better for the latter series.

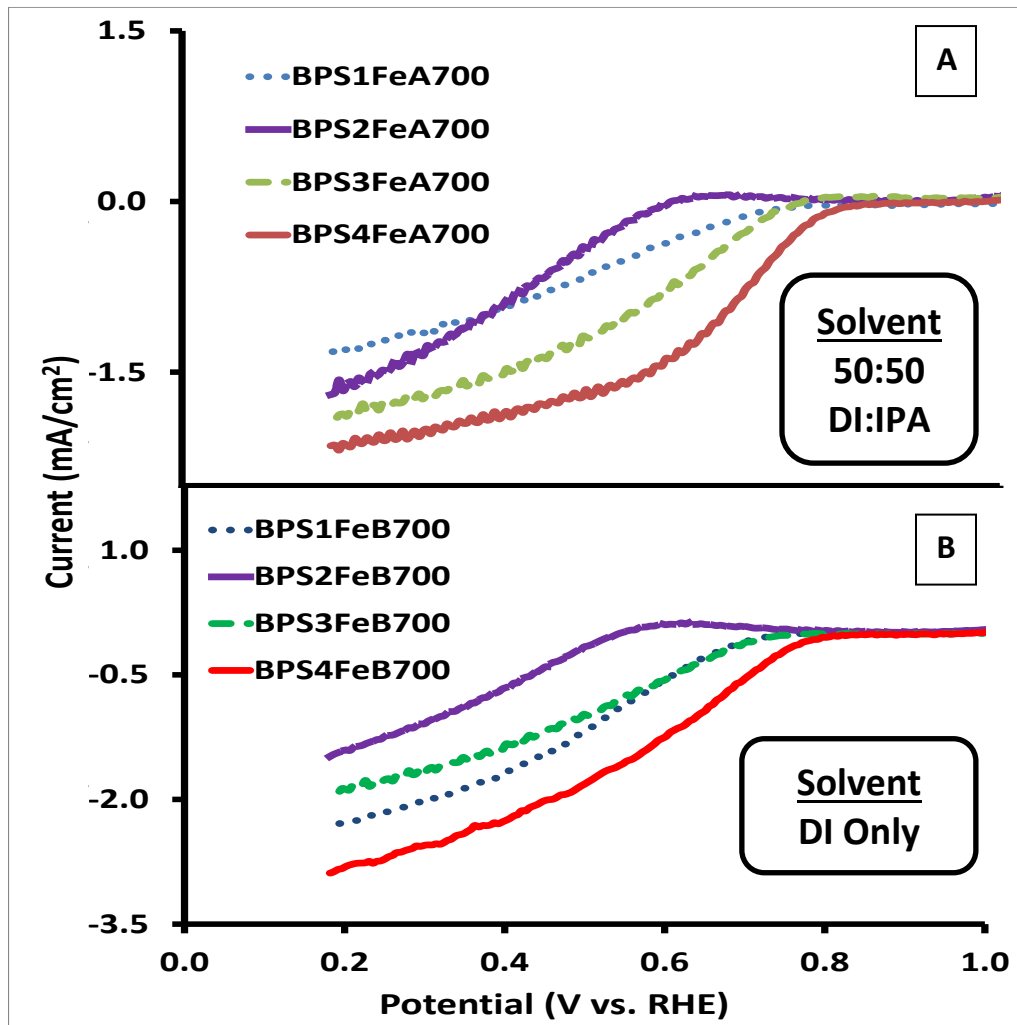


Figure 4.1. Comparison of the activity of the BP series prepared with iron(II) acetate in (A) a 50:50 mixture of deionized water and isopropyl alcohol and (B) deionized water. Measurements were obtained at 900 RPM in an O<sub>2</sub> saturated 0.5M solution of sulphuric acid.

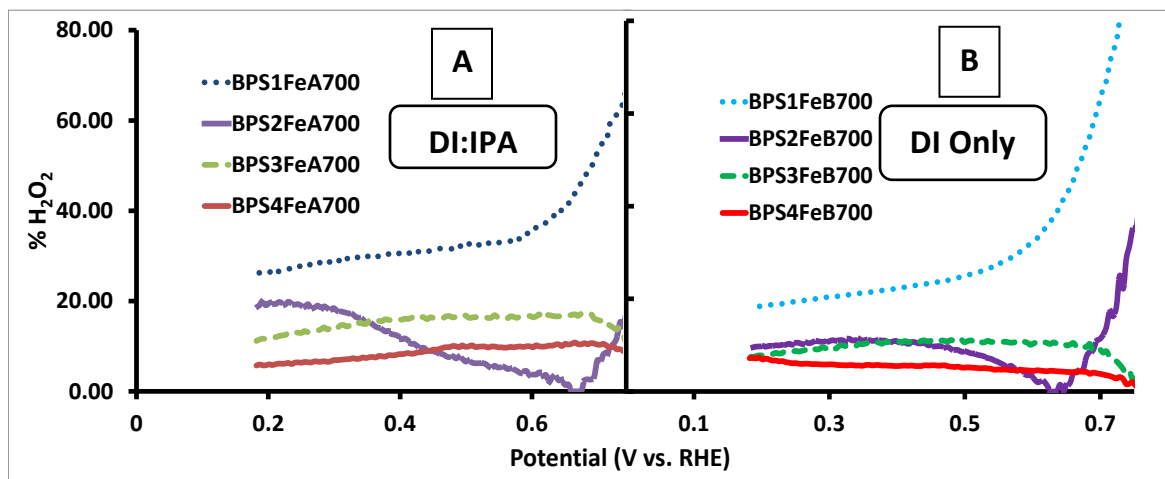


Figure 4.2. Comparison of the hydrogen peroxide production of the BP series prepared with iron(II) acetate in (A) a 50:50 mixture of deionized water and isopropyl alcohol and (B) deionized water.

Figure 4.3 compares the achieved onset potential to the ratio for both series and clearly illustrates the differences in the two series. A large deviation appears with the second ratio; however this may be due to experimental errors. The fact that it occurs for both series indicates a possible deviation in the preparation of the carbon support and diazonium coupling reaction or iron uptake experiment. Overall the activity trends with the aphen loading; a higher activity is achieved with a higher amount of aphen. Figure 4.4 compares the number of electrons transferred for each ratio as calculated from the collected ring data. For both series the best ratio results in a total transfer of four electrons which is not supported by the Koutecky-Levich analysis (Figure 4.5). As with the previous BP series, this discrepancy indicates that the mechanism of the ORR for these catalyst materials forms a hydrogen peroxide intermediate that is likely reduced to water at another catalyst site.

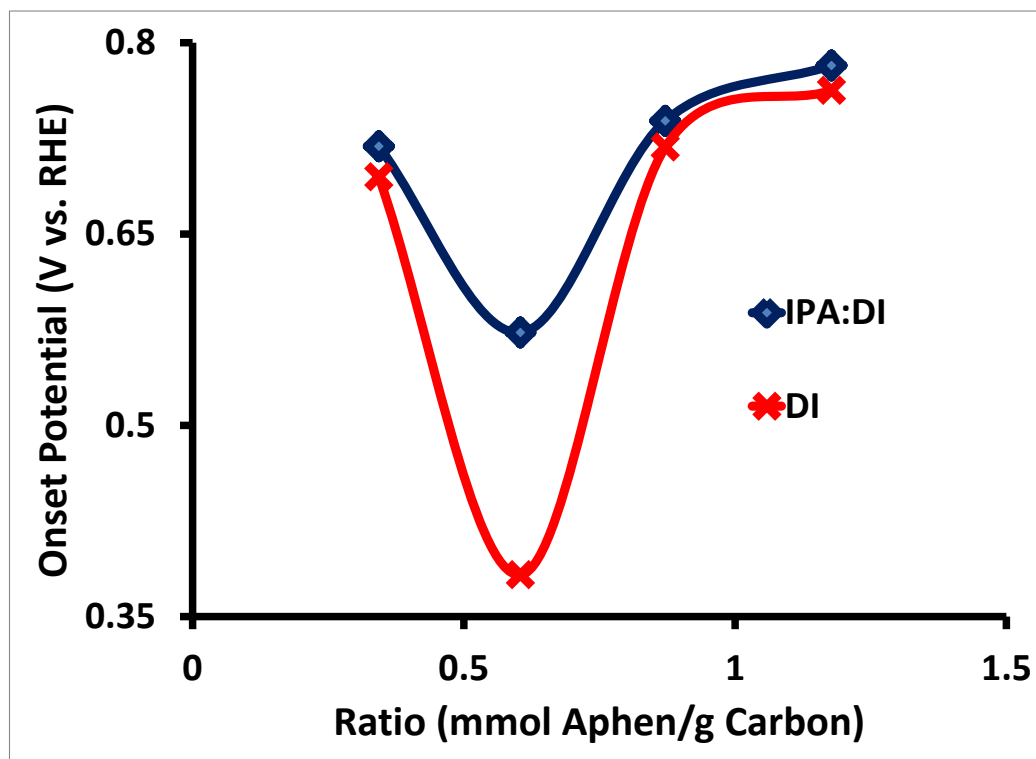


Figure 4.3. Comparison of the trend in onset potential of the BP series prepared with iron(II) acetate in various solvents.

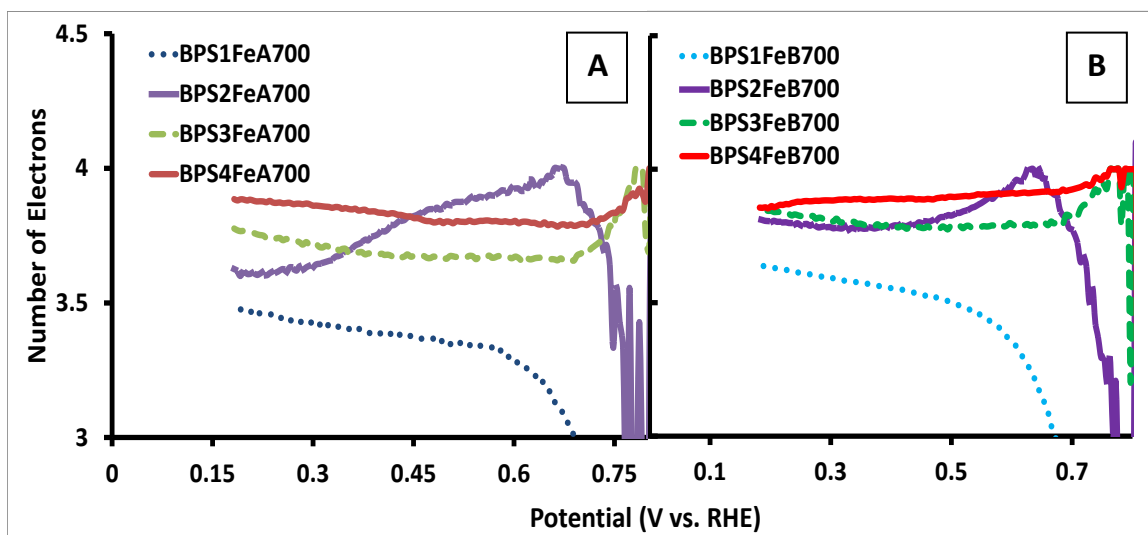


Figure 4.4. Comparison of the number of electrons transferred for the BP series prepared with iron(II) acetate in (A) a 50:50 mixture of deionized water and isopropyl alcohol and (B) deionized water.

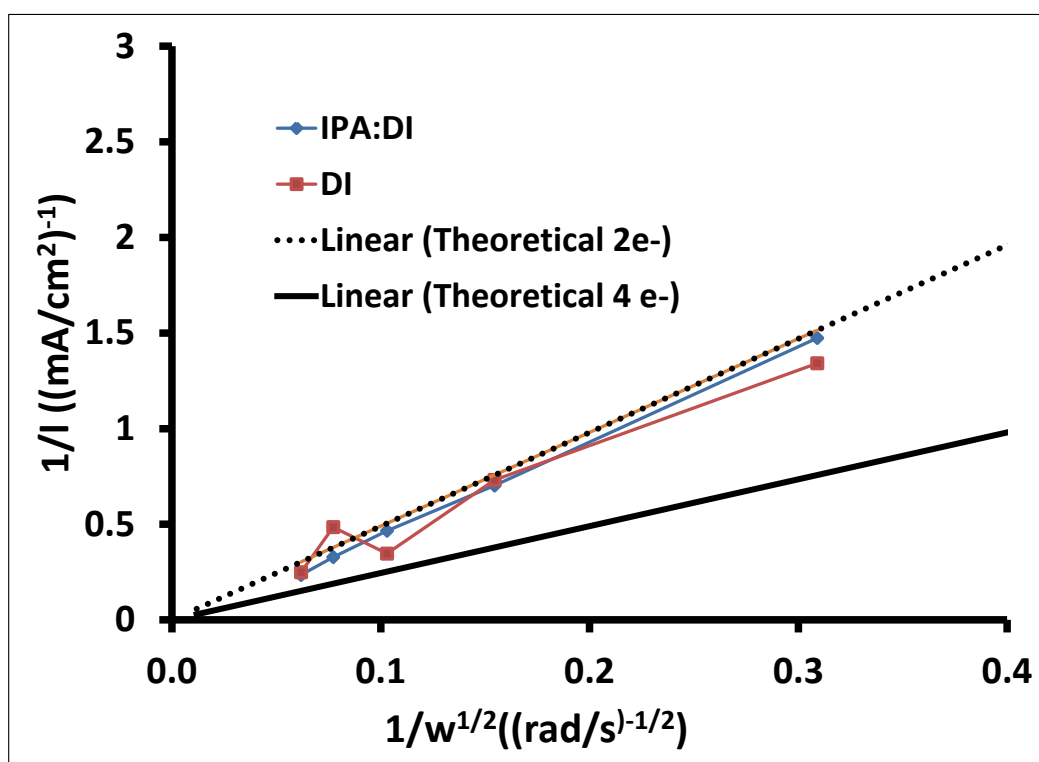


Figure 4.5. Koutecky-Levich analysis for the sample treated in ammonia compared to the theoretical 2 and 4 electron curves.

Figure 4.6 compares the activity of the best samples soaked in iron(II) acetate in either IPA/DI or DI alone to BPS4Fe700 (from the original series, soaked in iron(III) chloride). Overall neither catalyst soaked in an iron(II) acetate solution outperformed the  $\text{FeCl}_3$  based material though the

onset potential of BPS4FeA700 did have a comparable onset potential to BPS4Fe700. Due to the similar onset potential, the same trend in mechanism, but a discrepancy in limiting current, it is likely that the samples treated with iron(II) acetate do not have as many active sites as BPS4Fe700.

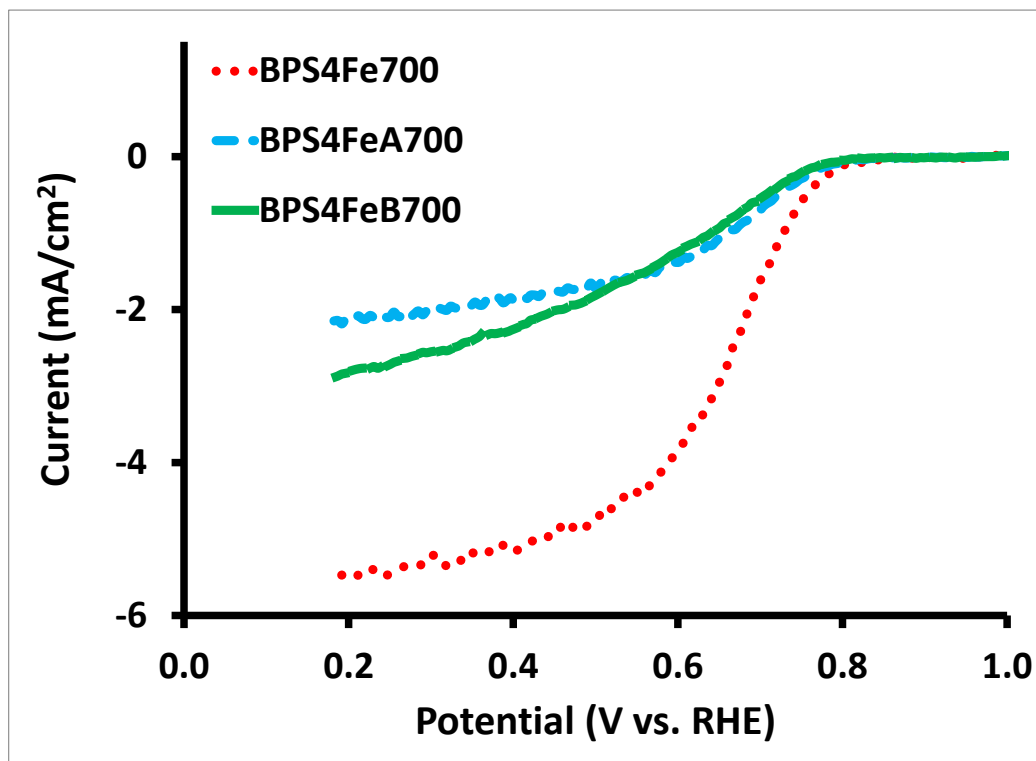


Figure 4.6. Comparison of the activity of the best sample of the BP series prepared with iron(II) acetate in a 50:50 mixture of deionized water and isopropyl alcohol or deionized water. Measurements were obtained at 900 RPM in an  $O_2$  saturated 0.5M solution of sulphuric acid.

It was expected that samples prepared with iron(II) acetate would yield materials with activity comparable to that in literature using this iron salt.<sup>38</sup> The use of an alternate iron salt could potentially alter the iron uptake; in order to investigate this aspect, TGA was completed to quantify the iron. Figure 4.7 shows the TGA results for BPS4FeA700, BPS4FeB700, and BPS4Fe700. It can be seen that the iron uptake was significantly larger using iron(II) acetate in the iron uptake step, resulting in ~25% iron for both BPS4FeA700 and BPS4FeB700 compared to ~4% for the best samples soaked in iron(III) chloride. It is possible that the acetate ligand is more weakly bound to the metal allowing for more available iron during the iron uptake step. The oxidation state of the metal may also play a role in its ability to be coordinated as  $Fe^{2+}$  is the oxidation state of iron in the active site. Considering the large increase in iron and no gains in the activity of the samples, it is likely that this excess iron is not present in an active site.

Previous work has indicated that the optimal loading of iron for NPMC is as little as 0.2 wt %<sup>37</sup> with amount above this resulting in a decline in activity. The wt% of iron(II) acetate added in this study was ~ 20%, indicating that the additional iron added by the iron(II) acetate salt would have decreased the activity of the prepared samples.

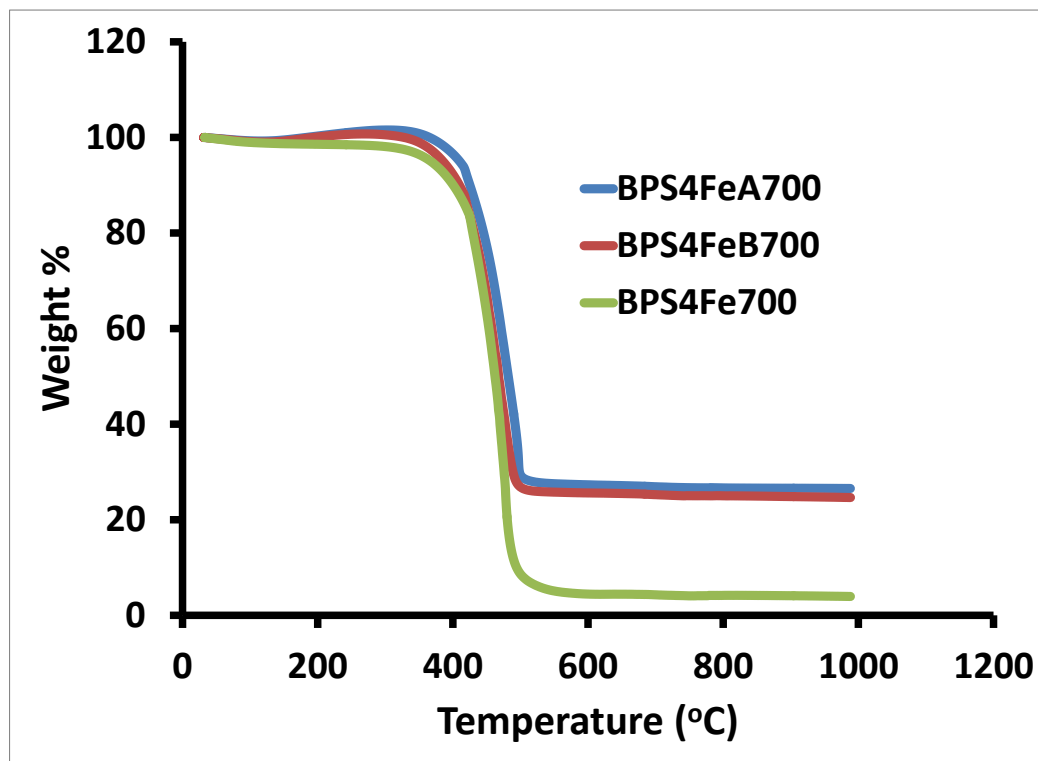


Figure 4.7. Determination of the iron content for select samples of the iron(II) acetate series. Measurements were performed under flowing air with temperatures ramped from 20-1000 °C at 20 °C min<sup>-1</sup>.

Further supporting the detrimental impacts of the excess iron is the sharp peak seen in the initial CV obtained for BPS4FeA700 in an N<sub>2</sub> purged 0.5 M sulphuric acid solution (Figure 4.8). This peak has been observed in other NPMCs<sup>47</sup> and is indicative of the formation of iron carbide. Instead of forming active sites, excess iron is able to bond directly with the carbon support creating a passivating layer which blocks the formation of more active sites. In order to best utilize the iron(II) acetate salt a better method of coordination is needed to ensure the optimal amount of iron is loaded.

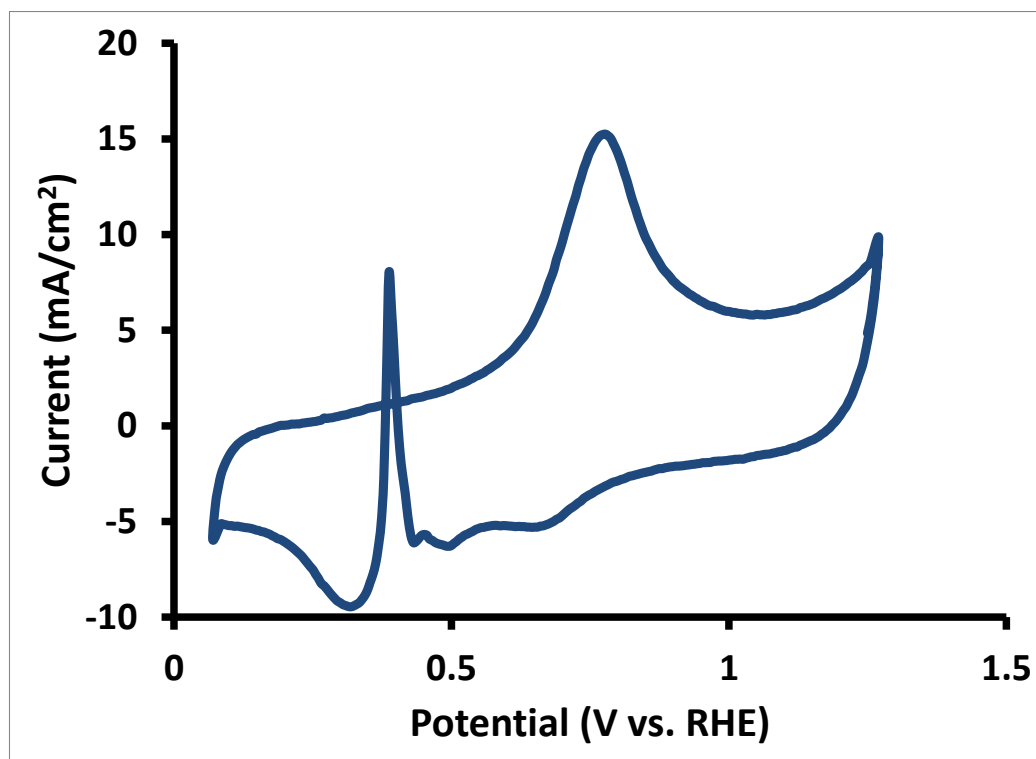


Figure 4.8. Initial CV scan for BPS4FeA700 obtained in an  $N_2$  saturated 0.5 M solution of sulphuric acid.

#### 4.1.1 Varying Concentrations

In order to maintain an optimal loading of iron, BPS4 was soaked in a lower concentration of the iron(II) acetate solution. Originally samples were soaked in a 10mM solution of iron(II) acetate ( $\sim 20$  wt%) to follow the procedure used for the iron(III)chloride samples. The modified procedure used a 0.35mM solution ( $\sim 0.76$  wt%) using the 50:50 mixture of IPA and DI as the solvent. Figure 4.9 clearly shows that the lower iron concentration did not yield a catalyst that exceeds the best material in the BP series. Table 4.1 compares key parameters of the catalyst prepared with the lower iron concentration to the original iron(II) acetate samples. The new treatment did not yield a better onset potential but did provide improvements in the limiting current and hydrogen peroxide production.

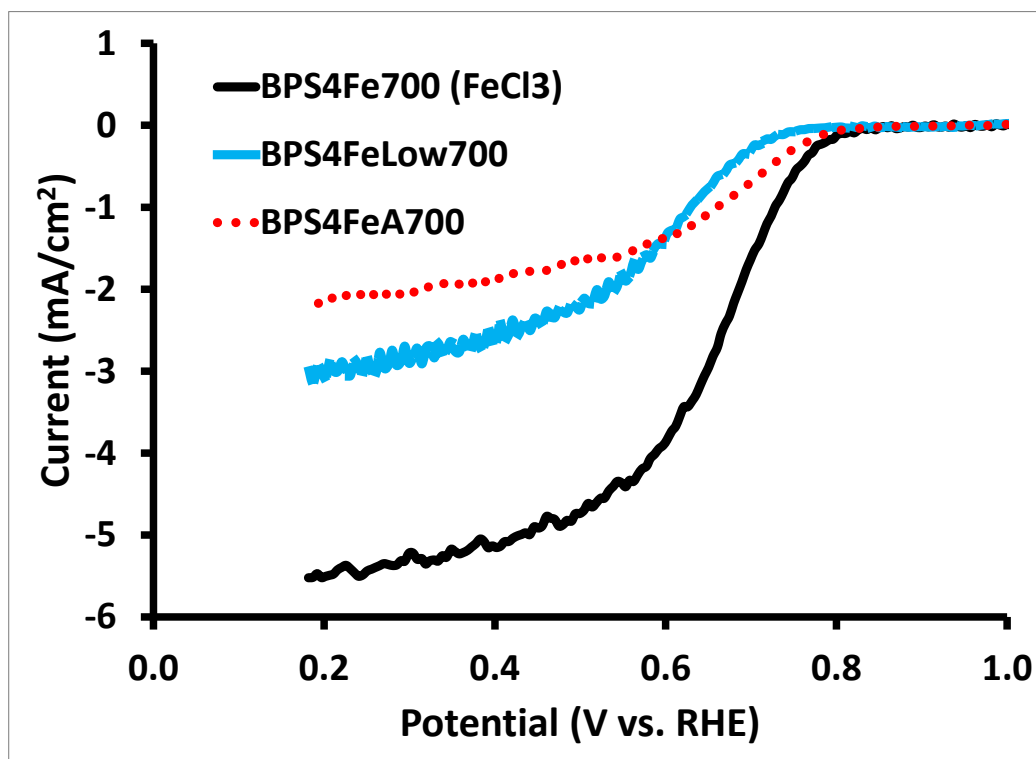


Figure 4.9. Comparison of the sample prepared with a lower concentration of iron(II) acetate to the best sample of the BP series and the platinum standard. Measurements were obtained at 900 RPM in an O<sub>2</sub> saturated 0.5M solution of sulphuric acid.

Table 4.1. Comparison of key parameters for the sample prepared with a lower concentration of iron(II) acetate to the best catalyst treated with iron(II) acetate.

Sample	Onset Potential (V vs. RHE)	Limiting Current (mA/cm <sup>2</sup> )	Hydrogen Peroxide (%)
BPS4FeLow700	0.73	-2.94	3.54
BPS4FeA700	0.78	-2.15	5.71

Overall an improvement was seen with the limiting current and hydrogen peroxide production, indicating that more active sites are now accessible with the absence of excess iron. Despite these improvements, the onset potential decreased which may be attributed to too little iron or non-optimal iron uptake procedures. Koutecky-Levich analysis (Figure 4.10) indicates that the BPS4FeLow700 is a catalyst that follows more closely to the four electron process than BPS4FeA700. The average number of electrons (calculated from the ring data) for BPS4FeLow700 and BPS4FeA700 were 3.9 and 3.8 respectively; indicating slightly different processes are occurring on the catalyst surface but overall both materials transfer the correct amount of electrons. This iron(II) acetate uptake study indicates that the lower concentration of

iron helps to improve some aspects of the catalyst, but for a larger improvement optimization of the iron uptake needs to be completed.

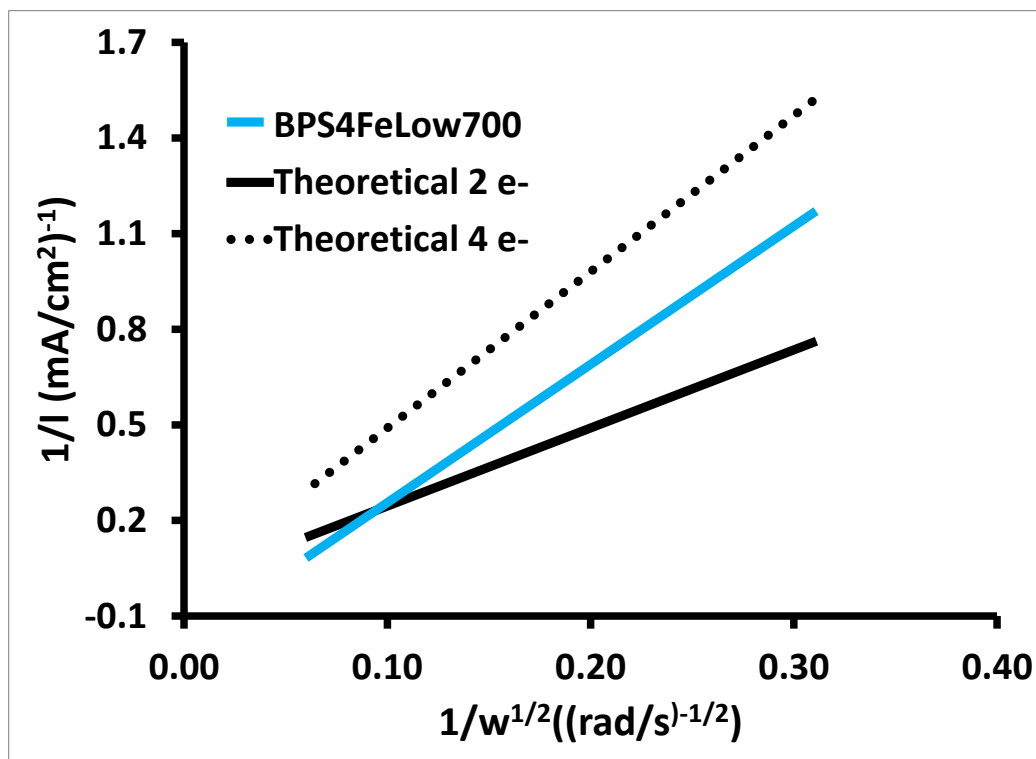


Figure 4.10. Koutecky-Levich analysis for the sample prepared with a lower concentration of iron(II) acetate compared to the theoretical 2 and 4 electron curves.

#### 4.1.2 Acid Leached

Another method to remedy the problems associated with excess iron is to perform an acid leaching step as part of the synthesis. This has been shown to reduce the amount of iron and increase the performance of NPMCs.<sup>38</sup> BPS4FeA700 was soaked in a sulphuric acid solution (with no further heat treatment) to remove excess iron, but no improvement was seen in any parameters for this sample. Figure 4.11 compares the activity of BPS4Fe700L to both BPS4FeLow700 and BPS4FeA700 and Table 4.2 summarizes the key catalyst parameters. Overall the acid treatment was more harmful to the catalyst than beneficial which can also be seen in the Koutecky-Levich plot (Figure 4.12). The activity trends towards the two electron process as BPS4FeA700 did, however it appears to have less of a linear relationship. In addition to this the number of electrons transferred (as calculated from the ring data) was  $\sim 3.6$  which shows a decrease from before the acid leaching. It is possible that the acid soaking step was not

completed correctly and that a different concentration of sulphuric acid or length of acid leaching is needed.

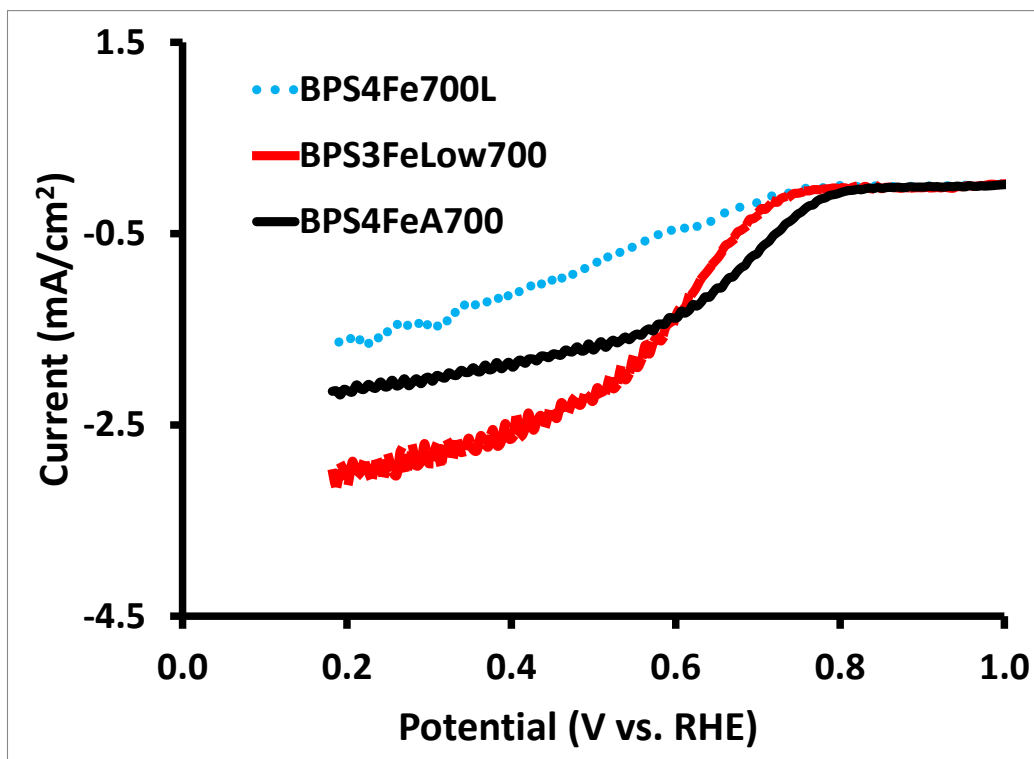


Figure 4.11. Comparison of the ORR activity for the sample leached in an acid solution to both BPS4FeLow700 and BPS4FeA700. Measurements were obtained at 900 RPM in an O<sub>2</sub> saturated 0.5M sulphuric acid solution.

Table 4.2. Comparison of key parameters for the acid leached sample to the best catalyst treated with iron(II) acetate.

Sample	Onset Potential (V vs. RHE)	Limiting Current (mA/cm <sup>2</sup> )	Hydrogen Peroxide (%)
BPS4Fe700L	0.73	-1.67	14.4
BPS4FeA700	0.78	-2.15	5.71

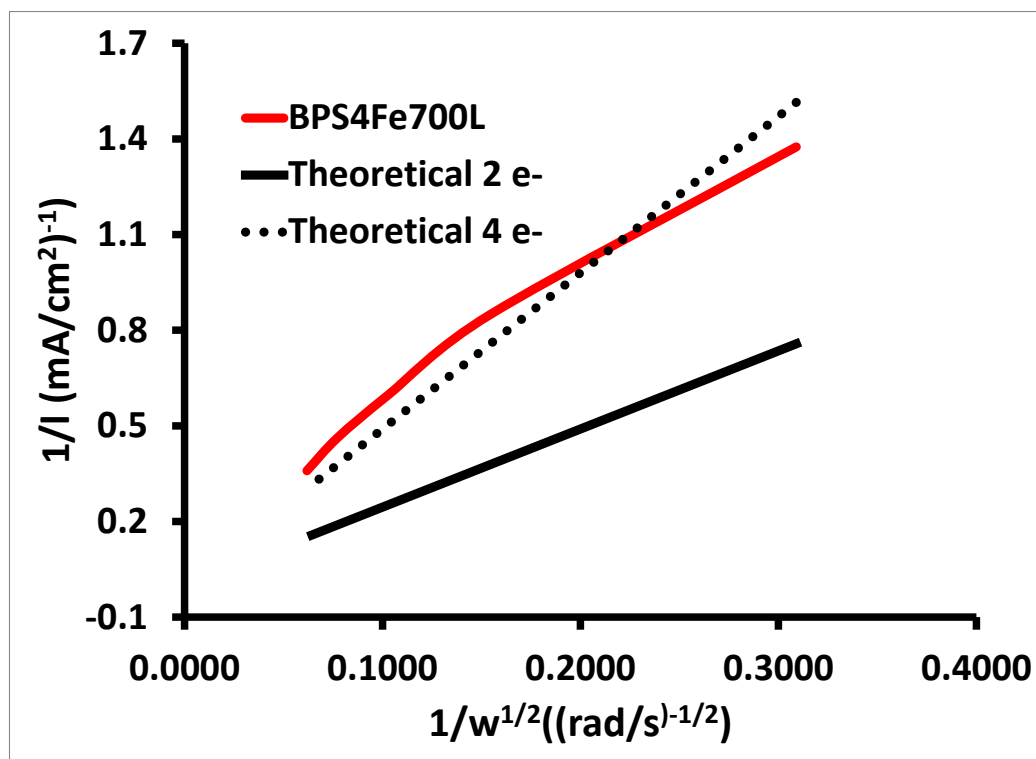


Figure 4.12. Koutecky-Levich analysis for the acid leached sample compared to the theoretical 2 and 4 electron curves.

## 4.2 Graphene Oxide and the Glycerol Reflux

The graphitic nature of graphene may allow for coupling of the aphen molecule on the edges of the carbon support (Figure 4.13). This would help facilitate the formation of the active site based on the expected slit pore structure (Figure 1.12). This size and shape also makes GO an ideal carbon support for a glycerol reflux as a replacement for the high temperature heat treatment. This technique is an inorganic synthesis used in literature to make organometallic compounds.<sup>74</sup> Since these reactions involve the coordination of various metals to large organic compounds it can be extended to coordinating iron to aphen modified GO.

The importance of the heat treatment step in the catalyst synthesis has been shown both in literature<sup>23</sup> and in this work (Section 3.2.1). It is necessary for altering the structure of the catalyst to coordinate iron to the correct number of nitrogens for the formation of the active site. However, the heat treatment also results in loss of some functionalities and non-ideal changes in structure. By utilizing GO, the sheet like structures may be able to align to form the same active site at a more moderate temperature (270 °C), much like those used to make inorganic compounds. For the previously discussed synthesis an amorphous carbon that will

undergo rearrangements to form the active site was ideal. Since a glycerol reflux does not require the same extent of rearrangements of the carbon support, a more graphitic structure would be appropriate in this method.

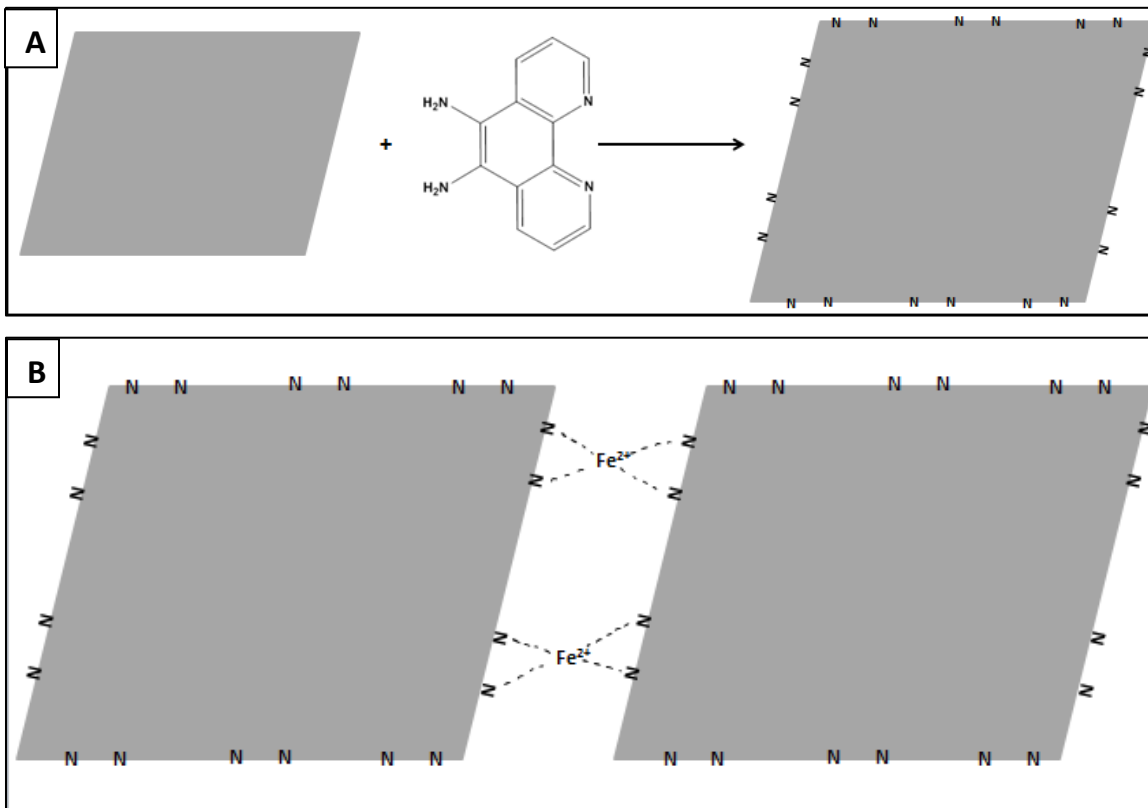


Figure 4.13. Proposed active site formation on graphene oxide. It is expected that aphen will functionalize the GO on edge sites (A) to facilitate the slit pore style formation of active sites (B).

#### 4.2.1 Graphene Oxide Synthesis

Graphene oxide was synthesized as described in section 2.1.1.3. The synthesis of graphene oxide was successful as shown in Figure 4.14 and Figure 4.15. Raman analysis indicates that changes in the graphite flakes did occur and the carbon material became less graphitic. TEM images of the synthesized material confirmed the presence of graphene sheets.

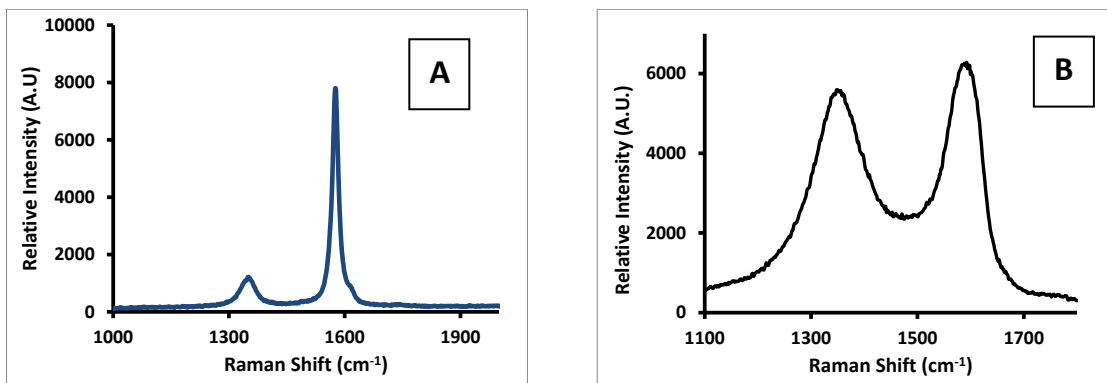


Figure 4.14. Comparison of Raman spectra for (A) graphite flakes and (B) synthesized graphene oxide.

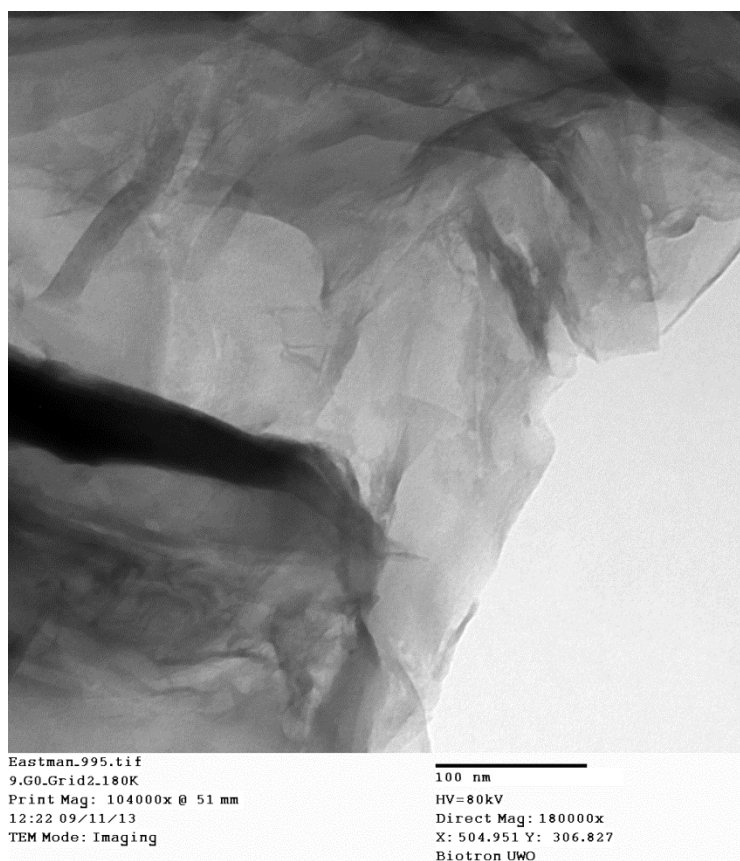


Figure 4.15. TEM image of the graphene oxide at 180000X magnification.

Prior to iron soaking (either via the conventional method or glycerol reflux) the GO underwent the diazonium coupling reaction to incorporate the nitrogen precursor. Figure 4.16 shows the CV obtained following the coupling reaction and compares it to unmodified GO. Small peaks are present in GOS4 similar to the peaks present in both the BP and KB series due to the redox activity of aphen. Comparing the CV of GOS4 to GO, it is clear that the peaks are due to the diazonium coupling modification and are indicative of the amount of aphen coupled to the

support. The smaller aphen peaks indicate that the coupling was not as successful on GO. The peaks are very small as well as asymmetric indicating less reversibility in the redox process. The tilt in the CV also indicates that there is more resistance in the catalyst layer which may impact charge transfer for these samples. Despite the poor success of diazonium coupling with GO, the remainder of the steps in the synthesis were carried out as with BP and KB as well as with a glycerol reflux.

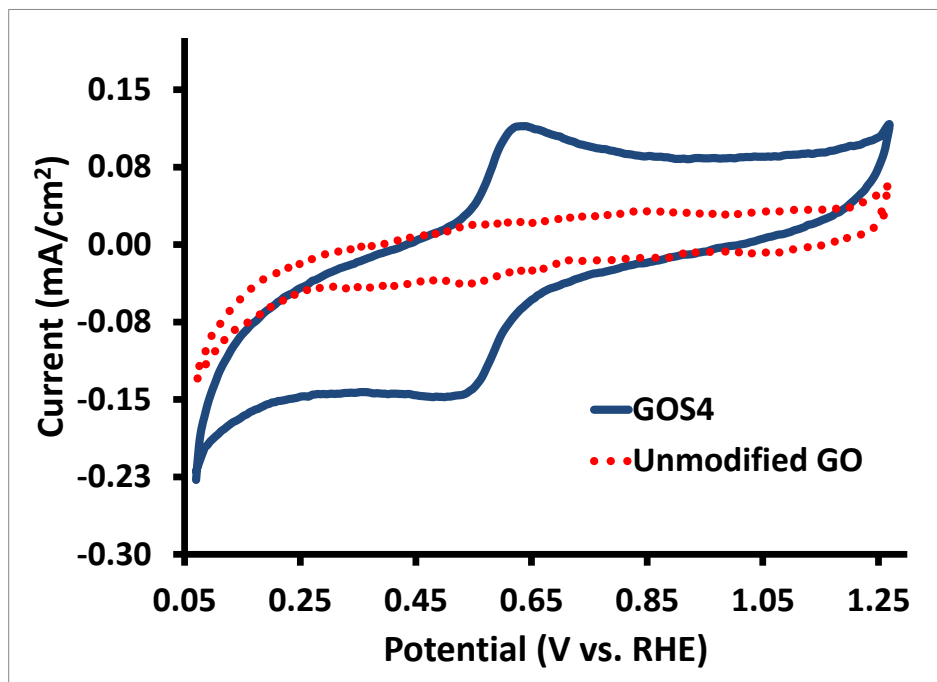


Figure 4.16. Comparison of the CV for graphene oxide reacted with aphen and the unmodified GO. Measurements were obtained in an N<sub>2</sub> saturated solution of 0.5M sulphuric acid.

#### 4.2.2 Conventional Catalyst Synthesis using GO precursor

A catalyst was prepared using graphene oxide as the carbon support with the same procedure utilized for the KB and BP samples. Figure 4.17 shows the results of this synthesis; it is clear that both the onset potential and limiting current of this sample do not exceed those of the best sample in the BP series. Comparing GOS4Fe700 to GO, it is evident that a modification did occur and the synthesized material is displaying more activity than the bare GO. Table 4.3 further emphasizes the poor performance of GOS4Fe700 with one of the lowest onset potentials and worst limiting current. Despite the poor performance the hydrogen peroxide formation is reasonable. In addition to this, analysis of the data collected at the ring indicates a full four electrons being transferred, indicating successful reduction to water.

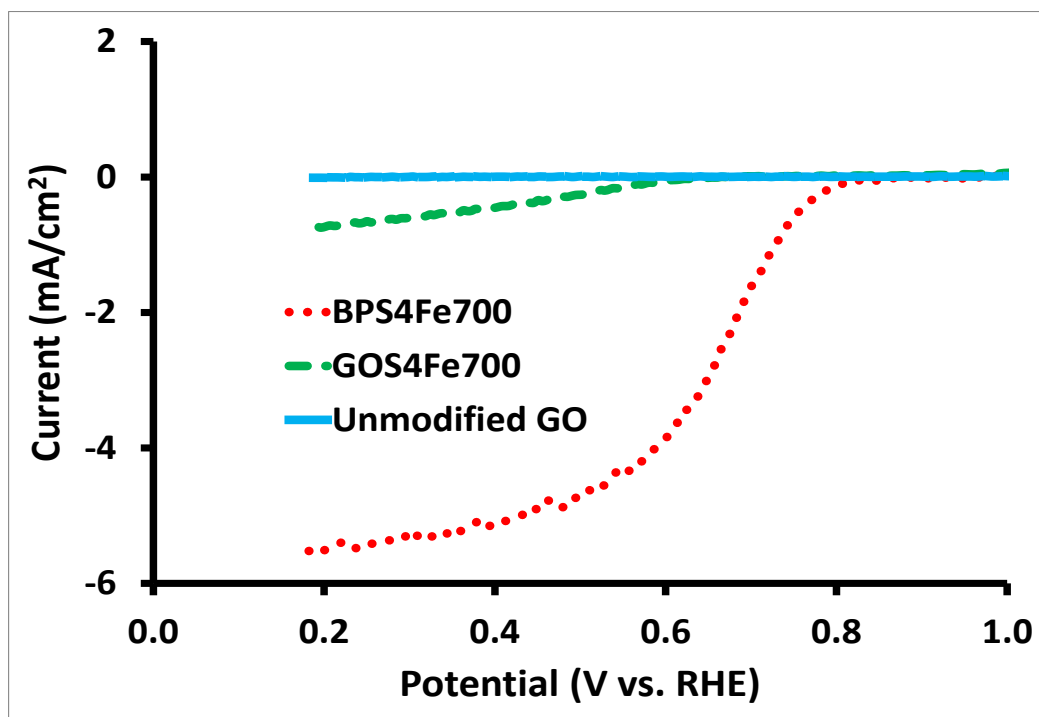


Figure 4.17. Comparison of the ORR activity of the graphene oxide sample compared to the best BP material as well as the unmodified GO. Measurements were obtained at 900 RPM in an O<sub>2</sub> saturated 0.5 M solution of sulphuric acid.

Table 4.3. Comparison of key parameters for the sample prepared with the GO support to the best catalyst of the BP series.

Sample	Onset Potential (V vs. RHE)	Limiting Current (mA/cm <sup>2</sup> )	H <sub>2</sub> O <sub>2</sub> (%)
GOS4Fe700	0.65	-0.771	3.77
BPS4Fe700	0.78	-5.52	0.59

Overall it was clear that the diazonium coupling reaction was not as effective on the graphene oxide, which contributes to poor activity later in the treatment. Although the reaction did not proceed as expected, the performance was still greater than that of bare carbon which indicates successful formation of some active sites. The amount, orientation, or type of active site needs to be further investigated to determine what occurred in this reaction process. TEM images (Figure 4.18) sheds some light on the structure of these materials. Analysis of the images on the 50 nm scale show many small structures present in the sample. At 10 nm it is clear that these structures show stacking of the graphene oxide sheets which likely occurred as a result of the loss of oxygen functionalities during the high temperature heat treatment.

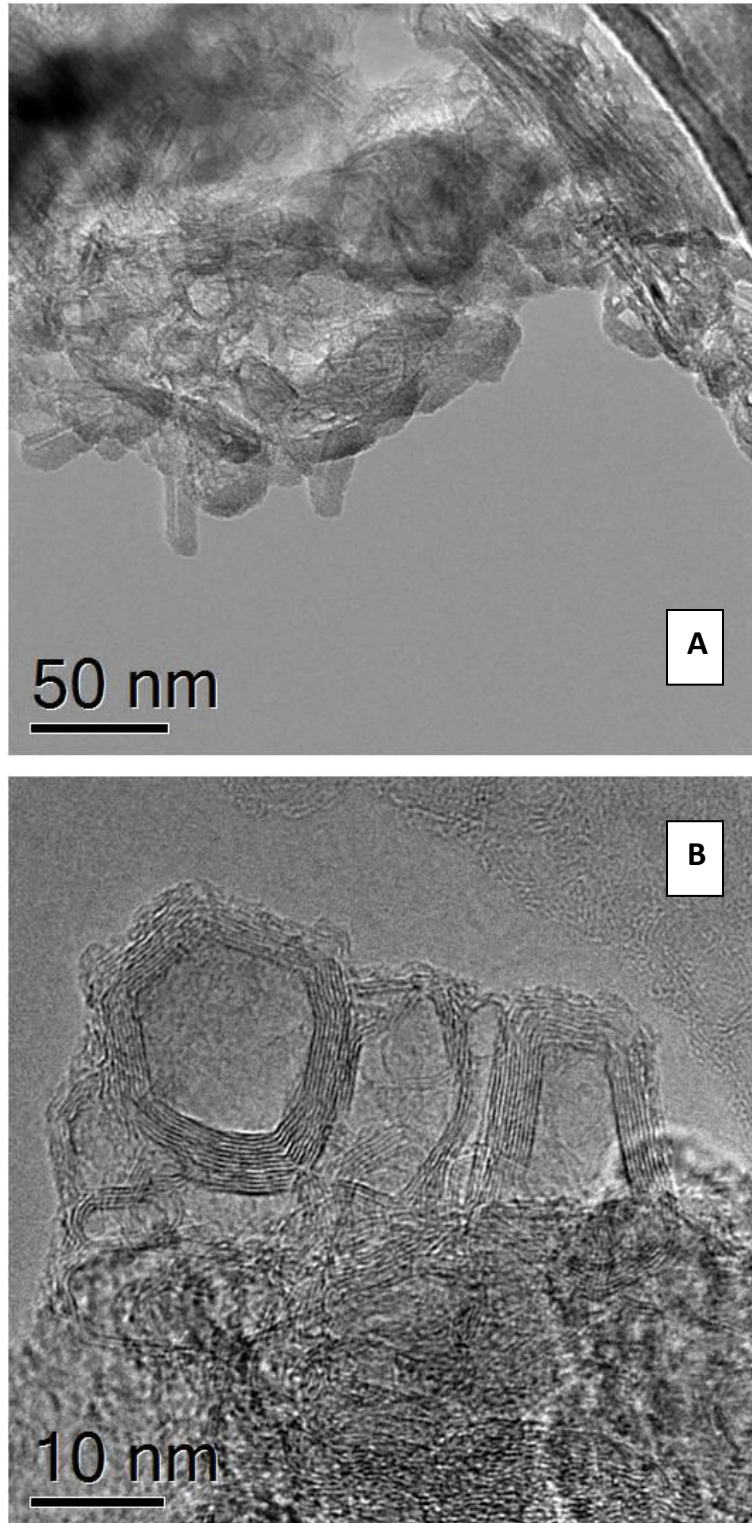


Figure 4.18. TEM images of samples prepared with graphene oxide at (A) 80000X magnification and (B) 400000X magnification.

### 4.2.3 Glycerol Reflux

Catalysts were prepared using graphene oxide as the carbon support and a glycerol reflux at 270°C. Figure 4.19 shows the results of this synthesis; it is clear that the performance of this sample does not exceed GOS4Fe700 though it does show better activity than unmodified GO. Table 4.3 further emphasizes the poor performance of GOS4FeGly with the lowest onset potential, poor limiting current, and high levels of hydrogen peroxide. Overall the glycerol reflux was not successful in synthesizing an active catalyst.

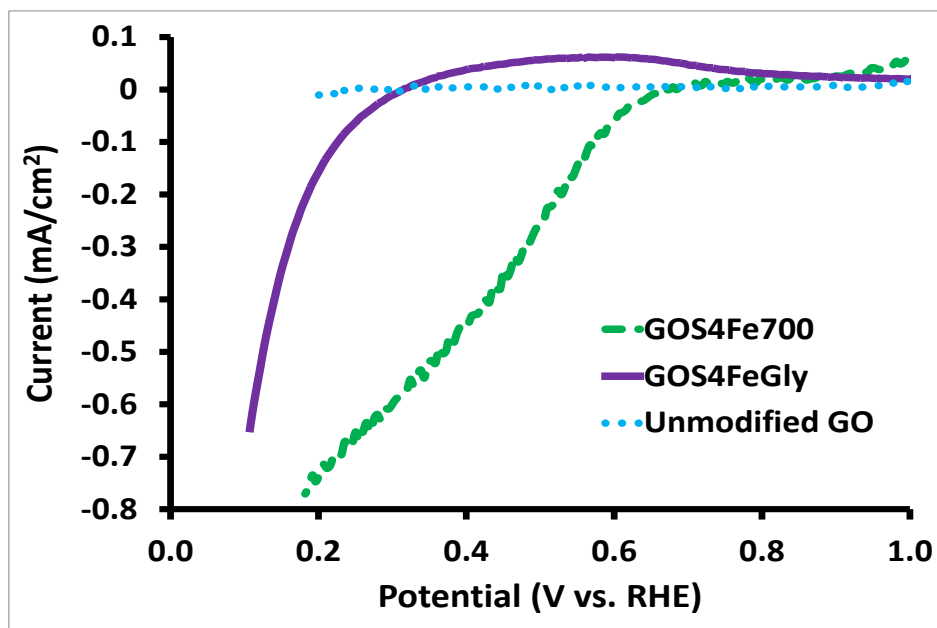


Figure 4.19. Comparison of the ORR activity of the graphene oxide sample prepared with a glycerol reflux compared to GOS4Fe700 and unmodified GO. Measurements were obtained at 900 RPM in an O<sub>2</sub> saturated 0.5M solution of sulphuric acid.

Table 4.4. Comparison of key parameters for the sample prepared from graphene oxide and glycerol reflux to the best catalyst of the BP series.

Sample	Onset Potential (V vs. RHE)	Limiting Current (mA/cm <sup>2</sup> )	H <sub>2</sub> O <sub>2</sub> (%)
GOS4FeGly	0.38	-0.646	12%
BPS4Fe700	0.78	-5.52	0.59

TEM images of GOS4FeGly indicate that the same stacking of the graphene sheets as seen with GOS4Fe700, which indicates that the oxygen functionalities are also lost during the gentle heat treatment that occurred during the glycerol reflux. It also appears that there are still sheets present in the sample and it is possible that active sites are forming however the conditions of the glycerol reflux are likely not optimal for the formation of active catalysts.

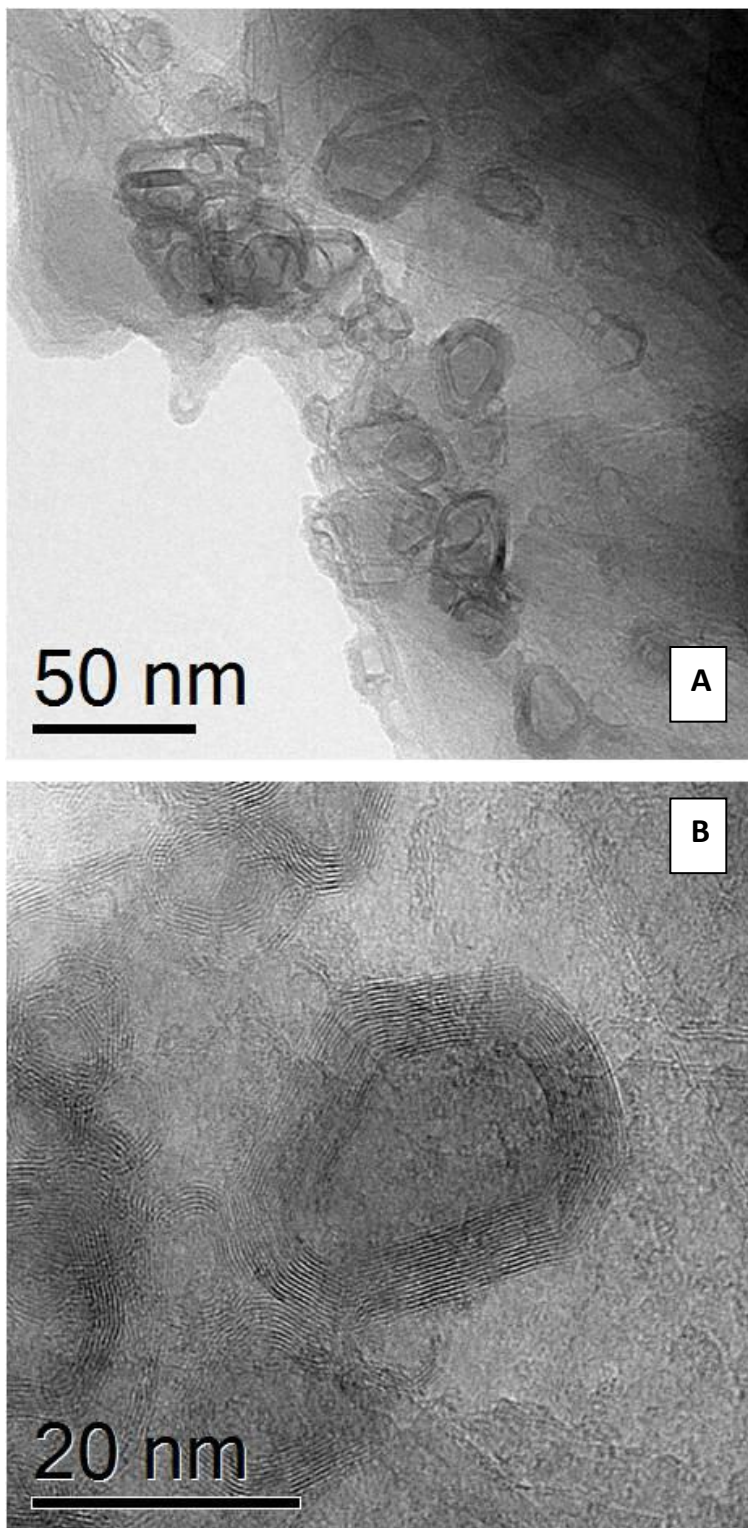


Figure 4.20. TEM images of samples prepared with graphene oxide and a glycerol reflux at (A) 100000X magnification and (B) 400000X magnification.

Overall, graphene oxide did not provide a good support for the methods of catalyst synthesis used in this work. It was shown that GO was modified in the diazonium coupling reaction, however the extent of modification was very low indicating that the coupling reaction needs to be optimized for further studies. Both the conventional iron uptake method and the glycerol reflux indicate that the GO is stacking on itself which could be negatively impacting the materials. In order to utilize GO for active catalyst, the iron uptake procedure will also need to be optimized.

# **Chapter 5 Conclusions and Future Directions**

## 5.1 Optimal Conditions for the Synthesis of NPMCs

Previous work by our group has investigated NPMCs prepared via a benzimidazole or diazonium coupling reaction of 5,6-diamino-1,10-phenanthroline to a carbon support. Optimal conditions were determined for the former reaction and catalyst materials. Part of this work was to optimize the conditions for catalysts prepared using the diazonium coupling reaction by exploring various aspects of the process including the aphen ratio, carbon support, and iron salt. The aim of this work was to synthesize a non-precious metal catalyst with a high density of well-defined active sites with activity comparable to platinum standards.

### 5.1.1 Aphen Ratio

Five different ratios of aphen to carbon BP were synthesized and assessed for overall activity. It was clear that the most active catalyst resulted from a ratio of 1.18 mmol aphen/g carbon, which was the fourth ratio of the series. The amount of aphen loaded onto the carbon support was detected electrochemically prior to introduction of iron or heat treatment, and it was determined that the highest loading was achieved by the third ratio. Upon soaking samples in iron(III) chloride and performing a heat treatment, it was determined that the activity of the catalyst trended with activity for the first four samples rather than three. This indicates that higher loadings of aphen result in the formation of a multilayer which yields electrochemically inactive functionalities that are incorporated into the carbon support as active sites during heat treatment. A decline in activity was still observed for the highest ratio indicating that there is an amount of aphen that is too high and exceeding the optimal loading will negatively impact the catalyst.

### 5.1.2 Carbon Support

Three different carbon supports were explored as a base for the NPMCs; BP, KB, and graphene oxide. The amount of aphen was initially assessed by CV under nitrogen with the peak height being indicative of the amount of aphen coupled to the carbon. Analysis of this data showed that the diazonium coupling reaction was most successful on BP followed by KB and least successful on graphene oxide. It is likely that the conditions for the diazonium coupling reaction were not optimal for the KB or graphene oxide supports.

Comparing the structure of KB to BP shows that KB is more graphitic with fewer oxygen functionalities. This affects the wettability of the material and, since the diazonium coupling

reaction occurs in an aqueous environment, will impact the success of the coupling. This could also be the reasoning behind the lack of effectiveness of the diazonium coupling reaction with graphene oxide. Although a large coverage of oxide groups are expected, the actual structure of graphene oxide is uncertain and the extent of oxidation varies with synthesis methods. It is possible that the amount of oxide coverage was not sufficient to make the graphene oxide wettable enough for the diazonium coupling reaction.

Overall BP had the most successful modification in the diazonium coupling reaction. This appears to be a key factor in the overall catalyst activity. After soaking samples in iron(III) chloride and heat treatment at 700 °C, the most active catalyst was still found to be derived from the BP series.

### 5.1.3 Iron Salt

Two different iron salts were used in the catalyst synthesis; iron(III) chloride and iron(II) acetate. Original BP and KB series were prepared with iron(III) chloride. Two additional series were prepared using iron(II) acetate with BP as the carbon support and either a 50:50 mixture of deionized water and isopropyl alcohol or deionized water alone. Four ratios were used and the overall trend was compared to that of the previous studied BP series. Samples prepared with the mixture of deionized water and isopropyl alcohol were more successful than those prepared with deionized water alone. The isopropyl alcohol helped to increase the wettability of the carbon material making the iron coordination more successful. Overall, the activity of the catalyst prepared with iron(II) acetate followed the trend; increased loading yielded increased activity, however no sample exceeded that of the best material prepared from BP. It was shown that the iron content was too high and two methods were employed to increase the activity; preparing samples with lower iron concentrations and acid leaching the original samples. Neither method proved successful in exceeding the activity of BPS4Fe700.

### 5.1.4 Additional Modifications to procedure

Originally graphene oxide was synthesized for use in a glycerol reflux to eliminate the high temperature heat treatment step. Although the graphene oxide synthesis was successful, the glycerol reflux produced a catalyst with very poor activity. The conditions for this treatment were not optimized and more work is required to produce active catalysts using this method.

A heat treatment in a 50:50 mixture of ammonia and nitrogen gas was also completed in attempts to increase the activity of the catalysts. A small gain was observed in the onset potential coupled with losses for both the limiting current and hydrogen peroxide production. The slight gain in onset potential may also be a result of sample or ink preparation. This indicates that more work is needed with this treatment before it is included in the optimal conditions.

### **5.1.5 Optimal Conditions**

Overall it was determined that the best carbon support, ratio, and iron salt were BP, 1.18 mmol apheh/g carbon, and iron(III) chloride respectively. The optimal heat treatment temperature was also investigated and found to be 700 °C. Although this produced the most active catalyst of the series prepared in this work, it was still outperformed by the tested platinum standard. This leaves much room for improvement as many steps in the reaction can still be optimized. It is predicted that the active sites responsible for the ORR in these materials would be more defined than comparable studies in literature using physisorption methods. This definition will help to further optimize the conditions of the catalyst synthesis to ensure a highly active material with a good coverage of these well-defined active sites.

## **5.2 Future Directions**

Overall successful catalyst materials were synthesized with the largest dependence of activity stemming from the success of the diazonium coupling reaction. Predicted trends were observed with regards to the varying ratios resulting in determination of the optimal ratio of apheh to carbon for preparation of these materials. Heat treatment and ink loadings were also studied and optimal conditions were established. Beyond these factors, much work is needed to optimize the remaining studies to synthesize a material that is comparable to platinum.

### **5.2.1 Verify the Diazonium Coupling Reaction**

While our experiments do confirm covalent attachment of apheh, it is uncertain if this precursor is coupling to the carbon support in the manner proposed in this work. In order to determine if both amines are reacting, the same series can be prepared with a 5 or 6 amino-1,10-phenanthroline and the amount of active precursor post coupling can be compared. This may determine whether or not the two amine functionalities are impacting the coordination.

It is also possible to prepare variations on aphen with the spacing between the amines made further apart. Performing the coupling reaction with a 3, 9-diamino structure would also allow for a study of the effects of the amine groups. The amount of coordination between the 5, 6-diamino and 3, 9-diamino structures can be compared to determine if the spacing between the amine groups will impact the success of the diazonium coupling reaction.

### 5.2.2 Iron Salt

Although it was determined that the iron(III) chloride was the best salt for these series of reactions, the ease at which iron(II) acetate delivers iron to the materials should be explored in more detail. All samples in the iron(II) acetate series were soaked in the same concentration of iron solution which may not be an ideal method. Since the amount of aphen varies so much with each sample, the amount of iron available may also need to change since we see that it is possible to overload the sample. In addition to this, the trend for the four ratios indicated that there wasn't yet a plateau; therefore preparing samples at higher ratios of aphen to carbon may offer an advantage with this iron salt.

In order to determine which aspect of iron(III) chloride (oxidation state or ligand) resulted in a more successful catalyst, further iron salt experiments need to be completed. Performing the metal uptake step with iron(II) chloride would test for the impact of oxidation state while using iron(III)acetate would test for impact of ligand.

It would also be beneficial to pre-coordinate the iron to a nitrogen precursor. This would produce a premade active site that could be coordinated to a carbon support. Synthesizing a catalyst in this way would also reduce the heat treatment step as the active site may already be formed or mostly formed.

### 5.2.3 Ammonia Heat Treatment

Ammonia heat treatments have been shown to improve the overall activity of catalyst materials. Previous work in our lab has shown gains in all materials that were heat treated in a mixture of ammonia and nitrogen.<sup>48</sup> Heat treating an entire series in ammonia would allow for insight into whether or not aphen loading will impact the effects of the ammonia.

### 5.2.4 Glycerol Reflux

Further investigation into the glycerol reflux should be completed. In theory, the graphene oxide sheets should provide sites for the diazonium coupling reaction that can more easily align to form the active site as predicted with the slit pore method. However, it is likely that the conditions for the diazonium coupling reaction were not optimal for this carbon support and work needs to be completed to ensure that this step of the process is successful before moving on to the next portion of the synthesis. Increasing the level of oxidation on the graphene would increase the wettability of the carbon and improve the modification via the diazonium coupling reaction.

Although the glycerol reflux yielded extremely poor results, it was a starting point from which optimization can be studied. It is possible that the reaction time or temperature needs to be adjusted to increase success of the reflux. Once optimal conditions for the diazonium coupling are achieved with graphene oxide, the glycerol reflux may be more effective. Since the reflux seems to cause a stacking of the graphene sheets, an added step or compound to prevent this from occurring may need to be introduced. It is unclear whether or not the stacking occurred as a result of the diazonium coupling or the glycerol reflux. Investigation into each step of the graphene oxide synthesis should be completed to determine the most effective area to begin optimization.

### 5.2.5 Alternate Nitrogen Precursor

Although the coupling of aphen resulted in good activity, other nitrogen precursors may have an advantage over it. Using a smaller nitrogen containing compound, such as adenine (Figure 5.1A) may allow easier access to pores that appear to be an important aspect of the catalyst material. On the other hand, utilizing a larger structure with iron pre-coordinated to it, such as the original porphyrin like structures used in early materials (Figure 5.1B) may be beneficial for use with more graphitic carbons, such as GO, that do not undergo much rearrangement to form active sites. If the active site is already present in the precursor, then the most important aspect of the synthesis would be ensuring that this nitrogen and iron containing compound is successfully attached to the carbon support.

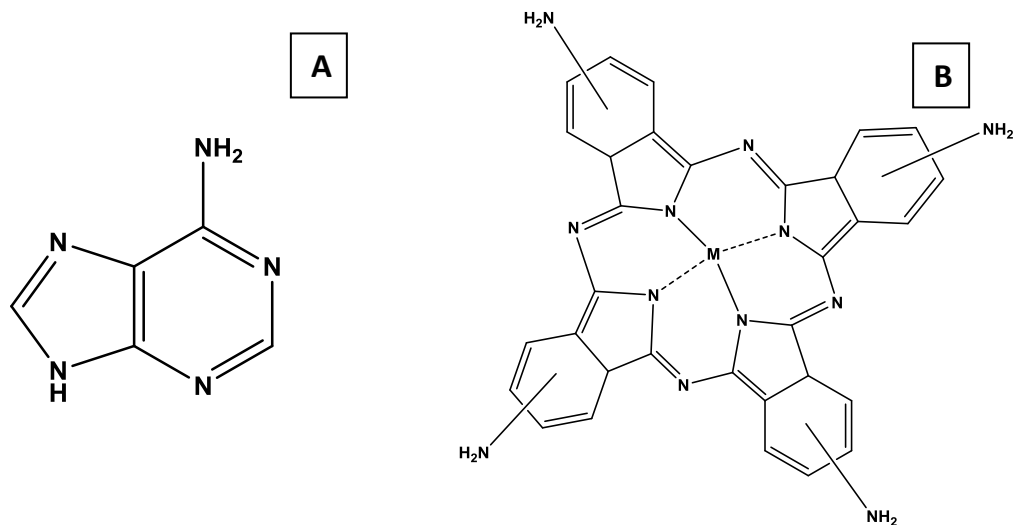


Figure 5.1. Potential nitrogen precursors for synthesis of NPMCs; (A) amine and (B) tetra-amino phthalocyanine<sup>76</sup>

### 5.2.6 Durability and Full Cell Tests

Once successful materials are synthesized, with activity comparable to platinum, further analysis will need to be completed to determine whether or not these materials are viable in a fuel cell. The long term stability will need to be assessed to ensure that degradation of the catalyst will be minimized. In addition to this, the activity in the full cell would need to be tested to fully determine whether or not these materials would offer an advantage to the current catalysts used. It is possible that, due to the large difference in cost, a less active Fe catalyst material may replace their more active counter parts. There is still much work that needs to be completed before these materials can be considered for commercial use; however initial steps were taken to synthesize active NPMC.

## References

1. Sawin, J. L. Renewables 2012: Global Status Report. *REN21* **2012**.
2. Energy Information Administration, U. S. Canada.  
<http://www.eia.gov/countries/cab.cfm?fips=CA> (accessed 01/13, 2014).
3. Golden, D. M. Interaction of Combustion with the Atmosphere. *Proceedings of the Combustion Institute* **2000**, *28*, 2383-2392.
4. Shafiee, S.; Topal, E. When will fossil fuel reserves be diminished? *Energy Policy* **2009**, *37*, 181-189.
5. Winter, M.; Brodd, R. J. What are batteries, fuel cells, and supercapacitors? *Chem. Rev.* **2004**, *104*, 4245-4269.
6. Kang, B.; Ceder, G. Battery materials for ultrafast charging and discharging. *Nature* **2009**, *458*, 190-193.
7. U.S. Department of Energy *Fuel Cell Handbook*, 7<sup>th</sup> Edition; University Press: Hawaii, 2005; .
8. Vishnyakov, V. M. Proton exchange membrane fuel cells. *Vacuum* **2006**, *80*, 1053-1065.
9. Anonymous *PEM fuel cell electrocatalysts and catalyst layers fundamentals and applications*; Springer: London, 2008; .
10. Pilatowsky In *Chapter 2 Thermodynamics of Fuel Cells*; ebrary, I., Ed.; Cogeneration fuel cell-sorption air conditioning systems; Springer: New York, 2011; pp 25-36.
11. Bard, A. J.; Inzelt, G.; Scholz, F. *Electrochemical dictionary*; Springer: Heidelberg, 2012; .
12. Inaba, M. In *In Degradation Mechanism of Polymer Electrolyte Fuel Cells*; 14th International Conference on the Properties of Water and Steam in Kyoto; Kyoto, 2004; , pp 395.
13. Bouwman, P.; Dmowski, W.; Stanley, J.; Cotten, G.; Swider-Lyons, K. Platinum-iron phosphate electrocatalysts for oxygen reduction in PEMFCs. *J. Electrochem. Soc.* **2004**, *151*, A1989-A1998.
14. Srinivasan, S. In *Chapter 4: Fuel Cell Principles*; Fuel Cells: From Fundamentals to Applications; Springer Science and Business Media: United States of America, 2006; Vol. 1, pp 722.
15. Anonymous *PEM fuel cell electrocatalysts and catalyst layers fundamentals and applications*; Springer: London, 2008; .
16. Matthey, J. Price Charts: Platinum. <http://www.platinum.matthey.com/prices/price-charts> (accessed 07/15, 2014).

17. Li, H.; Sun, G.; Li, N.; Sun, S.; Su, D.; Xin, Q. Design and preparation of highly active Pt-Pd/C catalyst for the oxygen reduction reaction. *Journal of Physical Chemistry C* **2007**, *111*, 5605-5617.
18. Toda, T.; Igarashi, H.; Uchida, H.; Watanabe, M. Enhancement of the electroreduction of oxygen on Pt alloys with Fe, Ni, and Co. *J. Electrochem. Soc.* **1999**, *146*, 3750-3756.
19. Easton, E. B.; Bonakdarpour, A.; Dahn, J. R. Fe-C-N oxygen reduction catalysts prepared by combinatorial sputter deposition. *Electrochem. Solid State Lett.* **2006**, *9*, A463-A467.
20. Ammam, M.; Easton, E. B. Oxygen reduction activity of binary PtMn/C, ternary PtMnX/C (X = Fe, Co, Ni, Cu, Mo and, Sn) and quaternary PtMnCuX/C (X = Fe, Co, Ni, and Sn) and PtMnMoX/C (X = Fe, Co, Ni, Cu and Sn) alloy catalysts. *J. Power Sources* **2013**, *236*, 311-320.
21. Bashyam, R.; Zelenay, P. A class of non-precious metal composite catalysts for fuel cells. *Nature* **2006**, *443*, 63-66.
22. Othman, R.; Dicks, A. L.; Zhu, Z. Non precious metal catalysts for the PEM fuel cell cathode. *Int J Hydrogen Energy* **2012**, *37*, 357-372.
23. Bezerra, C. W. B.; Zhang, L.; Lee, K.; Liu, H.; Marques, A. L. B.; Marques, E. P.; Wang, H.; Zhang, J. A review of Fe-N/C and Co-N/C catalysts for the oxygen reduction reaction. *Electrochim. Acta* **2008**, *53*, 4937-4951.
24. Yang, R.; Stevens, K.; Dahn, J. R. Investigation of activity of sputtered transition-metal (TM)-C-N (TM = V, Cr, Mn, Co, Ni) catalysts for oxygen reduction reaction. *J. Electrochem. Soc.* **2008**, *155*, B79-B91.
25. Kramm, U. I.; Herranz, J.; Larouche, N.; Arruda, T. M.; Lefevre, M.; Jaouen, F.; Bogdanoff, P.; Fiechter, S.; Abs-Wurmbach, I.; Mukerjee, S.; Dodelet, J. Structure of the catalytic sites in Fe/N/C-catalysts for O<sub>2</sub>-reduction in PEM fuel cells. *Physical Chemistry Chemical Physics* **2012**, *14*, 11673-11688.
26. Titov, A.; Zapol, P.; Kral, P.; Liu, D.; Iddir, H.; Baishya, K.; Curtiss, L. A. Catalytic Fe-xN Sites in Carbon Nanotubes. *Journal of Physical Chemistry C* **2009**, *113*, 21629-21634.
27. Chen, Z.; Higgins, D.; Yu, A.; Zhang, L.; Zhang, J. A review on non-precious metal electrocatalysts for PEM fuel cells. *Energy & Environmental Science* **2011**, *4*, 3167-3192.
28. Jaouen, F.; Proietti, E.; Lefevre, M.; Chenitz, R.; Dodelet, J.; Wu, G.; Chung, H. T.; Johnston, C. M.; Zelenay, P. Recent advances in non-precious metal catalysis for oxygen-reduction reaction in polymer electrolyte fuel cells. *Energy & Environmental Science* **2011**, *4*, 114-130.
29. Biddinger, E. J.; von Deak, D.; Ozkan, U. S. Nitrogen-Containing Carbon Nanostructures as Oxygen-Reduction Catalysts. *Topics in Catalysis* **2009**, *52*, 1566-1574.

30. Faubert, G.; Cote, R.; Dodelet, J.; Lefevre, M.; Bertrand, P. Oxygen reduction catalysts for polymer electrolyte fuel cells from the pyrolysis of Fe-II acetate adsorbed 3,4,9,10-perylenetetracarboxylic dianhydride. *Electrochim. Acta* **1999**, *44*, 2589-2603.
31. Lefevre, M.; Proietti, E.; Jaouen, F.; Dodelet, J. Iron-Based Catalysts with Improved Oxygen Reduction Activity in Polymer Electrolyte Fuel Cells. *Science* **2009**, *324*, 71-74.
32. JASINSKI, R. New Fuel Cell Cathode Catalyst. *Nature* **1964**, *201*, 1212-&.
33. ALT, H.; BINDER, H.; SANDSTED, G. Mechanism of Electrocatalytic Reduction of Oxygen on Metal-Chelates. *Journal of Catalysis* **1973**, *28*, 8-19.
34. Charreteur, F.; Jaouen, F.; Dodelet, J. Iron porphyrin-based cathode catalysts for PEM fuel cells: Influence of pyrolysis gas on activity and stability. *Electrochim. Acta* **2009**, *54*, 6622-6630.
35. Bezerra, C. W. B.; Zhang, L.; Lee, K.; Liu, H.; Marques, A. L. B.; Marques, E. P.; Wang, H.; Zhang, J. A review of Fe-N/C and Co-N/C catalysts for the oxygen reduction reaction. *Electrochim. Acta* **2008**, *53*, 4937-4951.
36. Bron, M.; Fiechter, S.; Hilgendorff, M.; Bogdanoff, P. Catalysts for oxygen reduction from heat-treated carbon-supported iron phenanthroline complexes. *J. Appl. Electrochem.* **2002**, *32*, 211-216.
37. Wang, H.; Cote, R.; Faubert, G.; Guay, D.; Dodelet, J. Effect of the pre-treatment of carbon black supports on the activity of Fe-based electrocatalysts for the reduction of oxygen. *J Phys Chem B* **1999**, *103*, 2042-2049.
38. Faubert, G.; Cote, R.; Guay, D.; Dodelet, J.; Denes, G.; Poleunis, C.; Bertrand, P. Activation and characterization of Fe-based catalysts for the reduction of oxygen in polymer electrolyte fuel cells. *Electrochim. Acta* **1998**, *43*, 1969-1984.
39. Mo, Z.; Peng, H.; Liang, H.; Liao, S. Vesicular nitrogen doped carbon material derived from Fe<sub>2</sub>O<sub>3</sub> templated polyaniline as improved non-platinum fuel cell cathode catalyst. *Electrochim. Acta* **2013**, *99*, 30-37.
40. Biloul, A.; Gouerec, P.; Savy, M.; Scarbeck, G.; Besse, S.; Riga, J. Oxygen electrocatalysis under fuel cell conditions: Behaviour of cobalt porphyrins and tetraazaannulene analogues. *J. Appl. Electrochem.* **1996**, *26*, 1139-1146.
41. Jaouen, F.; Charreteur, F.; Dodelet, J. Fe-based catalysts for oxygen reduction in PEMFCs - Importance of the disordered phase of the carbon support. *J. Electrochem. Soc.* **2006**, *153*, A689-A698.
42. Yan, X.; Xu, B. Mesoporous carbon material co-doped with nitrogen and iron (Fe-N-C): high-performance cathode catalyst for oxygen reduction reaction in alkaline electrolyte. *J. Mater. Chem. A* **2014**, *2*, 8617-8622.

43. Jaouen, F.; Dodelet, J. Non-noble electrocatalysts for O<sub>2</sub> reduction: How does heat treatment affect their activity and structure? Part I. Model for carbon black gasification by NH<sub>3</sub>: Parametric calibration and electrochemical validation. *J. Phys. Chem. C* **2007**, *111*, 5963-5970.
44. Othman, R.; Dicks, A. L.; Zhu, Z. Non precious metal catalysts for the PEM fuel cell cathode. *Int J Hydrogen Energy* **2012**, *37*, 357-372.
45. Jaouen, F.; Lefevre, M.; Dodelet, J.; Cai, M. Heat-treated Fe/N/C catalysts for O<sub>2</sub> electroreduction: Are active sites hosted in micropores? *J Phys Chem B* **2006**, *110*, 5553-5558.
46. Lefevre, M.; Proietti, E.; Jaouen, F.; Dodelet, J. Iron-Based Catalysts with Improved Oxygen Reduction Activity in Polymer Electrolyte Fuel Cells. *Science* **2009**, *324*, 71-74.
47. Easton, E. B.; Yang, R.; Bonakdarpour, A.; Dahn, J. R. Thermal evolution of the structure and activity of magnetron-sputtered TM-C-N, TM = Fe, Co) oxygen reduction catalysts. *Electrochemical and Solid State Letters* **2007**, *10*, B6-B10.
48. Pauric, A. D.; MacLean, B. J.; Easton, E. B. Fe-N/C Oxygen Reduction Catalysis Prepared by Covalent Attachment of 1,10-Phenanthroline to a Carbon Surface. *J. Electrochem. Soc.* **2011**, *158*, B331-B336.
49. Smith, R. D. L.; Pickup, P. G. Novel electroactive surface functionality from the coupling of an aryl diamine to carbon black. *Electrochemistry Communications* **2009**, *11*, 10-13.
50. Schmidt, G.; Gallon, S.; Esnouf, S.; Bourgoïn, J.; Chenevier, P. Mechanism of the Coupling of Diazonium to Single-Walled Carbon Nanotubes and Its Consequences. *Chemistry-a European Journal* **2009**, *15*, 2101-2110.
51. Rao, C. V.; Cabrera, C. R.; Ishikawa, Y. In Search of the Active Site in Nitrogen-Doped Carbon Nanotube Electrodes for the Oxygen Reduction Reaction. *Journal of Physical Chemistry Letters* **2010**, *1*, 2622-2627.
52. Johnson, W. A. In *Diazotization of Primary Aromatic Amines*; Invitation to Organic Chemistry; Jones and Bartlett Learning: Missassauga, Ontario, Canada, 1999; pp 418 - 420.
53. GALLI, C. Radical Reactions of Arenediazonium Ions - an Easy Entry into the Chemistry of the Aryl Radical. *Chem. Rev.* **1988**, *88*, 765-792.
54. Baranton, S.; Belanger, D. Electrochemical derivatization of carbon surface by reduction of in situ generated diazonium cations. *J Phys Chem B* **2005**, *109*, 24401-24410.
55. Schmidt, G.; Gallon, S.; Esnouf, S.; Bourgoïn, J.; Chenevier, P. Mechanism of the Coupling of Diazonium to Single-Walled Carbon Nanotubes and Its Consequences. *Chem. -Eur. J.* **2009**, *15*, 2101-2110.

56. Kramm, U. I.; Abs-Wurmbach, I.; Herrmann-Geppert, I.; Radnik, J.; Fiechter, S.; Bogdanoff, P. Influence of the Electron-Density of FeN<sub>4</sub>-Centers Towards the Catalytic Activity of Pyrolyzed FeTMPPCl-Based ORR-Electrocatalysts. *J. Electrochem. Soc.* **2011**, *158*, B69-B78.
57. Schulenburg, H.; Stankov, S.; Schunemann, V.; Radnik, J.; Dorbandt, I.; Fiechter, S.; Bogdanoff, P.; Tributsch, H. Catalysts for the oxygen reduction from heat-treated iron(III) tetramethoxyphenylporphyrin chloride: Structure and stability of active sites. *J Phys Chem B* **2003**, *107*, 9034-9041.
58. Jaouen, F.; Marcotte, S.; Dodelet, J.; Lindbergh, G. Oxygen reduction catalysts for polymer electrolyte fuel cells from the pyrolysis of iron acetate adsorbed on various carbon supports. *J Phys Chem B* **2003**, *107*, 1376-1386.
59. Jaouen, F.; Charretier, F.; Dodelet, J. P. Fe-based catalysts for oxygen reduction in PEMFCs - Importance of the disordered phase of the carbon support. *J. Electrochem. Soc.* **2006**, *153*, A689-A698.
60. Dimiev, A.; Kosynkin, D. V.; Alemany, L. B.; Chaguine, P.; Tour, J. M. Pristine Graphite Oxide. *J. Am. Chem. Soc.* **2012**, *134*, 2815-2822.
61. Saleh, F. S.; Easton, E. B. Assessment of the ethanol oxidation activity and durability of Pt catalysts with or without a carbon support using Electrochemical Impedance Spectroscopy. *J. Power Sources* **2014**, *246*, 392-401.
62. Rahman, M. R.; Okajima, T.; Ohsaka, T. Selective Detection of As(III) at the Au(III)-like Polycrystalline Gold Electrode. *Anal. Chem.* **2010**, *82*, 9169-9176.
63. Mavilla, S.; MacLean, B. J.; Easton, E. B. Preparation and Characterization of Non-Precious Metal Fuel Cell Catalysts via Chemical Modification of Carbon Surfaces. *ECS Transactions* **2013**, *53*, 31.
64. Smith, R. D. L.; Pickup, P. G. Voltammetric quantification of the spontaneous chemical modification of carbon black by diazonium coupling. *Electrochim. Acta* **2009**, *54*, 2305-2311.
65. Adenier, A.; Cabet-Deliry, E.; Chausse, A.; Griveau, S.; Mercier, F.; Pinson, J.; Vautrin-UI, C. Grafting of nitrophenyl groups on carbon and metallic surfaces without electrochemical induction. *Chem. Mat.* **2005**, *17*, 491-501.
66. Toupin, M.; Belanger, D. Spontaneous functionalization of carbon black by reaction with 4-nitrophenyldiazonium cations. *Langmuir* **2008**, *24*, 1910-1917.
67. Kariuki, J.; McDermott, M. Formation of multilayers on glassy carbon electrodes via the reduction of diazonium salts. *Langmuir* **2001**, *17*, 5947-5951.
68. Birry, L.; Zagal, J. H.; Dodelet, J. Does CO poison Fe-based catalysts for ORR? *Electrochem. Commun.* **2010**, *12*, 628-631.

69. Bonso, J. S.; Kalaw, G. D.; Ferraris, J. P. High surface area carbon nanofibers derived from electrospun PIM-1 for energy storage applications. *J. Mater. Chem. A* **2014**, *2*, 418-424.
70. Liu, G.; Li, X.; Ganesan, P.; Popov, B. N. Studies of oxygen reduction reaction active sites and stability of nitrogen-modified carbon composite catalysts for PEM fuel cells. *Electrochim. Acta* **2010**, *55*, 2853-2858.
71. Pauric, A. D.; Pedersen, A. W.; Andrusiak, T.; Easton, E. B. A Surface Modification Route to Nonprecious Metal Fuel Cell Catalysts. *J. Electrochem. Soc.* **2010**, *157*, B370-B375.
72. PELS, J.; KAPTEIJN, F.; MOULIJN, J.; ZHU, Q.; THOMAS, K. Evolution of Nitrogen Functionalities in Carbonaceous Materials during Pyrolysis. *Carbon* **1995**, *33*, 1641-1653.
73. Wang, H.; Cote, R.; Faubert, G.; Guay, D.; Dodelet, J. Effect of the pre-treatment of carbon black supports on the activity of Fe-based electrocatalysts for the reduction of oxygen. *J Phys Chem B* **1999**, *103*, 2042-2049.
74. ANSON, F.; BLAUCH, D.; SAVEANT, J.; SHU, C. Ion Association and Electric-Field Effects on Electron Hopping in Redox Polymers - Application to the Os(bpy)<sub>3</sub>(3+)/<sub>2</sub><sup>+</sup> Couple in Nafion. *J. Am. Chem. Soc.* **1991**, *113*, 1922-1932.
75. Anonymous In *Infrared and Raman Spectroscopy: Forensic Applications in Mineralogy*; Chalmers, J. M., Edwards, H. G. and Hargreaves, M., D., Eds.; Infrared and Raman Spectroscopy in Forensic Science; John Wiley and Sons: United Kingdom, 2012; pp 424.
76. Isaacs, M.; Armijo, F.; Ramirez, G.; Trollund, E.; Biaggio, S.; Costamagna, J.; Aguirre, M. Electrochemical reduction of CO<sub>2</sub> mediated by poly-M-aminophthalocyanines (M = Co, Ni, Fe): poly-Co-tetraaminophthalocyanine, a selective catalyst. *J. Mol. Catal. A-Chem.* **2005**, *229*, 249-257.
77. Grondein, A.; Belanger, D. Covalent grafting of aminated compounds on Vulcan XC72R by melamine in situ diazotization. *Carbon*. **2012**, *50(12)*, 4335-4342.

## Appendices

### THE AMERICAN ASSOCIATION FOR THE ADVANCEMENT OF SCIENCE LICENSE TERMS AND CONDITIONS

Aug 05, 2014

---

This is a License Agreement between Stephanie G Mavilla ("You") and The American Association for the Advancement of Science ("The American Association for the Advancement of Science") provided by Copyright Clearance Center ("CCC"). The license consists of your order details, the terms and conditions provided by The American Association for the Advancement of Science, and the payment terms and conditions.

**All payments must be made in full to CCC. For payment instructions, please see information listed at the bottom of this form.**

License Number	3442800189601
License date	Aug 05, 2014
Licensed content publisher	The American Association for the Advancement of Science
Licensed content publication	Science
Licensed content title	Iron-Based Catalysts with Improved Oxygen Reduction Activity in Polymer Electrolyte Fuel Cells
Licensed content author	Michel Lefèvre, Eric Proietti, Frédéric Jaouen, Jean-Pol Dodelet
Licensed content date	Apr 3, 2009
Volume number	324
Issue number	5923
Type of Use	Thesis / Dissertation
Requestor type	Scientist/individual at a research institution
Format	Print and electronic
Portion	Figure
Number of figures/tables	1
Order reference number	None
Title of your thesis / dissertation	Non-precious Metal Catalysts Prepared by Chemical Functionalization of Carbon Surfaces
Expected completion date	Aug 2014
Estimated size(pages)	122
Total	0.00 USD
Terms and Conditions	